2015

Economical production of high performance MgB2 superconductor with improved grain connectivity

Shaon Barua
University of Wollongong

Institute for Superconducting and Electronic Materials

Economical Production of High Performance MgB_2 Superconductor with Improved Grain Connectivity

Shaon Barua

This thesis is presented as part of the requirement for the award of the Degree of Master of Philosophy of the University of Wollongong

June 2015

DECLARATION

I, Shaon Barua, declare that this thesis, submitted in partial fulfillment of the requirements for the award of Master of Philosophy, in the Institute for Superconducting & Electronic Materials (ISEM), Faculty of Engineering, University of Wollongong, Australia, is wholly my own work unless otherwise referenced or acknowledged. This document has not been submitted for a qualification at any other academic institution.

Shaon Barua

June, 2015

ACKNOWLEDGEMENTS

First of all, I would like to express my heartfelt gratitude to my supervisors, Dr. Md. Shahriar Al Hossain, Prof. Jung Ho Kim, Dr. Zongqing Ma, for their continuous academic guidance, encouragement, and advice throughout my studies in the Institute for Superconducting and Electronic Materials (ISEM) at the University of Wollongong.

I would like to extend my gratitude to the directors of ISEM Prof. Shi Xue Dou and Prof. Xiaolin Wang for their support and advice.

I would like to express my gratitude to Dr. Germanas Peleckis and Dr. Xun Xu for the training you gave to me on PPMS and XRD, and solving any problems related to equipment.

I am grateful to Dr. Andrzej Morawski, Dr. Daniel Gajda, Mr. Tomek Cetner, Mr. Pawel Galat, for their support during my research visit to Institute of High Pressure Physics, Poland. I would also like to acknowledge all of them for their great collaboration and for generous opportunity they gave me to use their facilities.

My special thanks are to Dr. Tania Silver for her kind help in proofreading and correcting the English in the manuscripts of my journal articles and this thesis.

I would like to extend my special thanks to Dr. David Wexler, Dr. Gilberto Casillas Garcia, Dr. Mitchell Nancarrow, and Mr. Tony Romeo for their crucial contributions to measurements and fruitful discussions.

I would also like to thank the technical team at ISEM, especially, Mr. R. Morgan and Mr. Paul for their enthusiastic support.

This work would have not been completed without continuous encouragement from all my colleagues, including, Ashkan Motaman, Dipak Patel, Rejaul Kaiser and my friends in

Wollongong, Parvez Mannan, Majharul Khan helped me to keep mentally strong all the times. Last but not least, I thank my loving family, including my parents and sisters for being supportive and caring siblings.

Finally, I would like to thank everybody who was important to the successful realization of this thesis, as well as expressing my apologies that I could not mention them all personally, one by one.

TABLE OF CONTENTS

LIST OF FIGURES

LIST OF TABLES

ABSTRACT

The discovery of superconductivity in MgB_2, a binary intermetallic, by Jun Akimitsu in Japan created huge among the scientific community in applied superconductivity research. Extensive researches have been carried out throughout the last decade to make it viable for practical application. It is considered as the potential candidate for replacing conventional low temperature superconductors (LTS) and high temperature superconductors (HTS) due its remarkable properties, such as comparatively high critical temperature of 39 K, simple crystalline structure, weak link free grain boundaries, low materials cost. Soaring helium price is a serious threat to LTS. On the other hand, more than 20 years of efforts did not reduce the production cost of HTS. In addition, larger coherence length and lower anisotropy make MgB_2 competitive with HTS. Therefore, MgB_2 is technologically and economically viable conductor than LTS and HTS.

One of the possible applications of MgB_2 conductor is in superconducting magnets. Where, both high field and low field performance is very crucial factor from the application point of view. Previously, many researches have been successfully done to improve high field properties by carbon doping but low field performance is still poor. The best performance MgB_2 wire fabrication technique to date relies on the use of high purity amorphous boron powder, which is almost unavailable and very expensive. All commercial wires are produced using only amorphous boron powder. The high-field J_c of wire made from crystalline boron is significantly lower than that using amorphous boron when these are treated in identical conditions. Amorphous boron powder is made using radio frequency (RF), plus unavailability of high quality precursor boron powder has become a blocking factor for further progress in development of MgB_2 wire. Crystalline boron is a cheaper and readily available precursor powder. However, when it reacts with Mg to form MgB_2, a relatively high sintering

temperature or long sintering times are required, which incubates grain growth and hence will reduce the pinning force as the grains become larger, and thereby, the J_c is decreased.

In this thesis, an economic solution has been proposed to fabricate high performance *in-situ* powder in tube (PIT) MgB_2 wire. A systematic approach has been followed to address the existing problems associated with the commercially feasible conductor.

Firstly, chemical doping method has been used to enhance the superconducting performance. From the previous knowledge, it is well established that chemical doping is the simplest and cheapest way to improvise the electronic structures of superconductors and their superconducting performance. To date, much attention has been paid to the enhancement of the high-field J_c properties of MgB_2 wires and carbon substitution on boron sites by chemical doping with nano-SiC, carbon nanotubes, nano-carbon, carbohydrate, etc. Carbon dopant has proved its potential to enhance the high-field properties, although researchers are still struggling to improve the low-field *J*c for practical applications. Among the aforementioned dopants, in this work, nano-size SiC was considered, and which is one of the most effective dopants for MgB_2. It was found that alumina (Al_2O_3) is more stable in terms of reaction with MgB_2 and as a dopant, results in low field J_c enhancement due to improved grain connectivity. To investigate the effect of simultaneous doping with nano-Al_2O_3 and SiC on the formation and superconductivity properties of the MgB_2 bulk and wires were fabricated. In this work, to improve the in-field J_c performance, the effects of co-doping with nano-Al_2O_3 and SiC into MgB_2 bulks and wires on the microstructure, as well as the superconducting and electronic properties were studied. It was found that the *a*-axis lattice parameter decreases faster than the *c*-axis one with the increasing addition of SiC. This clearly indicates the substitution of carbon on boron sites in the *ab*-plane. However, the *c*-axis only slightly modulated with the addition of Al_2O_3. It was found that co-doping with SiC and Al_2O_3 also reduces the transition

temperature (T_c) more than in the undoped and alumina only doped MgB_2 sample. The co-doped sample with the composition of 2 wt% Al_2O_3 + 1 wt% SiC showed the best in-field J_c performance at both 10 and 25 K. The value of $B(10^4)$ [the field at which $J_c = 10^4$ Acm^{-2}] was enhanced from 7.6 T to 9.8 T in the co-doped wire compared to the pure wire due to improved grain connectivity, smaller grain size, and C-substitution, as evidenced by the ρ, full width half maximum (FWHM), T_c, and *a*-axis lattice parameter, respectively.

After successful application of co-doping, another chemical doping method has been studied using carbon low cost carbon encapsulated boron. Previously, many research groups introduced carbon (C) into the MgB_2 lattice structure in various methods, and among those methods, the most popular techniques are solid state mixing and the chemical solution route. In the case of solid state mixing, nano-size precursors, such as SiC and C, are used, but usually, nano-size precursor powders tend to become agglomerated during the mixing process. In addition, inhomogeneous mixing between precursors makes the MgB_2 undergo complicated reactions or leads to unexpected impurity phases. Alternatively, the chemical solution route has been suggested, and the effects of carbohydrate, i.e., malic acid, introduced in this way on the MgB_2 superconducting material have been evaluated, demonstrating that this is one of the most successful techniques reported so far. In this case, homogeneity of the carbon cannot be achieved up to the desired level. This is because there is no definitive control during this process due to the high volatility of the liquid hydrocarbon. Lately, a more efficient carbon-doping method was introduced, with the product called pre-carbon-doped boron, resulting in enhancement of the irreversibility field (B_{irr}) and the upper critical field (B_{c2}) when it was used in MgB_2 superconductor. In that method, boron was amorphous, but with some monocrystalline nature, synthesized by the radio frequency (RF) plasma method. In this process, however, residual BCl_3 adsorbed on the powder particles can react with the humidity in air, which is detrimental to the performance of the superconductor. In order to overcome

these problems, a new *in-house* carbon-encapsulated boron powder was fabricated and studied in collaboration with Pavezyum Kimya, Turkey. These MgB_2 bulks prepared with this boron show enhanced magnetic J_c, with the highest value of 10^4 Acm^{-2} at 9.47 T, 5 K. The reason behind the improved high field J_c and pinning force is that the enhanced grain boundary pinning, and homogeneous carbon distribution in the carbon-doped samples increase the Mg and B reactivity, and at the same time, restrict the grain growth of the reacted MgB_2. These results indicate that carbon-encapsulated amorphous boron could be a promising alternative for industrial production of practical MgB_2 bulks or wires with excellent J_c, as large-scale production can be commercially viable in terms of cost-effectiveness.

Cost of conductor is a determining factor in terms of potential application. To decrease the conductor cost significantly starting materials cost should be minimized. To investigate the performance of low cost starting materials in combination with cold high pressure densification an innovative approach has been applied. The reason behind this investigation is that high quality precursors cost is significantly high, which increases the conductor cost enormously. The price of high purity (99%) amorphous B powder is about ten times more expensive than low purity (96%) crystalline B powders. In this study, wires were fabricated by using low cost carbon encapsulated crystalline boron and different sizes of Mg powder. A significant enhancement of transport J_c was observed in the wires made with big size Mg and low cost crystalline boron powders after CHPD. It was found from this investigation that large size size Mg is an alternate solution to the internal Mg diffusion (IMD) method for the development of high performance, cost-effective MgB_2 wires for industrial application. In these wires, localized diffusion of Mg occurs and the process acts like localized IMD (LIMD). The J_c of CHPD treated wires made from crystalline boron and large-size Mg shows the best performance among the other wires in this study. The possible reason for increased J_c may be the flat, directional, and elongated voids that arise after heat treatment from large size ductile

Mg during the cold working process. The performance of the densified wire made from cheap crystalline boron and large-size Mg showed similar J_c-B properties to wires using expensive nanosize materials. The critical current density of the wire in this work reached > 10^5 at 4.2 K and 4 T, which is within the feasible range for application in low-field magnetic resonance imaging (MRI) machines.

After finding an innovative solution for enhancement of in-field J_c by carbon doping and applying pressure, further investigation was carried out to achieve next stage enhancement. From the previous study it was proved that low cost wire can be produce by using large size Mg and carbon encapsulated crystalline powder with CHPD. In this method high core density was obtained in the final wire by apply CHPD before the heat treatment process. To get next stage improvement of J_c, another high pressure process was applied. In this new investigation, *in-situ* PIT wires were fabricated with *in-house* carbon encapsulated B powder and large size Mg. After fabrication of wires, pressure was applied in two steps, before the reaction by CHPD and during the reaction by HIP. The J_c was significantly increased in this process. At 4.2 K, the J_c value was 10,000 Acm^{-2} at close to 14 T which is comparable to 2G IMD wire. The advantages of this CHPD and HIP treated LIMD wire over IMD wire is that there is no hollow structure inside the wire. A highly dense wire with enhanced mechanical durability can be fabricated by this method, which is desirable for large scale application.

CHAPTER 1: INTRODUCTION

1.1 Historical development of superconductor

Superconductivity is defined as the appearance of fascinating electromagnetic property, due to which, certain materials lose their electrical resistance at extremely low temperature. Vanishing of resistance is entranced by certain critical temperature (T_c) below which resistance to electrical current disappear, associated with critical current density (J_c) and critical field (H_c). Critical temperature act as a boundary between superconducting state and normal state, here normal state indicates the returning of resistivity (see **Figure1.1**).

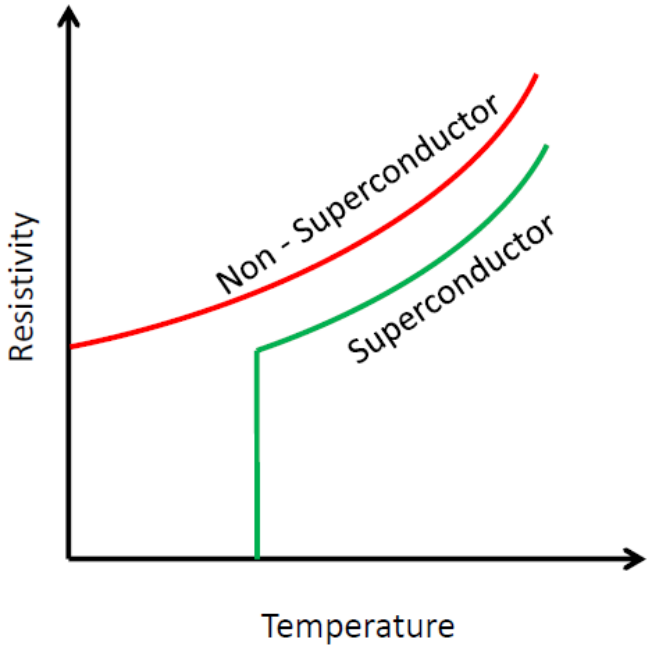

Figure 1.1 Temperature dependency in superconductor and non- superconductor[1]

In 1911, Heike Kamerlingh Onnes of Leiden University, a Dutch physicist, first observed superconductivity in mercury. When he cooled the mercury at liquid Helium temperature, the electrical resistivity of mercury was suddenly dropped to lower than measurable value (close to zero)[2]. In 1913, for discovering this incredible phenomenon, he was awarded Nobel Prize in Physics.

After the discovery of superconductivity, the next great milestone in understanding the behaviour of matter at extremely low temperatures was occurred in 1933. When two German researchers, Walther Meissner and Robert Ochsenfeld discovered that a superconducting material not only possesses zero resistance, but also repels a magnetic field in the superconducting state. This phenomenon is popularly known as the Meissner effect[3]. In the superconducting state, the Meissner effect is so strong that it can create enough force to levitate magnet over a superconducting material.

The single most important experiment which was reported by two different laboratories simultaneously in 1950, Reynolds *et al.*[4] at Rutgers University, and Maxwell working at the National Bureau of Standards[5] was the experiment on the "isotope effect". This experiment played a significant role in guiding the way to an explanation of superconductivity. They found that the critical temperature for the superconducting transition was lower in the sample which had the higher isotopic mass. In fact the critical temperature was inversely proportional to the square root of the average isotopic mass of the materials.

In 1957, the first widely-accepted theoretical model of superconductivity was proposed by American physicists John Bardeen, Leon Cooper, and John Schrieffer. Their Theories of Superconductivity became known as the BCS theory, which was derived from the first letter of each man's last name and won them a Nobel Prize in 1972. According to the theory, the electrical transport in superconductors is due to the pairing of electrons (Cooper pairs) with opposite moment and spins instead of single electrons. The coherent travelling of electron pairs leads to resistance-less current flow through a superconducting material[2]. The mathematically-complex BCS theory explained superconductivity at temperatures close to absolute zero for elements and simple alloys. However, the BCS theory becomes inadequate to fully explain superconducting phenomena at higher temperature and different superconducting systems.

Another significant theoretical advancement came in 1962 when a graduate student at Cambridge University, Brian D. Josephson, predicted that electrical current would flow between two superconducting materials - even when they are separated by a non-superconductor or insulator[2]. His prediction was later confirmed and won him a share of the 1973 Nobel Prize in Physics. This tunnelling phenomenon is widely known as the "Josephson effect" and has been used to electronic devices such as the SQUID, an instrument capable of detecting even the weakest magnetic fields.

Then, in 1986, a revolutionary discovery was made in the field of superconductivity. Alex Müller and Georg Bednorz, two researchers at the IBM Research Laboratory in Rüschlikon, Switzerland, synthesized a brittle ceramic compound that showed superconductivity at the highest temperature then known, 30 K. This discovery was so remarkable, because ceramics are normally insulators and don't carry current at all. So, researchers had not considered them as probable high-temperature superconductor candidates. The Lanthanum (La), Barium (Ba), Copper (Cu) and Oxygen (O) compound that Bednorz and Müller synthesized, behaved in a not-as-yet-understood way[6]. For discovery of superconducting copper-oxides (cuprates), both of them own Nobel Prize in 1987. In January of 1987, a research team at the University of Alabama-Huntsville first substituted Yttrium (Y) for Lanthanum (La) in the Müller and Bednorz molecule and achieved an incredible 92 K T_c in YBCO. Later, much higher T_c was observed in ceramic superconductors in the mercuric-cuprates, with a transition temperature of 134 K, discovered by the team of Schilling *et al.*[7] of Zurich, Switzerland.

In 2001, Nagamatsu *et al.* found a simple binary compound of magnesium (Mg) and boron (B), magnesium diboride (MgB_2), to be an astonishing new superconductor which shows T_c of 39 K. The critical temperature of MgB_2 is the highest among the elemental or binary alloy superconductors[8]. After the discovery of superconductivity in MgB_2, many research groups are

working for making it industrially feasible conductor, especially to replace NbTi and Nb_3Sn conductors in high magnetic field applications such as high field magnets[9].

In 2008, oxypnictide or iron-based superconducting material ($LaO_{1-x}F_xFeAs$) was discovered, with T_c of 26 K. After that discovery, extensive research was carried out to enhance T_c, and 52 K was found by replacing lanthanum (La) with other elements, such as, samarium (Sm) and neodymium (Nd)[10, 11]. Later, Ishikawa *et al.* reported high pressure technique to synthesize BaFe2As2, which resulted in higher T_c around 35 K[12]. In 2014, Mankowsky *et al.* reported room temperature superconductivity in YBCO for picoseconds by using mid-infrared laser pulses through deformation of material's crystal structure[13]. **Figure 1.2** shows the history of superconductor development with time.

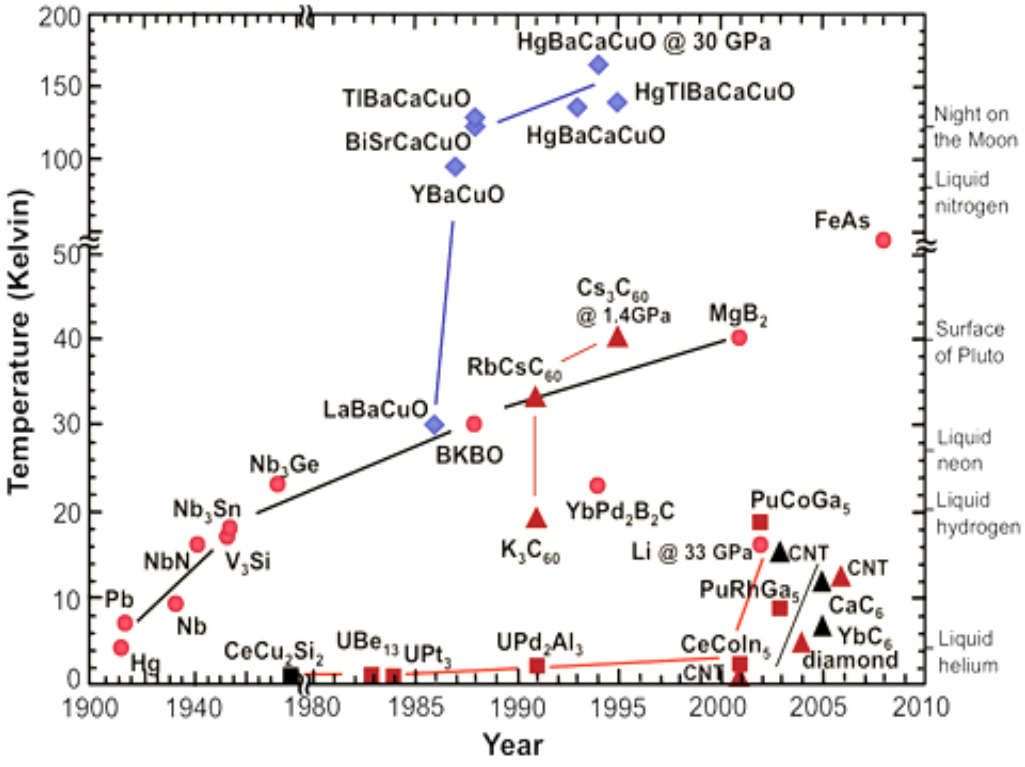

Figure 1.2 The history of superconductor development with time

1.2 Fundamentals of superconductivity

Superconducting state is determined by the three important parameters: (i) critical temperature (T_c), (ii) Critical current density (J_c) and (iii) critical field (H_c). The interrelations among these parameters are shown in **Figure 1.3**.

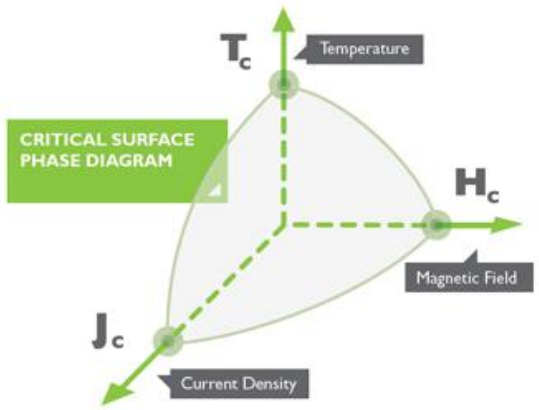

Figure 1.3 Critical phase diagram[1]

According to Meissner effect, if a superconductor is placed in a magnetic field, it will not allow existence of magnetic flus density in interior of superconducting materials. Furthermore, a shielding current will be created to repeal the applied magnetic field[1-3]. As a consequence of the behaviour against the magnetic field, a superconductor can be distinguished from a conductor as it expels all magnetic fields when subjected to superconducting transition. In 1958, based on the responses of the superconductor to the applied magnetic field, Abrikosov divided superconductor materials into two types, type-I and type-II. Generally, type-I superconductivity is well known in pure element superconductors and type-II superconductivity is found in the alloys[1, 2].

When a type-I superconductors is subjected to higher magnetic field than the critical value, superconducting properties is abruptly destroyed (see **Figure 1.4(a)**). On the contrary, in type-II superconductor, raising the applied magnetic field above the critical value leads to a mixed

state, yet it remains superconductor at that state also as long as the current is low(see **Figure 1.4(b)**). Further increase in the applied filed till the second critical field (H_{c2}) it shows superconductivity[1, 2].

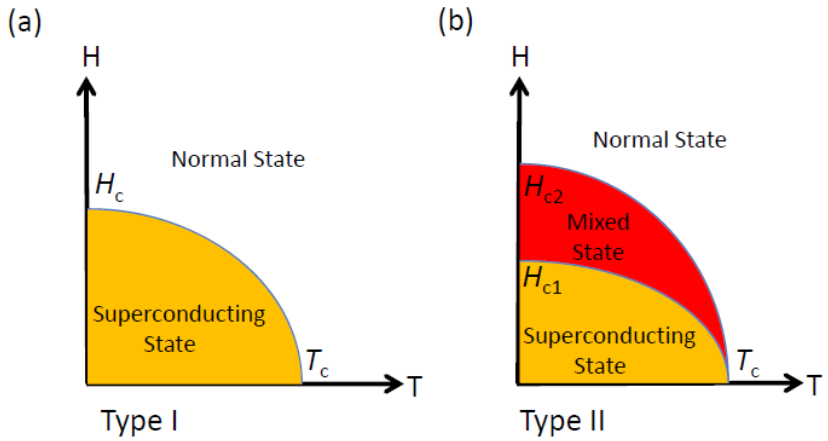

Figure 1.4 Schematic representation of (a) type-I and (b) type-II superconductors

If a type-I superconductor is placed in a weak external magnet field, the field penetrates into the material for only a short distance, which is termed as the London penetration depth (λ_L). It decays to zero, according to following rule (see Equation 1.1)[1, 2].

$$B(x) = B(0)e^{\left(\frac{-x}{\lambda_L}\right)} \quad \text{..... (1.1)}$$

Where, x is the distance from the surface and $B(0)$ is representing the flux density of the applied fields at the surface. Due to difference between the experimentally determined penetration depth (λ), and the London penetration depth, (λ_L), Equation (1.2) was applied to correct by introducing the coherence length (ξ) and mean free path (l)[14]. The coherence length (ξ) is defined as the distance between the surface and where the sample reaches the density of superconducting electrons which is of the order of 10^{-4}cm for a pure superconductor[2]. Here, ξ is dependent on the purity of the material and treated as analogous to mean free path.

$$\frac{1}{\xi} = \frac{1}{\xi_0} + \frac{1}{l} \quad \ldots\ldots\ldots\ldots\ldots\ldots \quad (1.2)$$

Where, ξ_0 is the coherence length stands for a perfectly pure superconductor.

Coherence length is reduced when the impurity content is increased[2, 15]. Thus the coherence length of an impure material is given by $\kappa = \lambda / \xi$, where κ is the Ginzburg-Laudau (GL) parameter. Presence of impurities in superconductors results in higher normal state resistivity, because to electron scattering, which leads to shortening of coherence length and higher κ value[16].

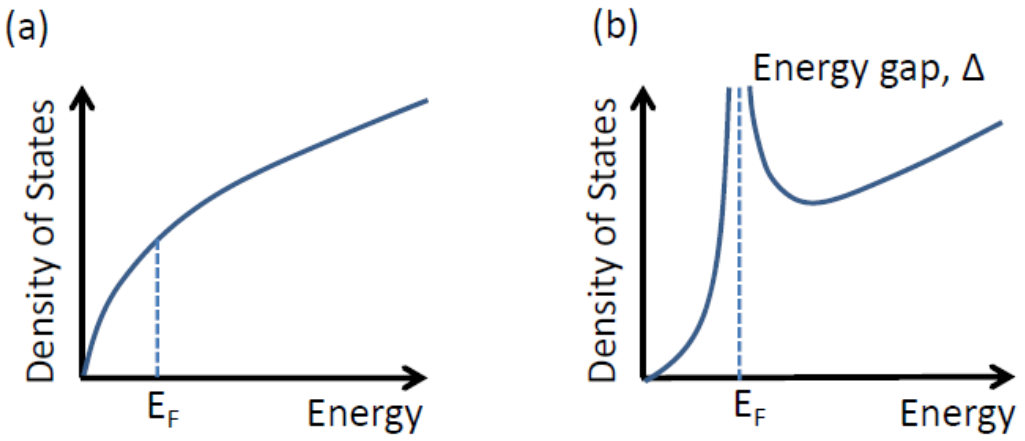

Figure 1.5 Density of states versus energy for metal in (a) normal state and in (b) superconducting state.[15]

The BSC theory states that, there is an energy gap in superconducting materials between the ground state and the quasi-particle state, along with the width equal to 1.76 $K_b T_c$, where K_b denotes Boltzmann's constant (see **Figure 1.5**). Conversely, at absolute zero temperature, for normal materials, energy states are covered up to the Fermi energy level E_F. The success of the BSC theory is due to introduction of the cooper pairs[2], which are the charge carriers in superconducting state, poses lowest energy level as a result of electrons interaction near the Fermi energy level. When temperature is raised above the absolute zero temperature, cooper

pairs split up into two quasi particles due to thermal agitation, which causes decrement in the energy gap, furthermore it will be zero at T_c[2, 15].

Abrikosov's investigation suggested the exact value of the GL parameter (κ), based on which superconductors can be categorized. When $\kappa < 1/\sqrt{2}$, the superconductor falls into type I, and if $\kappa > 1/\sqrt{2}$, the superconductor falls into type II[15].

In type-II superconductors, the magnetic field penetration is same as the type-I superconductor up to first critical field (H_{c1}); beyond this critical field, type-II superconductors goes to a new mixed state (or Shubnikov state), where penetration of the magnetic field into the superconductor occurs in the form of the thin filament, which is called the magnetic vortices and these magnetic vortices carries one magnetic flux quantum ($\Phi_0 = 2.067 \times 10^{-15}$ Tm^2)[1].

Further increment of field above H_{c1} introduces more vortices. As long as those magnetic vortices remain fixed and not influenced by the current, do not hamper the current flow. The flux lines are formed by normal core and which is enclosed by supper current vortex. This super-current vortex decays over a distance of λ(T) for bulk samples. The diameter of the vortices is of the order of the superconductor coherence length, ξ, i.e. typically nanometres (coherence length of $MgB_2 \approx \xi_{ab}(0) = 3.7–12.8$ nm, $\xi_c(0) = 1.6–5.0$ nm)[17].

Increasing current perpendicular to the applied field leads to vortex movement as a result of strong Lorentz force (F_L) acting on the vortices. As the vortex movement leads to resistive nature of the materials, it is very important to keep this force low for making sure that the material is in superconducting state. Different atomic defects can effectively pin the magnetic vortices, such as: impurities, grain boundaries, staking fault, dislocations and inclusions. If the size of the vortices matches with the defects, it acts very effectively. Therefore, the performance of the superconductor largely depends on the type, extent and the density of the defects as those are precondition for effective pinning centres[2].

The upper limit of the applied field for practical application is largely depends on another important parameter, the de-pinning field, H_{irr} ,where the vortex pinning is very weak due to enhanced Lorentz force and which results very low current density. Goodness of pinning properties can be predicted from the difference between the H_{c2} and H_{irr}, as the lower difference attributed to spinning properties of that material[2, 18].

1.3 Applications of superconductors

Superconducting materials are used in a wide range of commercial and industrial applications, such as, in energy production, in sensor materials, storage, and distribution, and in high field magnets. Nowadays, the low-temperature superconductors (LTS) materials, particularly Nb_3Sn (T_c of 18 K) and NbTi (T_c of 9 K) are used in nuclear magnetic resonance (NMR), magnetic resonance imaging (MRI), and magnets for plasma fusion devices[9]. Due to the superior properties of Nb-47wt.% Ti alloy, such as, economical fabrication process in a ductile form and nano-structure have made it compatible for high critical current applications. Ease of manufacturing in kilometres lengths of Nb_3Sn based strands and high critical current densities, made it as a prominent superconductor for commercial applications[9].

Contrarily, the high-temperature superconductors (HTS), mainly bismuth strontium calcium copper oxide (BSCCO) (Bi-2223, T_c of 110 K, and Bi-2212, T_c of 85 K) and $YBa_2Cu_3O_7$-x (YBCO, T_c of 92 K) are being used in electric power applications[9, 19]. Another promising invention was electric generator using the superconducting conductor. The size of those generators was reduced to the half of the conventional generators and efficiency also improved significantly.

Significant advancement of superconductor made it possible to produce superconductor based transformers and fault current limiters (FCL) with enormously improved performance. The Swiss-Swedish company ABB was the pioneer in introducing superconducting transformer to

a utility power network, in March 1997. Recently, ABB announced the development of a 6.4 MVA fault current limiter, which is the most powerful in the world[20]. In the electronics industry, superconductors are used in ultra-high-performance filters, in which zero resistance of the superconducting conductor plays primary role. There are disparate uses of superconductors in the military. The U.S. Navy uses HTSC superconducting quantum interference devices (SQUIDS) to detect mines and submarines. Using the magnetic levitation (MAGLEV) of superconductors, transport vehicles such as trains can be made to "float" on strong superconducting magnets[20]. This eliminates friction between the train and the track. The first commercial use of MAGLEV technology was introduced in Japan, 1990. Recently, in April 2015, the MLX01 test vehicle reached an incredible speed of 374 mph[20].

1.3.1 Potential of MgB_2 for superconducting applications

One of the major commercial markets for superconducting wires is magnetic resonance imaging (MRI) magnets. In MRI magnets, higher image quality and very strong, homogeneous, and stable field strength are crucial factors[21]. MgB_2 superconductor has vast potential in this industry[22]. The impact of MgB_2 in this industry largely depends on competitiveness of conductor price at a certain temperature and magnetic field. At 20 K, MgB_2 conductor is very promising superconductor due to low fabrication cost, larger coherence length, relatively high critical temperature, rich multiple-band structure etc. Development of cryocooler is another important prerequisite for application of MgB_2. But, the cryogenic refrigeration system required for operating at temperatures near 20 K is comparatively less complex and more energy saving than those operate at liquid helium temperature. Solid nitrogen is being considered as a cryogen due to its high heat capacity for MgB_2 based MRI magnets[23-25]. Soaring helium price is a serious threat to the LTS (i.e. NbTi and Nb_3Ti). Hence, MgB_2 conductor is a potential candidate for future MRI system. Disparate efforts are being carried out by different companies, such as Columbus Superconductors in Italy, Hyper Tech Research (HTR) in the

US, and Hitachi Ltd in Japan. Columbus Superconductors and ASG Superconductors, first demonstrated the "Open-Sky" MRI system. The central magnetic field reached 1.0 T at an operating temperature of 16 K in this MRI system. Along with other interesting properties, the sharp superconducting transition makes MgB_2 conductor ideal for resistive-type fault current limiters (FCL). The FCL device are generally used in electrical power transmission and distribution systems, which provides an important advantage by coping with the persistent increase in fault current levels during the upgradation of existing power systems. Recently, Hascicek *et al.* designed and tested a 12.5 kVA MgB_2-based superconducting transformer[26]. In 2013, Kajikawa *et al.* reported a fully superconducting motor using MgB_2 conductor[27]. HTR developed a racetrack coils for the cryogenic rotor in a liquid hydrogen-cooled superconducting generator using MgB_2 conductor for NASA[28]. Tajima et al. reported thin film MgB_2 for application in RF structures for particle accelerators[29]. Different theoretical studies were reported on practical application using MgB_2 conductor[30-33].

Along with high T_c, MgB_2 superconductor poses the simple crystal structure, transparency of grain boundaries to supercurrent, large coherence length, low product cost, and high critical field. All these important features make it suitable for both large-scale applications and electronic devices. In addition, the costs of the precursor materials for both Mg and B are comparatively less than Nb-based superconductors' precursors, make it attractive for industrial use.

But the major limitation for MgB_2 is the fast drop of its critical current density (J_c) in high magnetic field due to weak pinning. During the last decade, extensive research have been done to confront this problem. From the state of art research on different processing techniques such as chemical doping, thermo-mechanical processing, and irradiation, it is now established that chemical doping is the easiest and quickest way of improving superconducting properties[16, 34-

[38]. Among the different dopant, carbon is the best dopant so far reported, particularly in improving the high field J_c and upper critical field (H_{c2})[16, 18, 34-36, 39, 40]. The development of MgB_2 superconductor in the form of single crystals, bulks, wires, tapes and thin films, is so rapid that commercialization is possible in near future.

1.4 Aim and outline of the thesis

The main goal of this thesis is to improve the MgB_2 performance intrinsically by homogeneous doping to improve B_{c2} and extrinsically by reducing porosity along with increasing connectivity between the grains.

In Chapter 1, a brief reviews on the history of superconductors, fundamentals characteristics of superconductivity, applications of different superconductors, and the prospects of MgB_2 for superconducting applications are discussed. Chapter 2 reports a comprehensive literature review on MgB_2 superconductor, including the crystal and electronic structure, effect of carbon doping on the superconducting performance, and the effects of pressure on MgB_2. Chapter 3 contains the experimental procedures and equipment were used in this thesis. In Chapter 4, the carbon (C) substitution effects in co-doped MgB_2 bulk and wire samples of $Mg_{0.98}Al_{0.02}(B_{1-x}C_x)_2$ on the lattice parameters, critical temperature, resistivity, and magnetic and transport critical current density as a function of SiC doping level in the range from 0.5 wt% to 5 wt% with fixed 2 wt% alumina (Al_2O_3) are discussed. The co-doping composition of MgB_2 + 2 wt% Al_2O_3 + 1 wt% SiC resulted in both low and high field J_c enhancement compared to the pristine MgB_2 sample due to C-substitution, small grain size, and improved grain connectivity.

To date, various approaches have been adopted previously by many research groups to improve MgB_2 performance intrinsically by introducing carbon into MgB_2 lattice structure, and among those methods, the most popular techniques are solid state mixing[40] and the chemical solution

route[41]. In the case of solid state mixing, nano-size precursors, such as SiC and C, are used, but usually nano-size precursor powders tend to be agglomerated during the mixing process. In addition, inhomogeneous mixing between precursors makes MgB_2 undergo complicated reaction or leads to unexpected impurity phases. Alternatively, the chemical solution route has been suggested, and the effect of carbohydrate, i.e., malic acid, introduced in this way on the MgB_2 superconducting material have been evaluated, demonstrating that this is one of the most successful techniques reported so far[39, 41, 42]. In this case, homogeneity of the carbon cannot be achieved up to the desired level. This is because there is no definitive control during this process due to the high volatility of the liquid hydrocarbon. Recently, Susner *et al.* investigated and reported a more efficient carbon-doping method[43], with the product called pre-carbon doped boron, resulting in enhancement of the irreversibility field (B_{irr}) and the upper critical field (B_{c2}) when it was used in MgB_2 superconductor. In their method, they used boron that was amorphous, but with some monocrystalline nature, synthesised by the radio frequency (RF) plasma method[44, 45]. In this process, however, residual BCl_3 adsorbed on the powder particles can react with the humidity in air[46], which is detrimental to the performance of the superconductor. To overcome existing problems a cost effective carbon doping method have been reported in Chapter 5.

In chapter 6, an economical fabrication concept through localized internal magnesium diffusion (LIMD) method has been discussed. Instead of using a single magnesium (Mg) rod in the centre of a metal sheath tube, large-sized Mg particles (20-50 mesh) mixed well with cheap 97% crystalline boron powder were used in this process. After a repeated drawing process, the coarse Mg is elongated along the core wire axis of the metal sheath tube. Textured MgB_2 grains were then formed during the sintering process. In the LIMD process, however, there was still a need to improve the overall density. In order to increase the density of the composite, a

modified cold high pressure densification (CHPD) technique has been applied before the reaction.

In Chapter 7, further improvement was done by using cheap amorphous boron discussed that one in Chapter 5. To improve the in-field performance of MgB_2 conductor, combined intrinsic and extrinsic approaches have been adopted. Hot isostatic pressing was applied during the heat treatment process to improve connectivity. Chapter 8 contains the conclusions and suggestions for further improvements of the MgB_2.

1.5 References

1. W. Buckel and R. Kleiner, *Superconductivity: Fundamentals and Applications*, 2nd ed. (WILEY-VCG Verlag GmbH & Co. KGaA, Weinheim, 2004).

2. A. C. Rose-Innes and E. H. Rhoderick, *Introduction to Superconductivity,* 2nd ed. (Oxford: Pergamon Press, England, 1969).

3. A. M. Forrest, European Journal of Physics **4** (2), 117-120 (1983).

4. C. A. Reynolds, B. Serin, W. H. Wright and L. B. Nesbitt, Phys Rev **78** (4), 487-487 (1950).

5. E. Maxwell, Phys Rev **79** (1), 173-173 (1950).

6. J. G. Bednorz and K. A. Muller, Z Phys B Con Mat **64** (2), 189-193 (1986).

7. A. Schilling, M. Cantoni, J. D. Guo and H. R. Ott, Nature **363** (6424), 56-58 (1993).

8. J. Nagamatsu, N. Nakagawa, T. Muranaka, Y. Zenitani and J. Akimitsu, Nature **410** (6824), 63-64 (2001).

9. K. Vinod, R. G. A. Kumar and U. Syamaprasad, Supercond Sci Tech **20** (1), R1-R13 (2007).

10. Z. A. Ren, J. Yang, W. Lu, W. Yi, X. L. Shen, Z. C. Li, G. C. Che, X. L. Dong, L. L. Sun, F. Zhou and Z. X. Zhao, Epl-Europhys Lett **82** (5), 57002 (2008).

11. Z. Wei, H. O. Li, W. L. Hong, Z. M. Lv, H. Y. Wu, X. F. Guo and K. Q. Ruan, J Supercond Nov Magn **21** (4), 213-215 (2008).

12. F. Ishikawa, N. Eguchi, M. Kodama, K. Fujimaki, M. Einaga, A. Ohmura, A. Nakayama, A. Mitsuda and Y. Yamada, Phys Rev B **79** (17), 172506 (2009).

13. R. Mankowsky, A. Subedi, M. Forst, S. O. Mariager, M. Chollet, H. T. Lemke, J. S. Robinson, J. M. Glownia, M. P. Minitti, A. Frano, M. Fechner, N. A. Spaldin, T. Loew, B. Keimer, A. Georges and A. Cavalleri, Nature **516** (7529), 71-73 (2014).

14. A. B. Pippard, Proceedings of the Royal Society of London A: Mathematical, Physical and Engineering Sciences **216** (1127), 547-568 (1953).

15. O. V. Shcherbakova, A. V. Pan and S. X. Dou, *Manesium diboride supercoductors: Development and properties*, 1st ed. (VDM Verlag Dr. Muller Aktiengesellschaft & Co. KG and licensors, Germany, 2009).

16. J. H. Kim, S. Oh, Y. U. Heo, S. Hata, H. Kumakura, A. Matsumoto, M. Mitsuhara, S. Choi, Y. Shimada, M. Maeda, J. L. MacManus-Driscoll and S. X. Dou, Npg Asia Mater **4**, E3 (2012).

17. C. Buzea and T. Yamashita, Supercond Sci Tech **14** (11), R115-R146 (2001).

18. E. W. Collings, M. D. Sumption, M. Bhatia, M. A. Susner and S. D. Bohnenstiehl, Supercond Sci Tech **21** (10), 103001 (2008).

19. M. K. Wu, J. R. Ashburn, C. J. Torng, P. H. Hor, R. L. Meng, L. Gao, Z. J. Huang, Y. Q. Wang and C. W. Chu, Physical Review Letters **58** (9), 908-910 (1987).

20. http://www.superconductors.org/.

21. J. Jian-Ming, Antennas and Propagation Magazine, IEEE **40** (6), 7-22 (1998).

22. Y. Iwasa, D. C. Larbalestier, M. Okada, R. Penco, M. D. Sumption and X. Xiaoxing, Applied Superconductivity, IEEE Transactions on **16** (2), 1457-1464 (2006).

23. Y. Iwasa, Physica C: Superconductivity and its Applications **445-448** (1-2), 1088-1094 (2006).

24. W. J. Yao, J. Bascunan, S. Y. Hahn and Y. Iwasa, Ieee T Appl Supercon **20** (3), 756-759 (2010).

25. Y. Iwasa, J. Bascunan, S. Hahn and D. K. Park, Physcs Proc **36**, 1348-1353 (2012).

26. Y. S. Hascicek, Y. Akin, T. W. Baldwin, M. M. Rindfleisch, J. Yue, M. D. Sumption and M. Tomsic, Supercond Sci Tech **22** (6), 065002 (2009).

27. K. Kajikawa, Y. Uchida, T. Nakamura, H. Kobayashi, T. Wakuda and K. Tanaka, Ieee T Appl Supercon **23** (3), 5201604 (2013).

28. M. Tomsic, M. Rindfleisch, J. Yue, K. McFadden, D. Doll, J. Phillips, M. D. Sumption, M. Bhatia, S. Bohnenstiehl and E. W. Collings, Physica C: Superconductivity and its Applications **456** (1-2), 203-208 (2007).

29. T. Tajima, N. F. Haberkorn, L. Civale, R. K. Schulze, H. Inoue, J. Guo, V. A. Dolgashev, D. W. Martin, S. G. Tantawi, C. G. Yoneda, B. H. Moeckly, C. Yung, T. Proslier, M. Pellin, A. Matsumoto and E. Watanabe, Advances in Cryogenic Engineering, Vol 58 **1435**, 297-304 (2012).

30. S. Nomura, S. Akita, R. Shimada and T. Shintomi, Ieee T Appl Supercon **16** (2), 590-593 (2006).

31. T. Shintomi, T. Asami, G. Suzuki, N. Ota, T. Takao, Y. Makida, T. Hamajima, M. Tsuda, D. Miyagi, M. Kajiwara and J. Hirose, Ieee T Appl Supercon **23** (3), 5700304 (2013).

32. M. Sander, R. Gehring and H. Neumann, Ieee T Appl Supercon **23** (3), 5700505 (2013).

33. Y. Oga, S. Noguchi and M. Tsuda, Ieee T Appl Supercon **23** (3), 5700204 (2013).

34. J. H. Kim, S. Oh, H. Kumakura, A. Matsumoto, Y. U. Heo, K. S. Song, Y. M. Kang, M. Maeda, M. Rindfleisch, M. Tomsic, S. Choi and S. X. Dou, Adv Mater **23** (42), 4942-4946 (2011).

35. X. P. Zhang, D. L. Wang, Z. S. Gao, L. Wang, Y. P. Qi, Z. Y. Zhang, Y. W. Ma, S. Awaji, G. Nishijima, K. Watanabe, E. Mossang and X. Chaud, Supercond Sci Tech **23** (2), 025024 (2010).

36. X. Xu, S. X. Dou, X. L. Wang, J. H. Kim, J. A. Stride, M. Choucair, W. K. Yeoh, R. K. Zheng and S. P. Ringer, Supercond Sci Tech **23** (8), 085003 (2010).

37. J. H. Lee, S. Y. Shin, C. J. Kim and H. W. Park, J Alloy Compd **476** (1-2), 919-924 (2009).

38. A. Kario, R. Nast, W. Hassler, C. Rodig, C. Mickel, W. Goldacker, B. Holzapfel and L. Schultz, Supercond Sci Tech **24** (7), 075011 (2011).

39. M. S. A. Hossain, C. Senatore, R. Flukiger, M. A. Rindfleisch, M. J. Tomsic, J. H. Kim and S. X. Dou, Supercond Sci Tech **22** (9), 095004 (2009).

40. S. X. Dou, O. Shcherbakova, W. K. Yeoh, J. H. Kim, S. Soltanian, X. L. Wang, C. Senatore, R. Flukiger, M. Dhalle, O. Husnjak and E. Babic, Physical Review Letters **98** (13), 139902 (2007).

41. J. H. Kim, S. Zhou, M. S. A. Hossain, A. V. Pan and S. X. Dou, Appl Phys Lett **89** (14), 142505 (2006).

42. J. H. Kim, S. X. Dou, S. Oh, M. Jercinovic, E. Babic, T. Nakane and H. Kumakura, J Appl Phys **104** (6), 063911 (2008).

43. M. A. Susner, Y. Yang, M. D. Sumption, E. W. Collings, M. A. Rindfleisch, M. J. Tomsic and J. V. Marzik, Supercond Sci Tech **24** (1), 012001 (2011).

44. J. V. Marzik, R. C. Lewis, M. R. Nickles, D. K. Finnemore, J. Yue, M. Tomsic, M. Rindfleisch and M. D. Sumption, AIP Conference Proceedings **1219** (1), 295-301 (2010).

45. J. V. Marzik, R. J. Suplinskas, R. H. T. Wilke, P. C. Canfield, D. K. Finnemore, M. Rindfleisch, J. Margolies and S. T. Hannahs, Physica C: Superconductivity and its Applications **423** (3-4), 83-88 (2005).

46. S. J. Ye, M. H. Song, A. Matsumoto, K. Togano, M. Takeguchi, T. Ohmura and H. Kumakura, Supercond Sci Tech **26** (12), 125003 (2013).

CHAPTER 2: LITERATURE REVIEW

2.1 Crystal structure

The MgB_2 unit cell occurs in the simple hexagonal AlB_2-type structure, a very common structure among borides, with the space group P6/mmm. The crystal structure of MgB_2 consists of two honeycomb boron layers like graphite type sheets with a base diameter of nearly 3.5 Å[1]. This creates large spherical pores for magnesium. In the MgB_2 compound, magnesium atoms are located at the center of hexagons created by boron planes. The crystal structure of MgB_2 is depicted in Figure 2.1[2]. All the intense peaks can be indexed assuming an hexagonal unit cell, with a = 3.086 Å (distance between in-plane Mg-Mg) and c = 3.524 Å (distance between Mg layers)[2]. Due to the hexagonal structure and relatively longer distance between the boron planes than in-plane B-B distance of MgB_2, it shows a strong anisotropy in the B-B lengths[3-5]. The room temperature X-ray diffraction (XRD) pattern of MgB_2 is depicted in Figure 2.2[2].

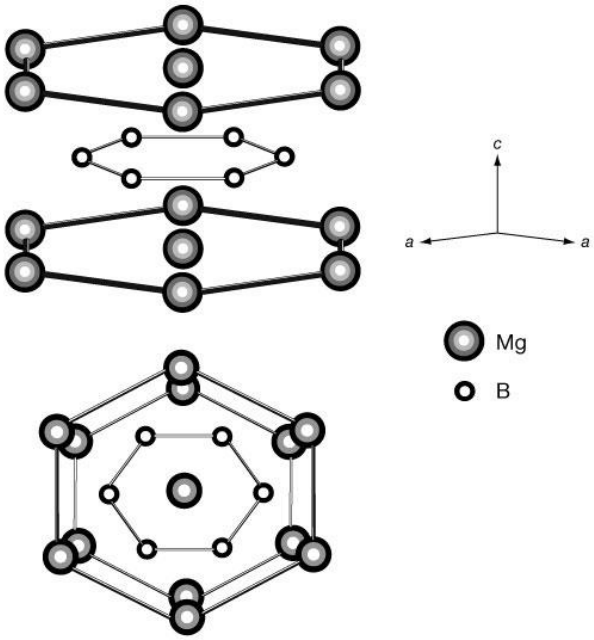

Figure 2.1 Crystal structure of MgB_2[2]

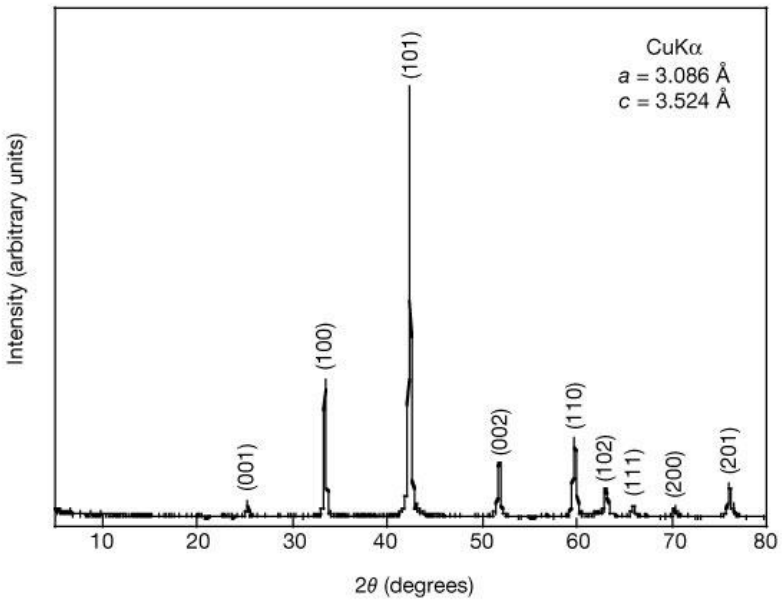

Figure 2.2 X-ray diffraction (XRD) pattern of MgB_2 at room temperature[2]

2.2 Electronic structure

At the Fermi surface of MgB_2, the electrons are predominantly *p* electrons of boron along with magnesium donating *s* electrons to the conducting bands[1, 6, 7]. Four conducting bands are in there, consisting of two σ bands derived from the σ–bonding $p_{x,y}$ orbitals of boron and two π bands, which are derived from the hole-like π-binding and electron-like antibonding p_z orbitals. The two-dimensional σ states are confined in the boron planes and the three-dimensional π states are extending in all the direction[1, 3]. The in-plane bonds of boron layers are strongly covalent; contrarily the bonds in between these layers are metallic[8]. The Fermi surface of MgB_2 is depicted in Figure 2.3.In here, Γ, L, A and M are sites in Brillouin zone for positioning of σ and π bands in Fermi surface. The two coaxial cylinders along Γ- A line are σ-bands in MgB_2 structure, while the π- bands form two the two webbed tunnels, near H and L, one hole like near K and M[1]. The superconductivity in MgB_2 is the result of asymmetric charge distribution in the σ-bonding with the presence of in-plane boron atoms, which provides sufficiently strong

coupling between the in-plane vibration of boron atom and the σ-bonding state[5, 9]. At the Fermi level the density of states are0.30 states eV^{-1}/cell for the two σ-bands, whereas 0.410 states eV^{-1}/cell for the two π- bands[8, 10].

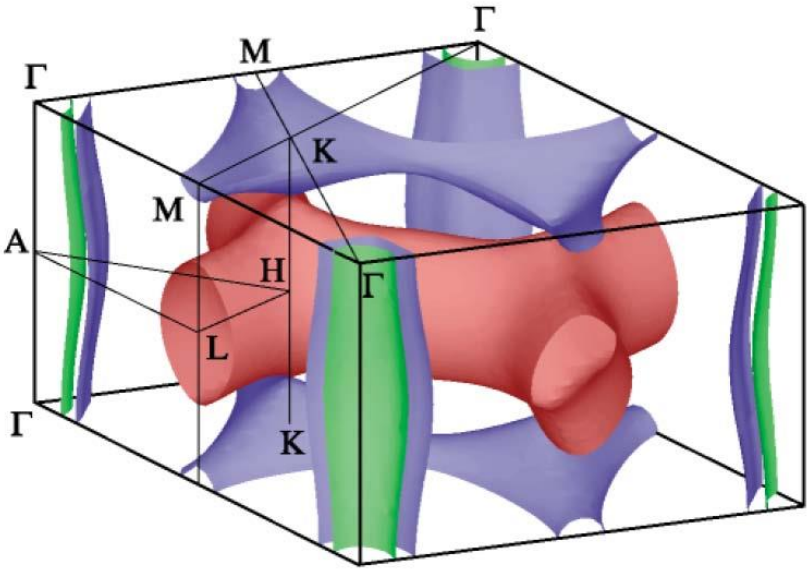

Figure 2.3 The Fermi surface of MgB_2. Green and blue cylinders (hole like) come from the bonding $p_{x,y}$ bands, the blue tubular network (hole like) from the bonding p_z bands, and the red (electron like) tubular network from the antibonding p_z band[1].

2.3 Two-gap superconductivity

In MgB_2 superconductor, the electronic states at the Fermi level, which are known as the highest occupied electronic states, are primarily either σ- or π-bonding boron orbitals. The electronic states at Fermi level and vibrational mode of boron atoms are depicted in **Figure 2.4**[3]. With respect to the in-plane positions of boron atoms in the MgB_2, the distribution of charge of the σ-bonding states are not symmetrical[3]. The couplings of σ-bonding states to in-plane vibration of boron atoms are very strong, which results a unique partially occupied sigma-bonding states in a layer structure[3]. But the electron-phonon coupling is weaker for the π bands. Moreover, inter-band coupling is even weaker, though it is not negligible[11].

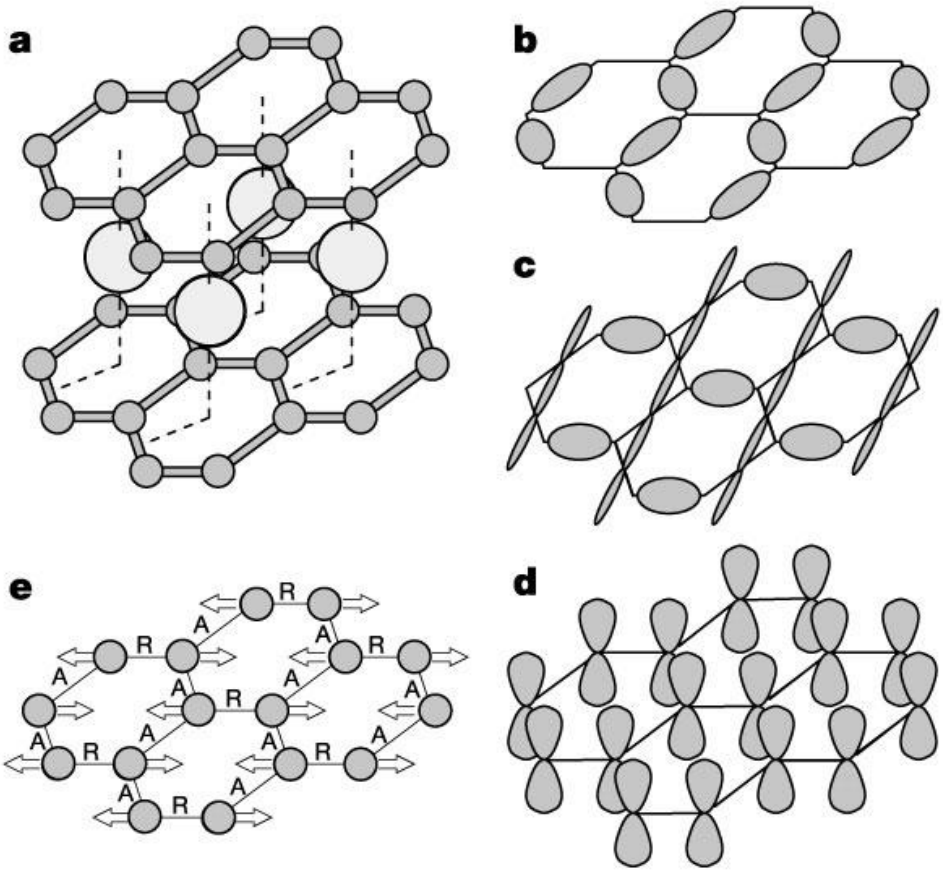

Figure 2.4 Crystal structure of MgB_2, electronic states at the Fermi level, and a vibrational mode of boron atoms. **a)** Crystal structure of MgB_2. Boron atoms form honeycomb planes, and magnesium atoms occupy the centers of the hexagons in-between boron planes, **(b, c)** sigma-bonding states at the Fermi level derived from boron $p_{x,y}$ orbitals, **d)** A π-bonding state at the Fermi level derived from boron p_z orbitals. **e)** A vibrational mode of boron atoms that couples strongly to sigma-bonding electronic states at the Fermi level. As boron atoms move in the arrow directions, shortened bonds, marked with 'A', become attractive to electrons, whereas elongated bonds, marked with 'R', become repulsive. The sigma-bonding states **(b, c)** couple strongly to the vibrational mode because they are mainly located in either the attractive or the repulsive bonding of the mode. The π-bonding states **(d)** do not couple strongly to this mode[3].

The superconducting energy gap and critical temperature have been calculated based on the information of electron-phonon coupling and Columb pseudo-potential matrix elements [10, 12]. In **Figure 2.5,** experimental results of the two gaps in MgB_2 are depicted from the scanning tunneling spectroscopy as a function of temperature[13].

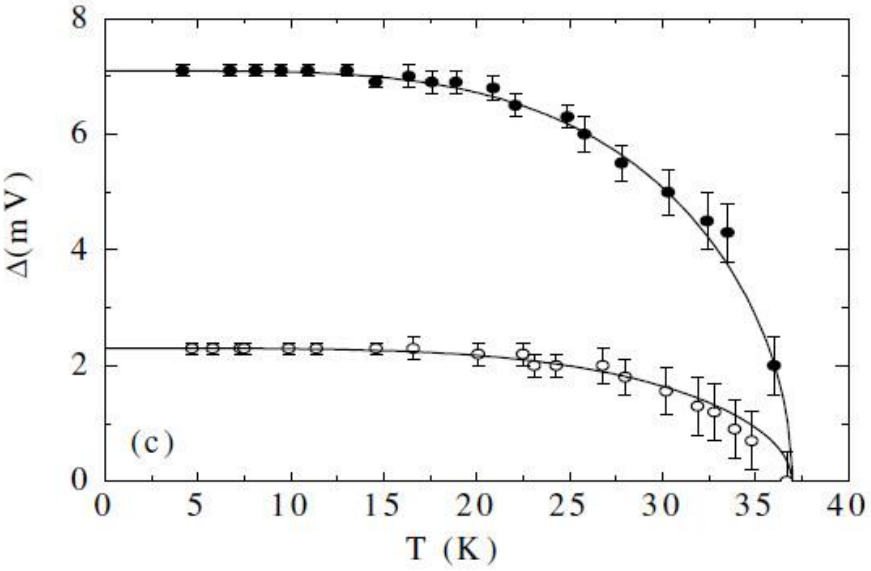

Figure 2.5 The superconducting gap values are extracted from the theoretical curves and are plotted as a function of the temperature together with the BCS Δ (*T*)[13].

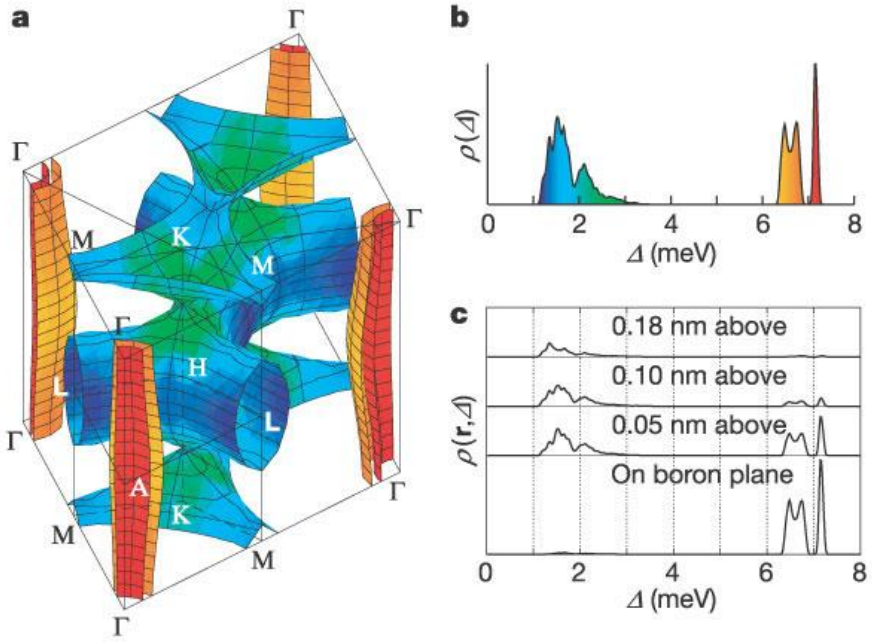

Figure 2.6 The superconducting energy gap on the Fermi surface at 4 K given using a color scale (a), and the distribution of gap values at 4 K (b). The Fermi surface of MgB_2 consists of four distinctive sheets. Two sigma sheets ('cylinders'), derived from the sigma-bonding $p_{x,y}$ orbitals of boron, are shown split into eight pieces around the four vertical Gamma–Gamma lines. Two π sheets ('webbed tunnels'), derived from the π-bonding p_z orbitals of boron, are shown around K–M and H–L lines. **c)** Local distribution of the superconducting energy gap on a boron plane and on planes at 0.05, 0.10 and 0.18 nm above a boron plane, respectively[3].

A details study of superconducting energy gaps of MgB_2 at low temperature on Fermi surface has been done by Choi *et al.*[3], using Eliashberg formalism. In **Figure 2.6,** the superconducting energy gap on the Fermi surface for MgB_2 from the band structure calculation is depicted[3]. At the Fermi surface, each π-band and σ-band has characteristic energy gaps for MgB_2. It ranges from ranges from 6.4 to 7.2 meV on the σ bands with an average of 6.8 meV, and on the other hand π-bands, it varies from 1.2 to 3.7 meV with an average of 1.8 meV[3].

2.4 Experimental evidences of two gaps and two bands

Disparate experimental investigation using tunneling spectroscopy[14, 15], specific heat measurement[10, 16, 17], point contact tunneling[15] etc. established the existence of the two-gap superconductivity in MgB_2. The first experimental evidence of two-band superconductivity came out from the study of specific heat measurement[16-18].

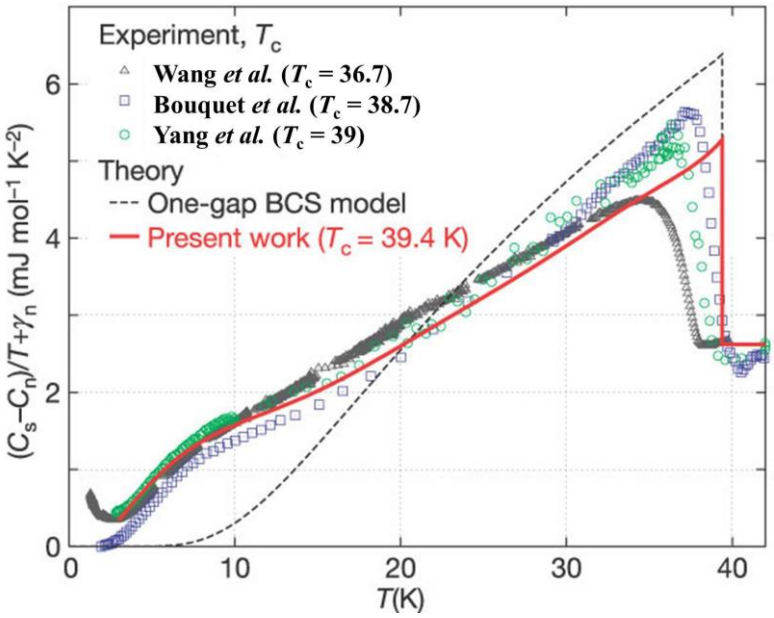

Figure 2.7 Specific heat measurement of MgB_2.The measured and calculated electronic contribution to the specific heat divided by temperature is plotted as a function of temperature. Here, (C_s - C_n) is the specific heat difference between the superconducting and normal states. The red solid curve represents the calculated result and the dashed curve is the standard one-gap BCS prediction corresponding to a transition temperature of 39.4 K[3].

The specific heat is plotted as a function of temperature is depicted in **Figure 2.7**. Choi *et al*[3]

proved that the empirical data of specific heat cannot be clarified by the one-gap BCS model with a T_c of 39.4K. The experimental result found is higher than the BCS curve at low temperature and the low temperature shoulder is an indication of a smaller second gap, which is resulted by the excitations along the π gap[3].

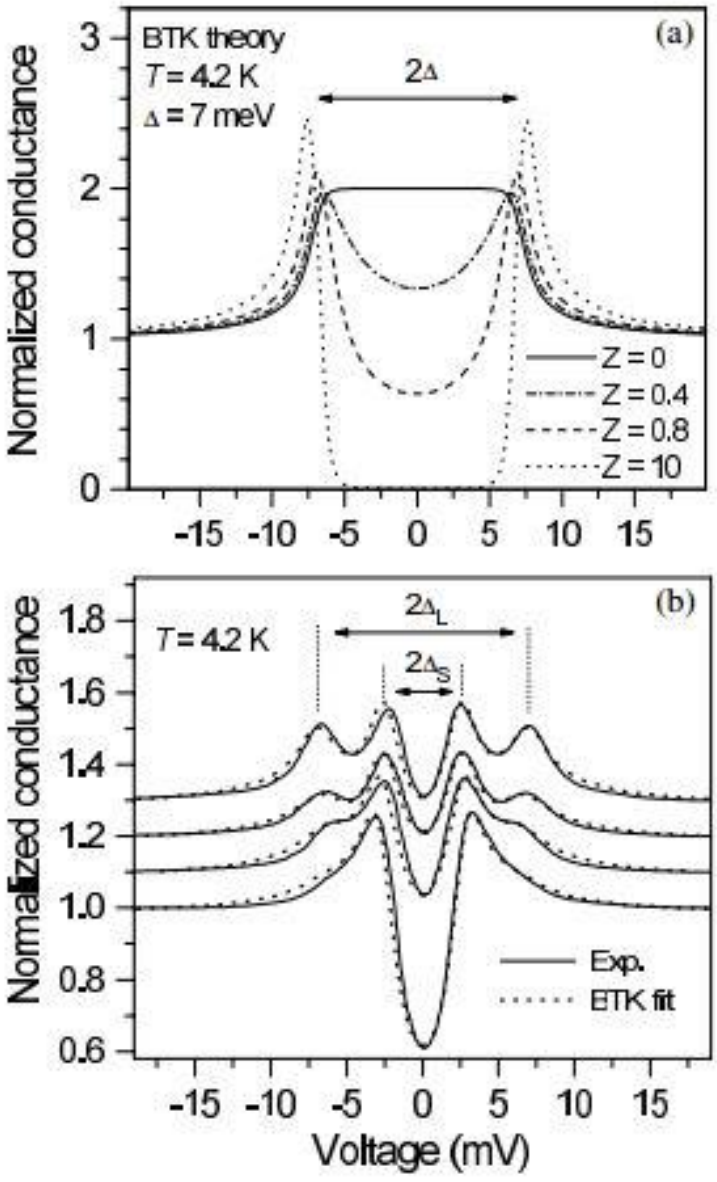

Figure 2.8 a) Numerical simulation of the Blonder–Tinkham–Klapwijk (BTK) model at different values of the barrier strength Z at 4.2 K. **b)** Experimentally detected evolution of the Cu-MgB_2 point-contact spectra at 4.2 K (solid lines). The dotted lines display fitting results for the thermally smeared BTK model for different barrier transparencies and weight factors[19].

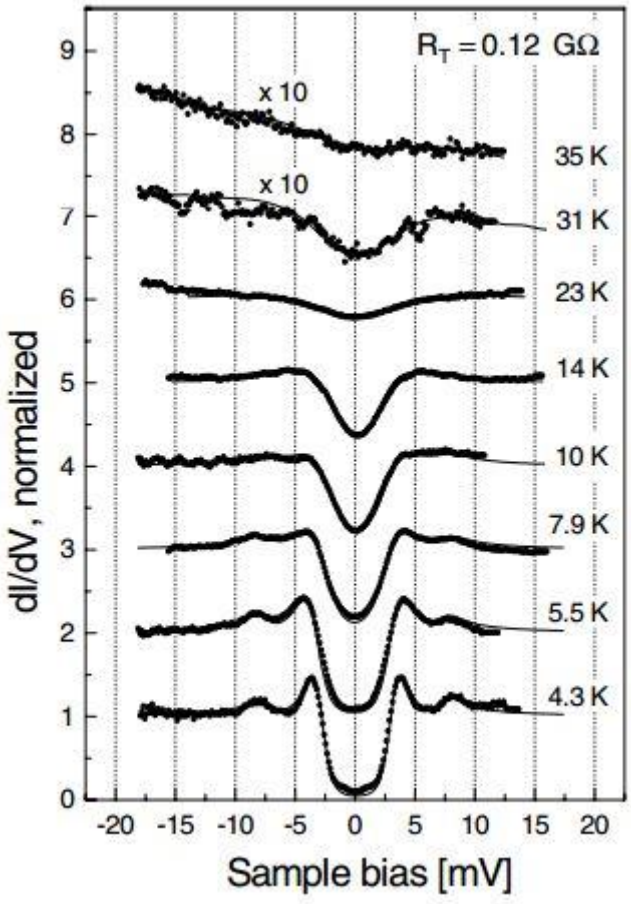

Figure 2.9 Temperature dependence of tunneling conductance spectra in the range between 4.3K and 35K. All experimental curves (black dots) are fitted by a sum of two weighted BCS-shape DOS (solid lines). The spectra are shifted by unity for clarity. The curves at 31 K and 35K are reported magnified by a factor of 10[23].

Different direct measurements of superconducting gap by point contact spectroscopy[19-22] and tunneling spectroscopy[13, 23, 24] also proved the two gap superconductivity in MgB_2. Szabo *et al*[19] investigated the Cu–MgB_2 point-contact spectra on different samples of polycrystalline MgB_2 at 4.2K. **Figure 2.8(a)** shows the numerical simulation of the Blonder-Tinkham-Klapwijk (BTK) model at different values of the barrier strength Z at 4.2 K and **Figure 2.8(b)** shows the experimentally observed evolution of the Cu-MgB_2 point-contact spectra at 4.2 K (solid lines)[19]. From the g scanning tunneling spectroscopy, Giubileo *et al.* showed the temperature dependence of tunneling conductance spectra in the range between 4.3K and 35 K[23]., which is depicted in **Figure 2.9**.

Chen *et al*.[25] measured the Raman spectra at two polarization configurations, VV and HV, where VV (HV) denotes the scattering geometry with the polarization direction of the incident light in vertical (horizontal), and the polarization direction of the scattered light is always vertical for scattered light. **Figure 2.10** depicts the Raman spectra from a poly crystalline MgB_2 sample[25]. Here, the two peaks is a result of superconducting transition, known as pair breaking peaks at about 50 cm^{-1} and 105 cm^{-1}. The frequency, at which pair-breaking peak appears, is a direct measure of the binding energy of the Cooper pairs. The binding energy is twice the gap value ($2\Delta_\pi$ and $2\Delta_\sigma$) [25]. The gap measured from the experiment are $\Delta_\sigma = 7.1$ meV and $\Delta_\pi = 2.3$ meV. Two pair-breaking peaks in the Raman spectra is also another evidence of two superconducting gaps in MgB_2.

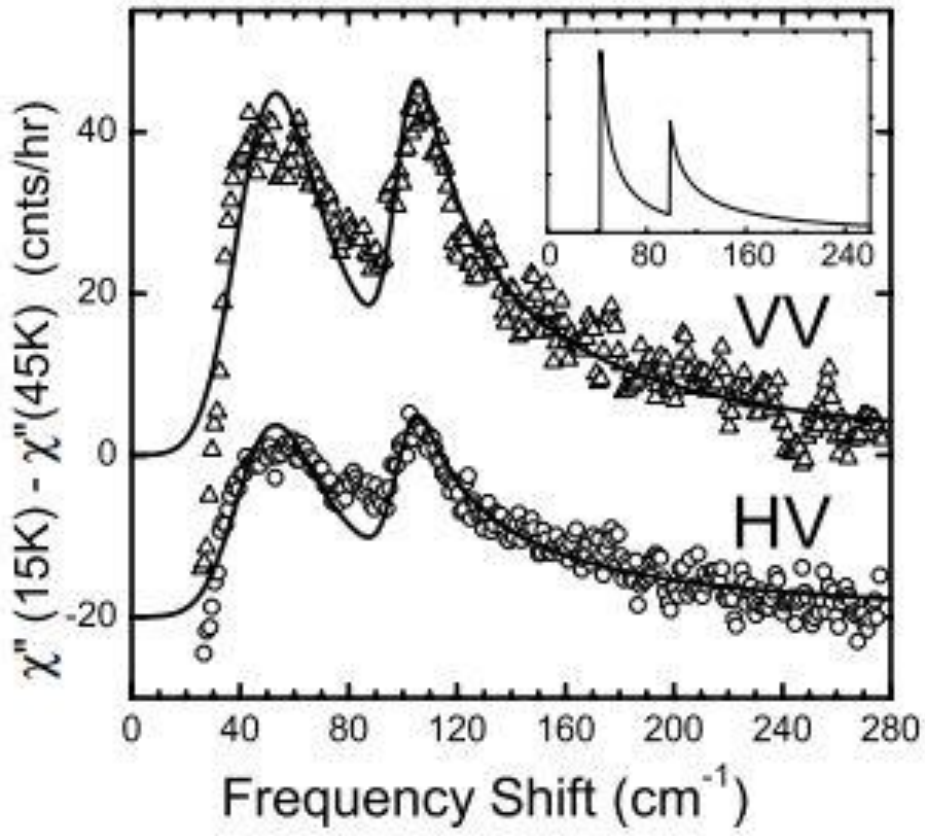

Figure 2.10 Low-temperature electronic Raman continua obtained by subtracting the 45K spectra from the 15K spectra. The thick solid lines are theoretical fits. The HV spectra have been shifted downward by 20 units. The inset is a calculated spectrum without convoluting

with a Gaussian function[25].

Disparate studies on photoemission spectroscopy also suggested the existence of two gaps[26-28] and two band[29] in MgB_2. High-resolution photoemission spectra of MgB_2 measured at two different states by Tsuda *et al* is depicted in **Figure 2.11**[26]. The inset of **Figure 2.11** shows the enlarged spectrum near E_F taken at 5.4 K. It is the weighted sum of two Dynes functions with the gap sizes of 1.7 meV (broken line) and 5.6 meV (dotted line). These results provide clear spectroscopic evidence for presence of multiple gap in MgB_2[26]. In 2003, the two gap of MgB_2 superconductor have been measured by using angle resolved photoemission spectroscopy (ARPES)[27, 28].

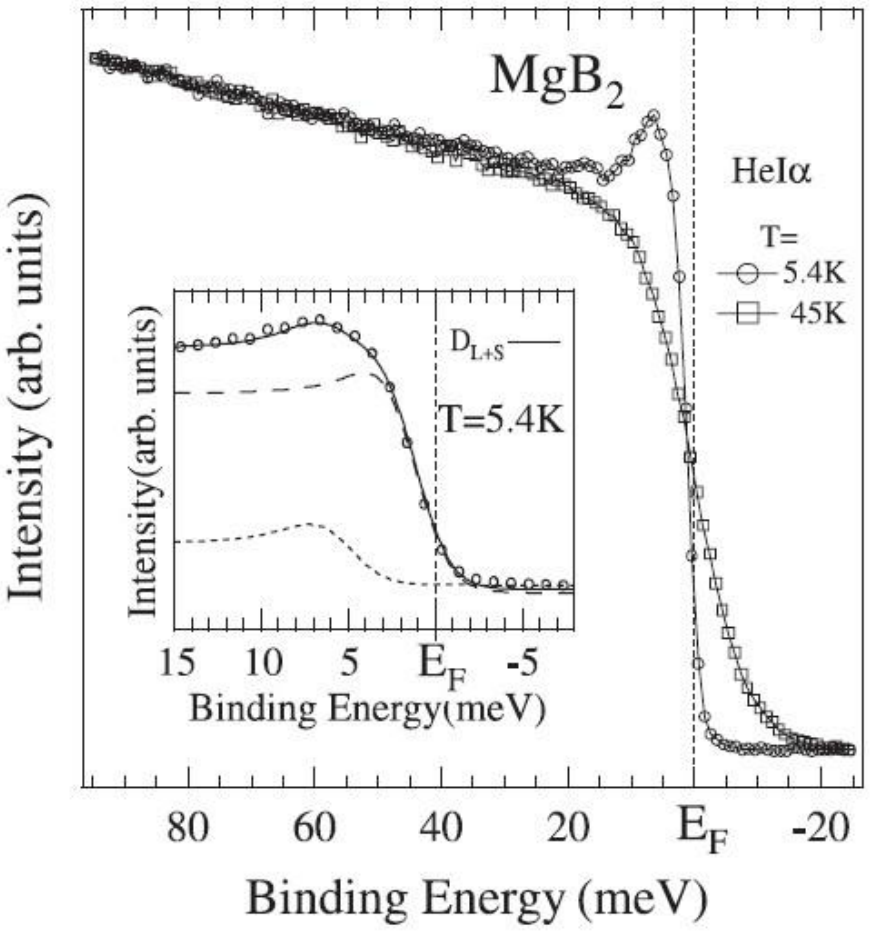

Figure 2.11 High-resolution photoemission spectra of MgB_2 measured at 5.4 K (open circles connected with a solid line) and 45 K (open squares connected with a solid line). The inset shows the enlarged spectrum near E_F taken at 5.4 K, which can be fitted by assuming two gaps

at 1.7 meV (broken line) and 5.6 meV (dotted line), respectively[26].

2.5 Critical temperature (T_c)

From the application perspective, critical temperature (T_c) is the most important parameter for superconducting material, which confines the application regime. The T_c of MgB_2 (39 K or -234 ºC) is the highest among the inter-metallic superconductors[2]. As the crystal structure has a significant impact on *Tc*, hence variation in lattice parameters affects *Tc*[30, 31]. Fabrication process which leads to changes in lattice volume, such as neutron irradiation[32, 33] or iso-static pressure [34-36] , are responsible for reduction of T_c. Furthermore, variation in stoichiometric ratio of starting materials, such as Mg deficiency could enhance the lattice strain, which leads to T_c decrement[37]. Another important factor is low crystallinity of MgB_2 which causes higher disorder in the lattice, decrease T_c[38].

2.6 Critical current (I_c) / critical current density (J_c)

Critical current (I_c) or critical current density (J_c) is the main characteristic parameter which determines the applicability of superconductor in practical applications. Due to high intra-grain and inter-grain J_c in MgB_2, it shows high transport J_c at low temperatures. The transport J_c reported in the wire/ tape geometry at 4.2 K is the order of 10^6 A cm^{-2} in self-field and it is around 10^4 A cm^{-2} at 8T filed[39]. In MgB_2 single crystal, the J_c is low due to weak pinning and rapid drop of J_c occurs with the magnetic field. The J_c in self-field is nearly 10^5 Acm^{-2} at low temperatures[40, 41]. On the other hand, thin films demonstrate much higher J_c than single crystals. This is because of their strong grain boundary pinning[40]. The highest value of J_c observed in thin films is around 3-4 × 10^7 Acm^{-2} in self-field[42-44].In **Figure 2.12** depicts the J_c of neutron irradiated single crystals (see **Figure 2.12 (a)**) and thin films (see **Figure 2.12 (b)**)[40]. The J_c of wires fabricated by the CTFF method shows the value around 6 × 10^5 Acm^{-2} at 4.2 K in self-field. The degradation of J_c with the applied magnetic field is more gradual than the single crystal and it shows J_c value around 10^5 Acm^{-2} with applied magnetic field 4.5 - 5 T, which is

below about an order of magnitude than the best thin film data[4]. From the comparison between the wires and tapes it can be seen that tapes shows superior performance than the wires due to their shielding property. The performance of MgB_2 is affected by disparate factors including quality of starting materials, size of Mg, presence of impurities, heat treatment condition, porosity, grain boundaries, and particle size distribution. Quality of starting materials (B and Mg) plays an important role on the performance of the conductor, as it is directly related to the grain size and connectivity of the final product, which determine the superconducting performance largely.

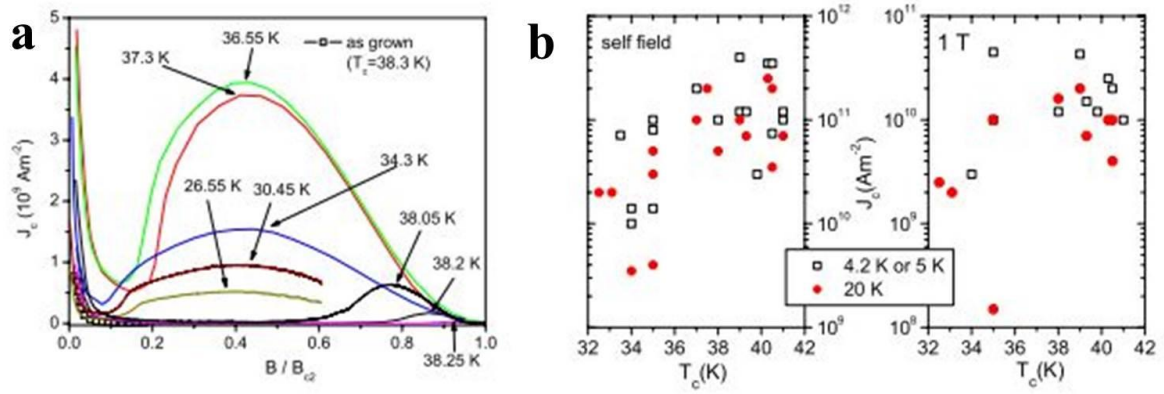

Figure 2.12 a) Critical current densities in neutron-irradiated single crystals. The introduced disorder is characterized by the transition temperature of the crystal, which decreases with increasing neutron fluence[45]. **b)** Critical current densities in thin films at 4.2 or 5 K (open squares) and at 20 K (solid circles). The left and the right panel of **(b)** refer to zero applied fields and 1 T (H∥c), respectively[40].

Zeng *et al.* reported that excess Mg in MgB_2 can significantly enhance the J_c by providing better grain connectivity compared to the stoichiometric MgB_2[39, 46, 47]. Fujii *et al.* studied the effect of Mg on transport J_c and showed that MgH_2 as the Mg source provides fresh and highly reactive Mg which facilitate the formation of high purity MgB_2[48]. Yamada *et al.* reported the transport J_c of MgB_2 tape by doping 10% SiC and using nano sized Mg powder, resulting a value of five times higher than the tapes prepared with the commercial Mg powder[49].

In the high temperature superconductors (HTS), the grain boundaries primarily act as weak

links which reduce the connectivity between the grains and the result is lower J_c. In case of in MgB_2 the grain boundaries are transparent to current flow which facilitates to improve the J_c by grain boundary pinning[50]. Producing very fine Mg and B powder mixture by ball milling results a significant enhancement of MgB_2 performance[51, 52]. Ball milling techniques is also proved to be a successful method for enhancing the J_c of *ex-situ* MgB_2 by minimizing the grain size and subsequently increase the grain boundaries, which leads to higher J_c in MgB_2[53].

Presence of porous structure in MgB_2 conductor is one of the limiting factors for reducing the transport J_c[54]. In *in-situ* process it is hard to fabricate dense MgB_2 structure due to the low packing density of the powder. Volume contraction of MgB_2 after heat treatment and evaporation of Mg are another problem responsible for porosity. In *ex-situ* process, porosity is originated from the low packing density of the powder. Though, it is minimized by final high temperature heat treatment[55-57]. Several studies have been carried out to find out the effect of boron source on resistivity, critical current density and phase transformation[58-60]. Crystalline and amorphous, which are two different structure of boron powder, leads to two different J_c values. Compared to the samples made from amorphous precursors, an order of magnitude lower J_c is obtained from the samples made from the crystalline boron powders. Zhang *et al.* showed significant enhancement of J_c by using ball-milling of crystalline boron powder[61]. The enhancement of J_c came from higher reactivity of finer powder and results in better strong flux pinning and connectivity. Systematic studies on crystalline boron powder by using ball milling have been done[62, 63]. Disparate studies on the ball milling medium showed that toluene is the most promising wet medium among the carbon content organic solvents[64-66]. Yamamoto *et al.* reported the systematic study on the relationship between the irreversibility field and the crystallinity, and their influence on the J_c by full width half maximum (FWHM) value obtained from the X-ray diffraction[67]. The FWHM value of the (002) peak reflects the out-of-plane disorder; whereas the FWHM value of (110) peak represents the in-plane disorder[67].

Larger value of FWHM is attributed to the lower crystallinity due to low heat treatment condition or disorder in crystal lattice. Intra-granular precipitates and different types of lattice defects are responsible for crystal lattice disorder and leads to degradation of crystallinity[67]. Since the grain size and lattice strain control the grain boundary pinning, hence lattice distortion and small crystal size improve the grain boundary pinning force.

2.7 Upper critical field (H_{c2})

Type-II superconductors have two characteristic critical fields, defined as the lower critical field (H_{c1}) and the upper critical field (H_{c2}). This intrinsic property is defined by the B, T phase boundary between the normal and superconducting states of a type II superconductor. The behavior of MgB_2 is mostly interesting, because adding nonmagnetic impurities enhance the upper critical field (H_{c2})[68-70]. Which is above the estimated $H_{c2}(0) = 0.69T_cH'_{c2}$ (T_c) of one-gap theory[71]. From the one-gap theory it is evident that, H_{c2} can be increased by adding impurities in superconductor, which is attributed to increase of normal state resistivity ρ_n. For better understanding of two band MgB_2 superconductor, Gurevich *et al.* suggested to a weakly-coupled bilayer model (see **Figure 2.13**) and at low temperature, H_{c2} of MgB_2 can be significantly enhanced by making the π band much dirtier than the main σ band[72]. As depicted in **Figure 2.13**, the global H_{c2} of the bilayer is controlled by the layer which has the higher H_{c2}[73]. With a dirtier π layer, it will have greater H_{c2} at low temperature, even if its Tc is much lower. At low temperature, this results an upturn in the global H_{c2}[72]. In carbon-doped thin films (see **Figure 2.14**), the value of H_{c2} has reached more than 60 T at low temperature, chasing the BCS paramagnetic limit of 65 T[73, 74]. Gurevich et al. argued that the strong coupling paramagnetic limit can be as much as 130 T in MgB_2[72]. This indicates the potentials scope of improving further of H_{c2} by engineering the two band scattering.

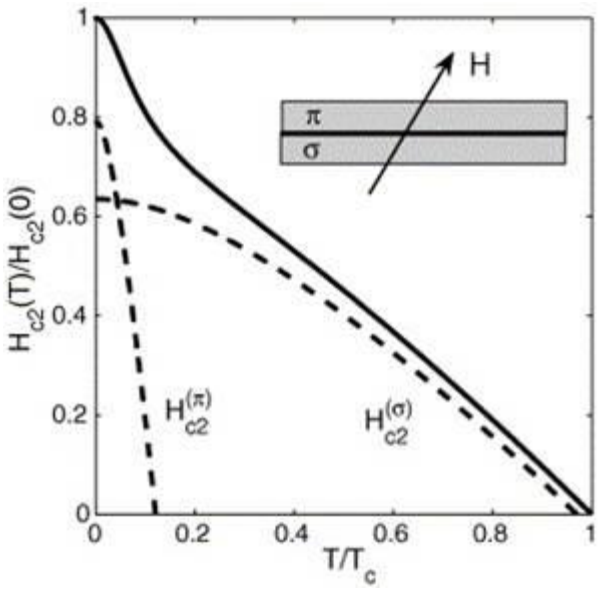

Figure 2.13 The mechanism of the upward curvature of H_{c2} (T) illustrated by the bilayer toy model shown in the inset. The dashed curves show H_{c2} (T) calculated for σ and π films in the one-gap dirty limit. The solid curve shows H_{c2} (T) calculated from two-gap dirty limit BCS theory[72].

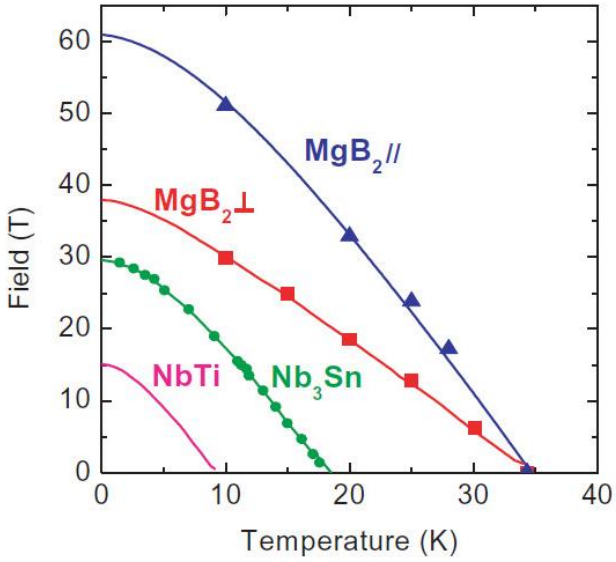

Figure 2.14 H_{c2} versus temperature plots for a carbon-alloyed HPCVD film, Nb–Ti (bulk) and Nb_3Sn (bulk). The triangle and square data are for the *ab* planes of MgB_2 parallel and normal to the field, respectively[7].

2.8 Resistivity

The resistivity of MgB_2, as reported in single crystal, thin film, polycrystalline bulk, and wire samples, fluctuates in orders of magnitude. According to their resistivity value at 300 K, it can be divided into four categories: (1) low resistivity - less than 20 μΩcm, (2) intermediate

resistivity—near 100 μΩcm, (3) high resistivity—500 μΩcm to 10 mΩ cm and (4) extreme resistivity—above 100 mΩcm[75]. Eltsev *et al.* reported the resistivity of single crystal, 1.0 mΩcm at 50 K, and 5.3 mΩcm at 300 K[76, 77]. Canfield *et al.* reported the resistivity of polycrystalline bulk 9.6 and 0.4 mΩcm at 300 and 50 K, respectively[78]. Pogrebnyakova *et al.* reported thin film resistivity, which are similarly low. The values are around 8.7 and 0.26 mΩcm4 at 300 and 50 K, respectively[79]. In some polycrystalline bulk sample Rogado *et al.* found the resistivity near 610 and 480 mΩcm at 300 and 50 K, respectively[80]. Wide ranges of resistivity for MgB_2, reported by different researchers have been accumulated by Rowel *et al.* in his review article, covering all the sample types from bulk to thin films[75].

Resistivity is influenced by the inter-grain and intra-grain effects. Factor affecting connectivity between the grains (inter-grain effect) are the presence of MgO and BO_x in the grain boundaries, porosity, presence of free Mg. Excess Mg is responsible for low resistivity in Mg rich sample. Similarly, impurities present within the grains as isolated small precipitates can increase intra-grain resistivity. Other impurities within the MgB_2 grains as inclusion, or which substituted in the MgB_2 lattice, increase the intra-grain resistivity[75]. One such potential impurity is carbon.

The contributing phenomena of the normal state resistivity in metal are temperature independent residual resistivity,ρ_0 and the phonon-mediated contribution, ρ_{ph} . Residual resistivity originates from the electron scattering at defects and ρ_{ph} is a function of temperature[40].

$$\rho(T) = \rho_0 + \rho_{\mathrm{ph}}(T)$$

In single-band conductors ρ_0 increases with disorder and ρ_{ph} remains constant. For two-band conductors, the resulting resistivity is governed by the following relation.

$$\frac{1}{\rho(T)} = \frac{1}{\rho_\sigma(T)} + \frac{1}{\rho_\pi(T)}$$

At low temperatures, the resistivity is affected by electron scattering at both σ- and π-bands. Contrarily, at room temperature electron scattering at the π- band controls the resistivity value. Introduction of defects into the MgB_2 crystal structure reduce the mean free path of the charge carriers in both bands[75]. The normal state resistivity is related to scattering time τ, the mean free path $l = \nu_F\tau$, the scattering rate $\Gamma = 1/\tau$ and the diffusivity *D*.

$$\rho = \frac{\Gamma}{\epsilon_0\omega_p^2} = \frac{\nu_F}{\epsilon_0\omega_p^2 l} = \frac{1}{e^2 N_0 D}$$

Here, the vacuum permeability $\epsilon_0 = 8.854\times10^{-12}$ $AsV^{-1}m^{-1}$, Fermi velocity ν_F, plasma frequency ω_p and the density of states (DOS) at the Fermi level N_0. Sidorenko *et al.* proposed a model to calculate the resistivity near the superconducting transition point based on the assumption that resistance is caused by the creep of vortices. Therefore, resistivity dependences are thermally activated[81]. The relationship is:

$$\rho(T,B) = \rho_0 \exp\left[\frac{-U_0}{k_B T}\right]$$

Where, U_0 is the flux-flow activation energy, mechanism in MgB_2, which can be extracted from the slope of the linear part of the Arrhenius plot[81], k_B is the Boltzmann's constant, and ρ_0 is a field independent pre-exponential factor.

2.9 Flux pinning and doping mechanisms

MgB_2 samples (films, bulks, and wires) except the single crystal sample are polycrystalline and moderately grain-boundary pinned. Hence, effects of dopant inclusion contribute to enhance the bulk pinning strength, (1) by increasing the H_{c2} and $H_{irr;}$ (2) by forming wide distribution of point pinning centers; (3) by producing localized lattice strains[4]. All these factors contribute to flux pinning. Structural defects such as dislocations, inclusions, impurities, and grain

boundaries effectively pin vortices at atomic sites. When, the size of the structural defect roughly matches with the size of the vortices, it becomes very effective pinning centers. Each vortex is assumed to be act individually, and the global pinning force is just the direct summation of the individual forces[82]. Disparate studies found that grain boundaries are the most dominant pinning centers in MgB_2 superconductor[64, 83, 84]. In an applied field *H*, the behavior and magnitude of J_c is delineated by a bulk pinning function, F_P. This function represents the summation of the elementary pinning forces, f_P [85]. The bulk pinning force density can be expressed as:

$$F_P = H_{c2}^m f(h) \qquad \text{where } h = H/H_{c2}$$

The field dependence bulk pinning force generally rises to a maximum value at $h = h_{max}$ and expressed in normalized form $F_p(h)/F_p(h_{max})$. This is independent of temperature for specific type of pinning center and it is known as scaling property[4]. According to the pinning mechanism model of Dew-Hughes[82], $f(h) \propto h^p(1-h)^q$ and various types of pinning can be classified based on the value of dimensionless parameter *p,q*. hence,

$h^0(1-h)^2 \rightarrow$ Normal volume pinning $d < a, b, c$

$h^{1/2}(1-h)^2 \rightarrow$ Normal surface (grain boundary) pinning $d < a, b$

$h^1(1-h)^2 \rightarrow$ Normal point pinning $d > a, b, c$

Here *a, b, c,* denote the dimensions of the pin and *d* is for fluxoid spacing. Normal point and surface pinning can also be characterized in terms of h_{max} values, which are generally 0.33 and 0.2, respectively[4]. Qin *et al.* proposed another pinning mechanism based on the vortices and pinning centers[86]. Based on this pinning mechanism, δT_c pinning (pinning via the spatial fluctuations in the transition temperature) is evident in MgB_2, whereas δl (pinning via the

spatial fluctuations of the charge-carrier mean free path) pinning is not observed[86].

A definitive argument excluding effects on the pinning mechanism is given by the normalized pinning force $F_{\mathrm{p}}(h)/F_{\mathrm{p}}(h_{max})$ obtained by magnetization. The normal pinning functions together with pinning force data was reported by Collins *et al.*[4] for a SiC-doped MgB_2 sample (see **Figure 2.15**), in which the normalizing field, H_{irr}, was based on a 100 Acm^{-2} criterion. A pronounced departure from scaling was observed in the results. The generally expected characteristic of grain-boundary pinning was seen for temperatures range between 10 K and 20 K, while in the 20–30 K range it was revealed that point pinning was starting to dominate[4]. The lack of fit for both curves at higher reduced fields was attributed to a distribution of H_{irr} value resulting from sample inhomogeneity.

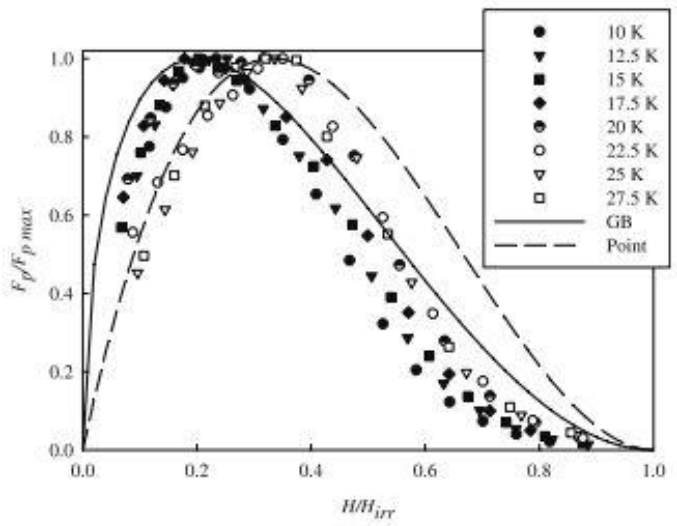

Figure 2.15 Normalized bulk pinning force curves for a sample of an MgB_2 strand doped with 5% SiC (particle size 30 nm)[4]

Motaman *et al.* found in the malic acid doped wire that the crossover field B_{sb} is almost the same even at different reaction temperatures[87]. Conversely, the crossover field B_{th}, reflecting the thermal regime, is dependent on the sintering temperature (see **Figure 2.16**).

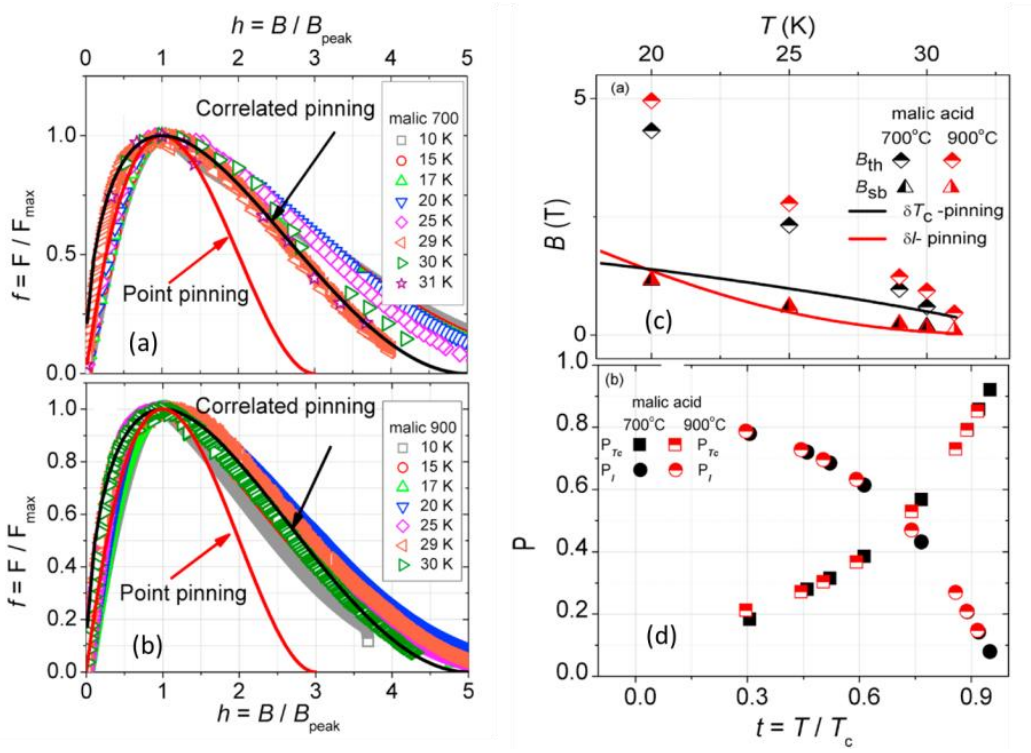

Figure 2. 16 (a) and (b) Magnetic field dependence in the temperature range of 10–30 K of the reduced pinning force *f*(*h*) for the malic acid treated MgB_2 wire sintered at 700 and 900 ° C. In (c) and (d) B_{sb} and B_{th} crossover field temperature dependence for the malic acid treated samples sintered at 700 and 900 ° C, with the black and red fitted lines standing for the δT_c and $\delta \ell$ pinning mechanisms, respectively[87].

Griessen *et al* proposed that, of δT_c and δl pinning results in different temperature dependences of the critical current density J_{sv} in the single-vortex pinning regime [88]. The relation between the J_{sv} and normalized temperature:

For δT_c pinning: $$J_{sv} \propto (1-t^2)^{7/6}/(1+t^2)^{5/6}$$

For δl pinning: $$J_{sv} \propto (1-t^2)^{5/2}/(1+t^2)^{-1/2}$$

Blatter *et al.* showed that, J_c is field independent if the applied field is less than the crossover field B_{sb} at which the dominant pinning mechanism changes from single-vortex to small bundle pinning[89]. In the area belowB_{sb}, vortex lattice is controlled by single-vortex pinning mechanism. Qin *et al.*[86] expressed the temperature dependency of the cross over field,

$B_{sb}(T) = B_{sb}(0)[(1-t^2)/(1+t^2)]^{v}$. For δT_c and δl pinning, v = 2/3 and 2, respectively.

2.10 Effects of doping on the superconductivity of MgB_2

To improve the J_c of MgB_2 many techniques have been introduced so far throughout the last decade such as chemical doping, thermo-mechanical processing, ball milling, and proton irradiation. Among those techniques chemical doping is found as the most effective and easy way of improving the superconducting performance of MgB_2. Depending on the way of introducing dopant materials in the MgB_2 structure, it can be divided into two categories: (1) substitution method and, (2) addition method. In case of substitution method, dopant is substitute into the B or the Mg crystal sites, which results in impurity scattering of charge carriers and responsible for changes in the crystallinity, electronic state, and lattice distortions. Contrarily, addition effects act between the grains, producing a significant effect on the grain connectivity and grain growth. It has an important role in grain boundary flux pinning[90]. Although, chemical doping enhances superconducting properties of MgB_2, it has adverse effect on T_c. Many dopants have been tried on MgB_2 throughout the last decade, such as, metallic elements (Ti, Co, Ni, Cu, Zr, Mo, Fe, Ag, Al, Si, La), metal oxides (TiO_2, SiO_2, Pr_6O_{11}, Al_2O_3,Dy_2O_3, HoO_2), carbon and carbon inorganics (nano-C, CNT, nano diamond, Na_2CO_3, TiC, SiC, B_4C), borides(CaB_6, ZrB_2,TiB_2, NbB_2), silicides (WSi_2, $ZrSi_2$), nitrides(Si_3N_4), and organic compounds (malic acid, paraffin, carbohydrate, maleic anhydride, toluene, acetone, ethanol, and tartaric acid)[4]. In this thesis, effect carbon doing is studied as it is the most effective dopant. It enhances the high field J_c significantly.

2.11 Effect of carbon (C) doping on the superconductivity of MgB_2

The metal oxides and metallic elements were introduced into the MgB_2 structure to create the normal flux pinning centers, however, nitrides, borides, and carbon containing dopants are more effective due to increase of H_{c2} by introducing pinning centers as well as substituting

boron in MgB_2[90]. Successful doping can be resulted by following improvements: (a) increment of H_{c2} and H_{irr} due to more impurity scattering, (b) wider distribution of point pinning centers, (c) by generating localized lattice strains[4]. So far, extensive research on carbon doping shows improvement of superconducting properties in MgB_2.

In the early stages, main focus was on the effects of doping on superconductivity, primarily on solubility and two-band studies[30, 91, 92]. Later to overcome the diffusion problem B_4C was used as a starting material[58, 93]. Due to differences in the starting materials, variation in the reported results on carbon solubility and the doping effect can be seen and amount of carbon substitution into MgB_2 by solid–vapor reaction route is in disagreement with the nominal composition[94]. Avdeev *et al.* also reported the changes in lattice parameters with the increasing carbon concentration and proposed an empirical model to estimate the carbon content. In his model, he estimated the level of carbon substitution, x in $Mg(B_{1-x}C_x)_2$, as x = 7.5Δ (*c/a*), where Δ (*c/a*) denotes the change in *c/a* compared to a pure sample[95]. In single crystal MgB_2, Kazakov *et al.* studied the structural, magnetization behavior of carbon substituted sample, and transport properties[96]. In the investigation of whole substitution range, T_c decreases linearly with increasing carbon content (see **Figure 2.17**) and it ranges from 10 K to 39 K.

Due to huge impact of carbon on MgB_2, wide ranges of carbon source have been investigated by different groups. The common carbon source so far reported for MgB_2 are SiC[98-100], carbon nano tubes (CNTs)[101-103], boron carbide (B_4C)[104-106], hydrocarbons[107-111], graphite[112], nano diamond[113], carbohydrates[114, 115], and graphene[116-120].

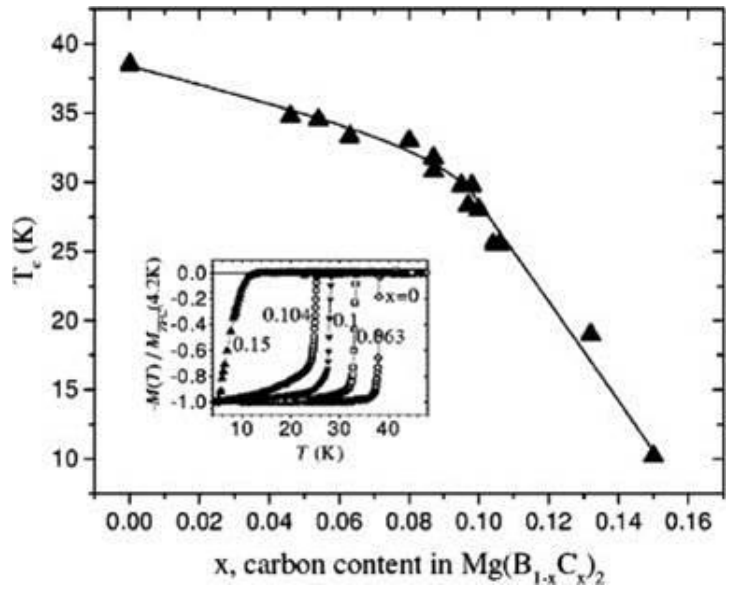

Figure 2.17 Variation of T_c as a function of carbon concentration. Inset shows magnetization curves of Mg ($B_{1-x}C_x$) crystals with different carbon content[96].

Soltanian *et al.* first investigated the effect of carbon on J_c and H_{irr} in MgB_2 and they found both T_c and *a*-axis lattice parameter decrease monotonically with increasing carbon content (see **Figure 2.18**)[97].

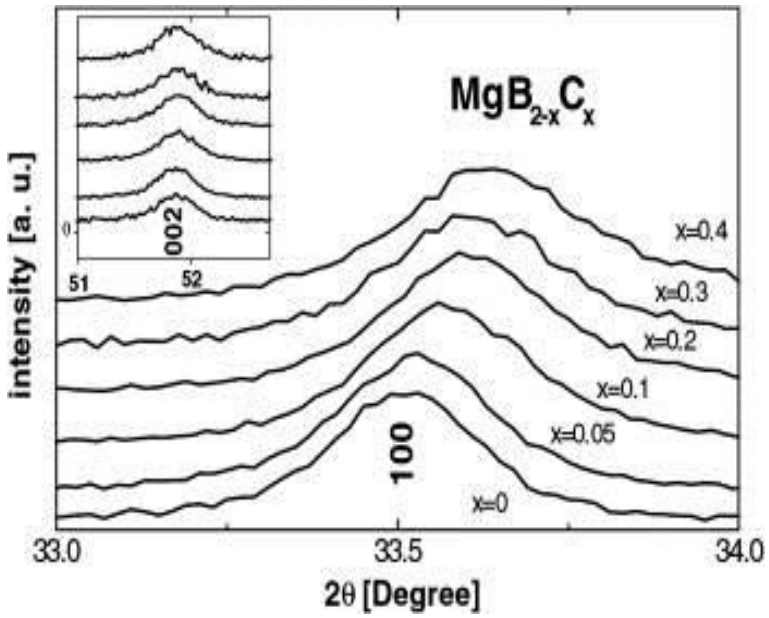

Figure 2.18 The (1 0 0) and (0 0 2) (inset) Bragg reflections for the Mg $(B_{1-x}C_x)_2$ composition with x = 0, 0.05, 0.1, 0.2, 0.3, and 0.4. The results showed that carbon substitution only has an effect on the *a*-axis lattice parameter [97].

Disparate studies on SiC doped MgB_2 have been done to optimize the performance for practical application and extensive work was done to investigate the effect of sintering conditions, different fabrication techniques, precursor size and optimum doping levels[99, 121-126]. At 4.2 K, significant enhancement was reported by Susner *et al.* using the SiC and 15% excess Mg, yielded 10^5 Acm^{-2} at 6 T and 10^4 Acm^{-2} at 11.5 T[127] in wires. In bulk sample with 10 wt% SiC doping Dou *et al.* reported J_c of 10^5 Acm^{-2} at 3 T and H_{irr} value of 8 T at 20 K[128]. UOW group showed that carbon substitution for B resulted in a large number of dispersed nanosize impurities and intra-granular dislocations, which are primarily responsible for the substantial enhancement in flux pinning[128,129]. Later, significantly high value of H_{c2}(exceeding 40 T) was reported by Matsumoto *et al.* in 10% SiC-doped MgB_2 bulk, sintered at 600 ºC[130]. Different leading research groups all around the world confirmed the potential of SiC as the most effective dopant for improving the transport current of MgB_2 conductor, such as the Los Alamos National Laboratory (US), Ohio State University (US), the National Institute for Materials Science, NIMS (Japan), Hyper Tech Research Center (US), the University of Tokyo (Japan), Karlsruhe Institute of Technology, KIT (Germany) the University of Wollongong, UoW (Australia) and the University of Geneva (Switzerland). In **Figure 2.19,** a comparison of transport J_c of SiC-doped MgB_2 wires with the best un-doped MgB_2 wire from various groups at 4.2/5 K has been depicted.

Due to the improved reactivity of nano carbon, less heat treatment temperature is required in nano carbon doped MgB_2 for considerable substitution of carbon in boron sites. Ma *et al.*[136], reported significant enhancement of superconducting properties for nano-carbon doped MgB_2 tapes at 750 ˚C. The transport J_c for the 5 at. % doped tapes attained $1.85\times10^4 Acm^{-2}$ at 10T and $2.8\times10^3 cm^{-2}$ at 14T, respectively. Moreover, the T_c for the doped tapes degraded slightly[136].

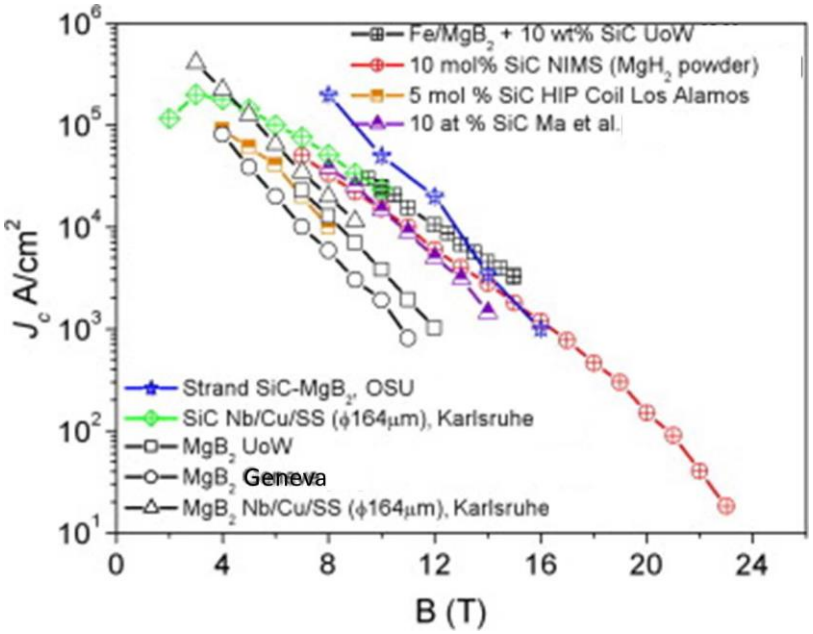

Figure 2.19 Comparison of transport J_c of SiC-doped MgB_2 wires with the best un-doped MgB_2 wire from various groups (Geneva[104], NIMS[131], Karlsruhe[132], OSU[133], UoW[128], Los Alamos[134] and Ma *et al.*[135]) at 4.2/5 K[90].

Among the different carbon containing dopants CNTs improve the mechanical and thermal properties of MgB_2. The best performances in J_c was reported by Yeoh *et al.* in the single wall carbon nano-tubes (SWCNT) doped samples sintered at 900˚C [90] . There are some problems associated with the CNTs due to entangle and agglomeration, which results inhomogeneity in the mixture and block the current transport and leads to suppressing the J_c[103]. Later, ultra-sonication was introduced to improve the homogeneity of CNTs doped MgB_2 matrix, which resulted further enhancement[102].

Most of the nano-dopants reported so far were introduced through the solid state reaction. Therefore, homogeneous distribution of carbon cannot be attained, which have important consequences on superconducting properties. To confront this problem hydrocarbon and carbohydrate doping were used as highly reactive and fresh carbon source, which have advantages over solid state reaction method, resulting in comparable *J*c values with those from the nano-SiC doping[137, 138]. Moreover, the low field J_c of the conductor does not decrease up to

a certain doping level in this method. From the microstructural analysis it is evident that the lower decomposition temperatures of hydrocarbons and carbohydrates produce highly fresh and reactive carbon and ensure more homogeneous mixing in the liquid state[108]. Finally, at low sintering temperature smaller grain size of MgB_2 with carbon doping leads to high J_c. In **Figure 2.20,** a Comparison of J_c–B characteristic at 4.2 K of malic acid treated wire with those of other commercial MgB_2 wires fabricated by Hyper Tech Research Inc. are depicted. The problem associated with the chemical solution route is that carbon concentration cannot be maintained properly in this complicated process.

For enhancing the high field performance using carbon doping has been established by different research groups. For homogenous carbon doping, the most interesting technique so far reported is using B_4C as a starting material. For bulk sample Ueda *et al.* and Yamamoto *et al.* reported that carbon can substitute in boron sites at 850 °C[105, 140, 141]. Lezza *et al.* investigated the effect of B_4C in MgB_2 wires and reported the J_c value of 10 wt% B_4C doped MgB_2/Fe wires is 10^4 Acm^{-2} at 4.2 K and 9 T[104].

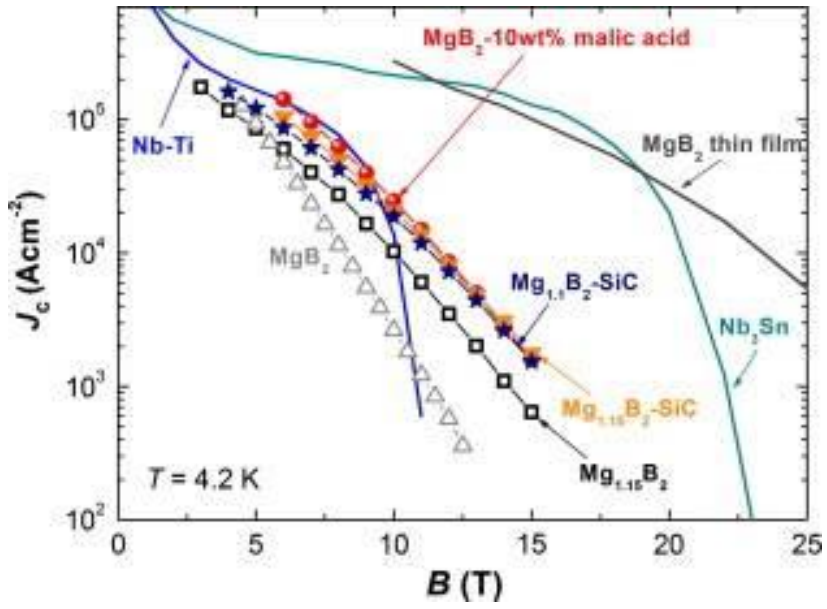

Figure 2. 20 Comparison of J_c vs. B characteristics at 4.2 K of malic acid treated wire with those of other commercial MgB_2 wires fabricated by Hyper Tech Research Inc. The malic acid

treated MgB_2 wire was sintered at 600 °C for 4 h. The J_c was about 25,300 Acm^{-2} at 4.2 K and 10 T[139].

2.12 Pressure Effects on J_c of MgB_2 Wires

To date, the low density within the filament cores has been a serious obstacle in reaching high J_c values for MgB_2 wires fabricated by the *in situ* processed technique. In addition, the reaction of magnesium and boron to form MgB_2 involves a volume contraction that produces a final density limited to about 50 % of theoretical density (2.36 g/cm^3). The high porosity is well known to be difficult to avoid. As a result the grain connectivity is hampered by the presence of voids in the finished wires. The typical effective superconductor area in the wire is only about 10%[142]. Collings *et al.*[4] reported relative mass densities of 70 to ~80% for MgB_2 filaments in *ex situ* wires, while Pan *et al.*[143] found ~45% for wires produced by the *in situ* technique. Several attempts have been undertaken to enhance the mass density of *in situ* filaments by applying high pressure during the reaction heat treatment. Serquis *et al.*[144] performed the reaction under hot isostatic pressure (HIP) conditions at 0.2 GPa in both *in-situ* and *ex-situ* wires and reported at 4.2 K an enhancement of $B(10^4)$ up to 1 T where $B(10^4)$ is the field at which critical current density (J_c) reaches a value of 1 x 10^4 A/cm^2. Prikhna *et al.* reported very dense bulk samples of Ti alloyed MgB_2 after reaction at T > 1000 °C in a multi-anvil device under 2 GPa argon (Ar) pressures[145]. In the bulk samples, the mass density was enhanced to values close to 100 %, yielding B (10^4) = 11 T at 4.2K. Yamada *et al.* reported hot pressing on SiC alloyed *in situ* tapes at 630°C under 100 MPa[146]. In the hot pressed tapes, the enhancement of Jc was significantly higher, the extrapolated value of B $(10^4)^{//}$ being close to 14T. The large difference in J_c between the hot pressed bulk samples [5] and the hot pressed tapes is at least partly due to the fact that the deformation of tapes by rolling leads to a certain degree of texturing[146]. Texturing is an inherent feature of MgB_2 wires and tapes produced by multistep deformation. Kim *et al.* reported the large anisotropy ratio in hot pressed binary and malic doped MgB_2 tapes[147]. Very high J_c values of MgB_2 wires were obtained by the *infiltration*

method, originally proposed by Giunchi *et al.*[148], recently Hur *et al.*[149] and Togano *et al.*[150] improved the method. They are thought to be essentially correlated to a high mass density of the superconducting hollow filaments characterizing this technique. Cold densification was also applied as an alternative to the application of pressures at high temperature, but was so far not used for *in situ* wires. Matsushita *et al* analyzed the changes of J_c and resistivity $\rho^{40\,K}$ on *in situ* MgB_2 pellets[151]. In *ex situ* MgB_2, Pachla *et al.*[152] reported the effect of cold isostatic pressure up to 1.5 GPa. Combination of Hydrostatic extrusion and two axial rolling for core densification was reported by several groups[126, 153, 154]. But, still it is not suitable for commercial application due to insufficient filament uniformity and improper design of billet composition.

In 2009, cold high pressure densification has been suggested as an alternative to enhance mass density after cold high pressure deformation (CHPD)[110, 155]. The J_c has been reported by Hossain *et al.*, around ~40,000 Acm^{-2} at 4.2 K and 10 T for a malic acid doped square conductor by CHPD[110]. The first successful CHPD of a dense MgB_2 conductor in a short-length (< 1 m) was reported by the University of Geneva in 2008. The density increased from 50% for normal wire to 73% for the CHPD wire after heat treatment. The J_c was increased by more than 300%, particularly at 20 K temperature[155]. This CHPD has been successfully applied on *in-situ*, *ex-situ* mono and multi filament wires with significant enhancement of J_c. Subsequent pressing steps with overlapping pressure zones have been performed by Flukiger *et al*. up to a wire length of 1 meter without degradation with respect to short wire lengths[156]. This result is promising in view of the magnet application of the CHPD process to wires of several hundred meters length.

2.13 Advantages of CHPD over other pressure techniques

As large quantities of MgB_2 wire are necessary for industrial applications, any high temperature/high pressure processing steps are not desirable, not only from an economical

point of view but also because they would limit the subsequent deformability of the wire. It is clear that the high pressure steps should be applied at low temperature, preferably at room temperature, thus allowing winding and cabling before the reaction heat treatment.

This may be illustrated by a brief comparison. The high gas pressure (up to ~1 GPa) in Cold Isostatic Pressing devices[152] has the disadvantage to be limited to small sample volumes, the size of the device being restricted by safety requirements. In Hot Pressing devices[145], where the pressure is transmitted by solid anvils, the total sample volume is limited to several cm^3, i.e. too small for industrial wire lengths. Finally, Hot Isostatic Pressing or HIP machines would be large enough for reacting kilometers of MgB_2 wire at argon pressures up to 0.2 GPa. However, the wire cannot longer be wound after HIP processing. The HIP treatment of complete coils is not an alternative, due to the shrinkage of the filaments during reaction, which would lead to instabilities.

A room temperature processing technique was developed at GAP in Geneva in 2008, namely the Cold High Pressure Densification (CHPD)[110, 155]. This method is based on a prototype cell, designed for the application of high pressures at room temperature, with solid anvils acting simultaneously on all four sides of a square wire. This densification step is followed by a pressure release allowing a recovery of the wire without damage. The operation of the initial device (particularly the pressure release) is very time consuming, but it was very useful for deciding whether it was appropriate to develop an automatic device[156] for continuous CHPD processing of long wires. Hossain *et al*. found that the densification step has the effect of enhancing the mass density of the unreacted (Mg + B) filament, letting the degree of texturing unchanged[110]. This is in contrast to the effect of pressing of a tape between two walls, the tape flows in the direction parallel to the pressing walls, with the consequence that the degree of texturing is enhanced, the mass density changing only slightly.

After CHPD on short samples the mass density of binary MgB_2 monofilaments was enhanced from 0.44% to 0.54% of the theoretical mass density after applying 2.5 GPa[155]. At the same time, a remarkable decrease of electrical resistance was observed on densified wires, reflecting an improved connectivity. It should be noted that the pressures applied on the 4-wall cell reached a maximum value of 6.5 GPa. At this pressure, the mass density of the unreacted (Mg + B) powder mixture reached 96 %, while the corresponding value in the reacted MgB_2 filament increased up to ~73% of the theoretical value. However, a reproducible enhancement of J_c was only observed up to pressures of the order of ~3 GPa. Later in this Chapter, the overall progress of MgB_2 wires by cold high pressure densification is compared with other reported densification techniques by various groups.

2.14 Effect of CHPD on MgB_2 conductor

2.14.1 CHPD applied on *in-situ* monofilament wires

The effect of CHPD on the superconducting properties of monofilamentary MgB_2 wires doped with 10 wt % $C_4H_6O_5$ (malic acid) is depicted in **Figure 2.21[110].** It was found that the enhancement of J_c in malic doped wires is considerably larger than for the densified binary MgB_2 wires (see **Figure 2.21**). By optimizing the CHPD process in the pressure range above 2 GPa further enhancement is expected. At 1.48 GPa pressure, the value of $B(10^4)^{//}$ was enhanced from 11.3 to 13.2 T. The J_c values of the present wires at 8 T and 4.2 K are now approaching those of industrial NbTi wires (1.2×10^5 Acm^{-2}). The Li *et al*. recently reported the best J_c value for the pre-carbon doped second generation MgB_2 wire is 10^5 Acm^{-2} at 10 T by Advanced Internal Mg Infiltration (AIMI) process[157]. The result is exceeding those commercial Nb-Ti wires and satisfactory to all technical applications. However, there is a serious limitation in mechanical properties and for scaling-up the AIMI method. In this process the Mg infiltration into the B layer forms a hollow wire with only a thin layer of MgB_2 in the

interior of the sheath tube, which may cause reduced superconducting volume and poor mechanical properties for the magnet coil development.

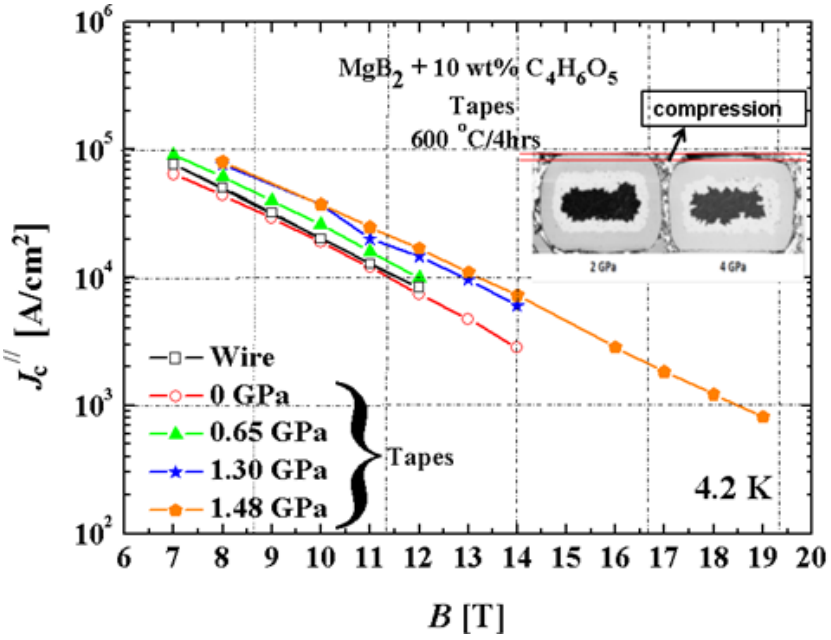

Figure 2.21 J_c vs. B at 4.2 K for $C_4H_6O_5$ doped MgB_2 tapes (Monel sheath, Nb barrier) after cold densification at various pressures. The values of the original round wire are also shown (600°C/4h) (in the inset, cross section of mono filament wire after CHPD)[110].

2.14.2 CHPD applied on *in-situ* multifilament wires

After successful application of CHPD to monofilamentary wire, it was applied to multifilamentary MgB_2 wires and to longer wire lengths by the same group[158]. A substantial enhancement of the transport J_c was observed in the binary 18-filament wires by sequential densification with overlapping pressure regions (see **Figure 2.22**). The field $B(10^4)^{//}$ where the transport J_c at 4.2 K reaches the value of $1x10^4$ $Acm^{-2}$for parallel field direction was obtained 8.5 T (0.1 μV/cm criterion). The enhancement of J_c by a factor 2.3 at 4.2K at applied fields up to 10 T observed in densified samples is directly correlated to the increasing mass density due to the filament volume contraction[158]. Recently Ye *et al*. reported transport J_c for SiC-added 37-filament IMD-processed MgB_2 wires, which achieved a value of 7.6×10^4 Acm^{-2}at 4.2 K and 10 T, which is higher than any kind of multi-filament wires with a smaller number of filaments[159]. The current carrying performance of those IMD wires is sufficient for the large

scale applications, but the problem is associated with the mechanical performance and durability due to the presence of hole inside the wire.

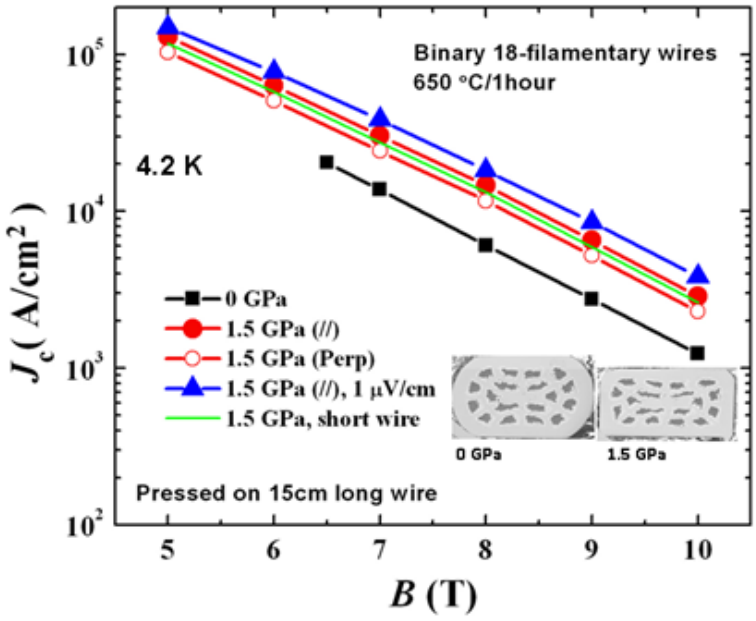

Figure 2.22 J_c vs. B at 4.2 K for binary 18-filament MgB_2 wires, at p = 0 and after CHPD at 1.5 GPa. The $B(10^4)$ values are 8.48 and 8.18 T for parallel and perpendicular field orientation with respect to the wider surface (0.1 μVcm^{-1} criteria) and inset shows the cross section of multi filament wire before and after CHPD [158].

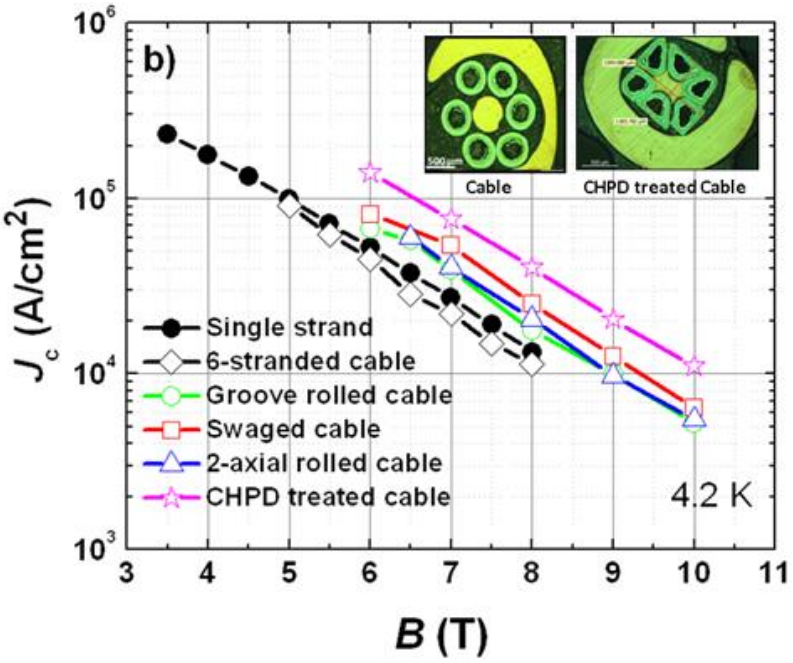

Figure 2.23 Critical current density, J_c vs. B, of single monofilament wire and cables with and without additional mechanical deformations at 4.2 K. Inset shows the cross section of cable before and after CHPD[160].

2.14.3 CHPD applied on *in-situ* cables

After the successful application of CHPD on mono- and multi-filament wires, it was applied on MgB_2 cables to improve the critical currents[160]. Hossain *et al.* studied the cable performance, which was produced by *in-situ* MgB_2 wire and found the superior current carrying capability after CHPD. In **Figure 2.23**, a comparison is depicted among the various mechanically deformed cable and mono filament wire[160]. The highest critical current density (10^4 Acm^{-2} at 10 T) is found in the cable deformed by CHPD due to higher filament mass density compared to the cables deformed by swaging, groove rolling and two-axial rolling.

2.14.4 CHPD applied on *ex-situ* wires

Kulich *et al.* investigated the effect of CHPD on *ex-situ* wires[161] and reported that *ex-situ* wires up to 2 GPa show only a negligible enhancement of the MgB_2 mass density and transport J_c, while a considerable enhancement of J_c was reported for *in-situ* wires with the same applied pressure. In both cases, CHPD enhance the grain connectivity, however in *ex-situ* wires, the enhancement of J_c is related to the partial disruption of the oxide layer around each MgB_2 powder particle. On the other hand, the enhancement of J_c *in-situ* wires is related to void reduction and increased connectivity due to larger contact area between grains. In *ex-situ* wire, the performance degradation after prolong exposition to air before heat treatment is major problem. After several months, the J_c value can be less than half of the original value and also effects negatively on T_c[162]. This problem can be eliminated by using CHPD. After CHPD electrical resistivity of the *ex-situ* wire gets reduced (see **Figure 2.24**), which establish the improvement of grain connectivity due to the breakage of the oxide layers[161].

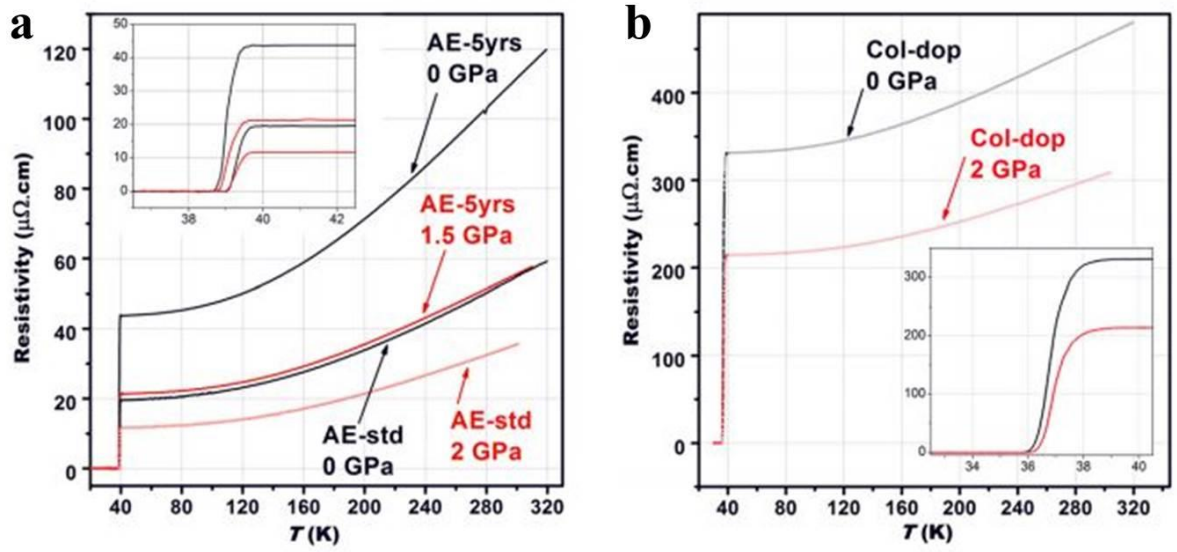

Figure 2.24 a) Temperature dependence of resistivity for various *ex-situ* MgB_2 wires. The inset shows details of the transition. Here, AE-std and AE-5yrs denote standard *ex-situ* wire and 5 years old standard *ex-situ* wire, respectively. **b)** Temperature dependence of resistivity for the *ex-situ* MgB_2 core Col-doped sample (commercial *ex-situ*, doped with 5 wt% of carbon). The inset shows details of the transition[161].

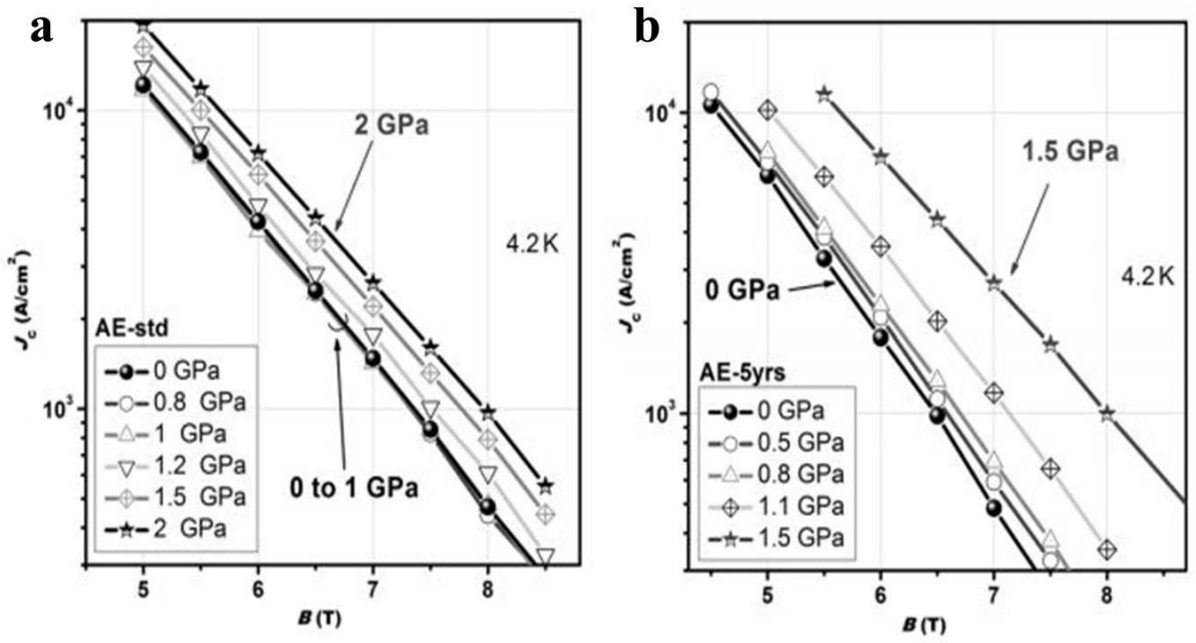

Figure 2.25 Enhancement of J_c by CHPD for **(a)** the standard commercial ex situ wire and **(b)** 5 years old standard ex situ wire[161].

The transport J_c of standard commercial *ex-situ* wire is enhanced after CHPD (see **Figure 2.25**).

Kulich *et al.* reported that after cold pressing, the J_c of the same wire exceeds the original

values, even after exposing the unreacted wire for more than one year to air[161].

2.14.5 Effect of CHPD on density:

The improvement of transport Jc in CHPD treated wires is due the enhancement of filament mass density[155]. Flukiger et al. showed that the relative mass density inside the unreacted (Mg + B) filaments was improved to 96% with 6.5 GPa applied pressure before the final heat treatment, corresponding to an enhancement of the relative mass density of the reacted MgB_2 filaments from 43 up to 73% (see **Figure 2.26(a)**). The enhancement rate of J_c as a function of mass density is the same, regardless whether the initial shape of the wires was round or rectangular (see **Figure 2.26(b)**)[155]. The effect of density is also evident in multifilament and cable conductor which has been shown in **Figure 2.22** and **Figure 2.23**, respectively.

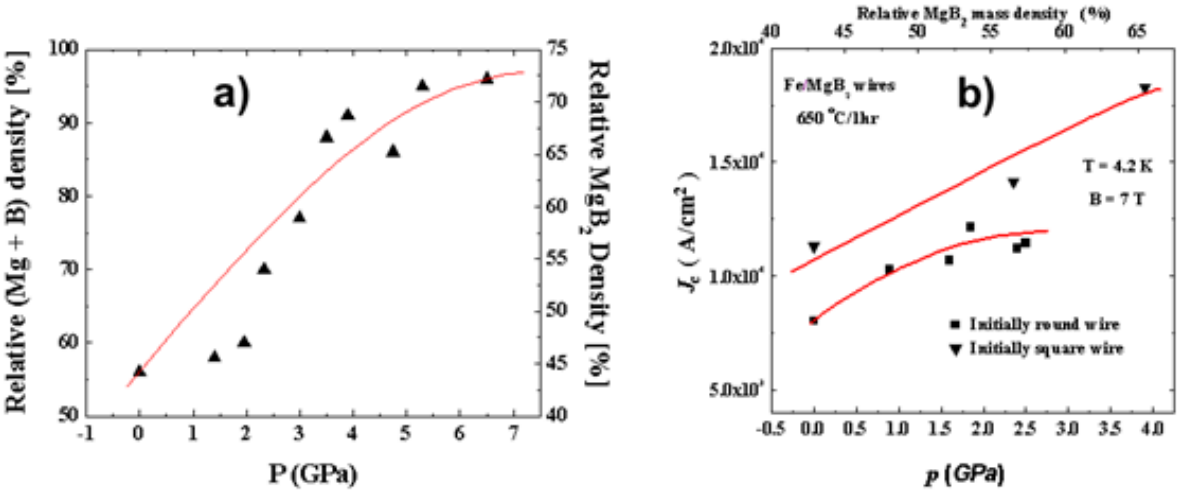

Figure 2.26 a) Mass densities of filaments in Fe/MgB_2 wires. Left scale: relative density d_m of the unreacted (Mg + B) mixture. Right scale: relative mass density d_f of reacted MgB_2 filaments. **b)** Variation of J_c of a binary Fe/MgB_2 wire at 4.2 K and 7 T, as a function of the cold densification pressure. Initially round wires show a maximum of J_c at 1.8 GPa, while initially rectangular wires still show an enhancement up to 4 GPa. The upper scale represents the relative mass density d_f of MgB_2 filaments[155].

2.14.6 Effect of CHPD on Microstructures

The inset of the **Figure 2.21, 2.22, 2.23,** cross section of a mono-, multifilament wires and cables have been shown, respectively before and after applying the CHPD simultaneously on the four surfaces. The transition zone between the unpressed region and the pressed region has

been depicted in **Figure 2.27(a)**, heat treated at 650 ◦C for 1 h. The microstructure of conventionally treated MgB_2 filaments shows always a certain amount of voids, as a consequence of the volume shrinking during the reaction process. The voids are clearly visible in **Figure 2.27(b)** on a polished surface. A considerable amount of voids were reduced after densification, as illustrated by **Figure 2.27(b)** after densification at a pressure of 1.9 GPa.

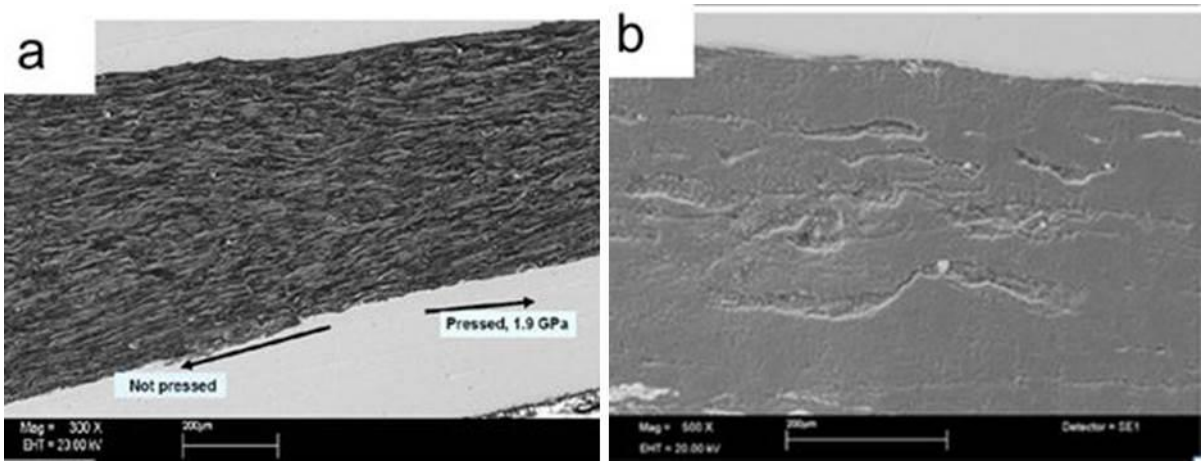

Figure 2.27 a) Filament of a binary Fe/MgB_2 wire at the border of a region pressed at 1.9 GPa. b) High resolution scanning electron microscopy (SEM) investigations revealed the reduced porosity[110, 158].

In doped wires, CHPD makes the carbon substitution more effective, leading to a reduction of T_c and hence reduction of anisotropy due to poor texturing. The observed improvement of J_c after applying CHPD in malic doped wires was due to the reduction of voids (SEM) and additional defects in the lattice[110].

2.14.7 Effect of CHPD on the exponential *n*-factor

Power law relationship is used for modeling and calculating the nonlinear transition of a superconductor. From the application point of view, such as MRI and medium filed NMR, the behavior of the exponential *n* factor plays a critical role[163]. Flukiger *et al.*[163, 164] and Hossain *et al.*[158] reported the enhancement of *n*-value for both mono filament and binary 18-filamnet wire. **Figure 2.28** shows the field dependency of the exponential *n* factor for both mono filament and multifilament wire. From the reported results of *n*-value, it is now evident that at 4.2 K and

low fields it can be very high for MgB_2 wires[163].

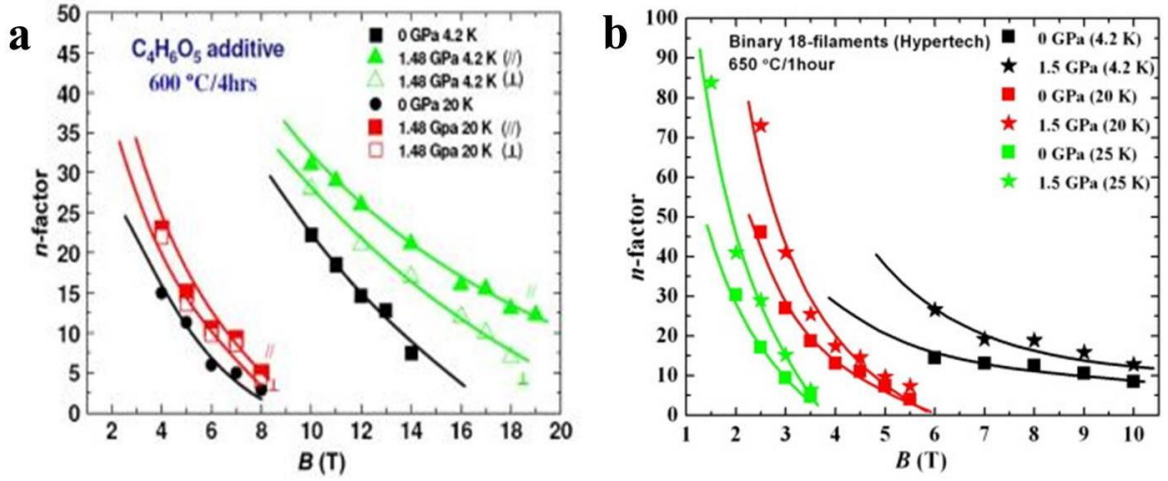

Figure 2.28 Variation of the exponential *n*-factor as a function of applied field, at 4.2, 20 and 25 K for a) mono filament alloyed[164] and **b)** binary multifilament wires[163].

But, with the applied field it decreases drastically, which can be limiting factor for applications at higher fields. CHPD treated wires exhibits higher *n*-value in both mono (see **Figure 2.28(a)**) and multi filamentary wires (see **Figure 2.28(b)**). 50 % improvement of *n*-value has been reported after densification at 1.5 GPa. From application perspective *n*-value should not be less than 30 and after densification, the average increase estimated around 1 T at 20 K and 2 T at 4.2 K[164] in malic acid doped mono filamentary wire. Although *n*-value is an empirical factor which depends on a variety of effects which are not all well-defined, it reflects in a certain way the homogeneity of a filament. Therefore, the enhancement of *n*-value can be interpreted as an improved homogeneity of the densified filament. Recently Hossain *et al.* also showed the similar effect in case of binary *in-situ* cable[160].

2.14.8 Effect of CHPD on anisotropy

Kovac *et al*. reported that anisotropy is affected by the mechanical strength of the metallic sheath and the metal matrix interface roughness, which affects the texture of Mg[165]. In the in-situ fabrication method texture is introduced by deformation of the crystal structure of the Mg[165]. Flukiger *et al.* reported the effect of CHPD on anisotropy factor of the malic doped wire

at 4.2K. In **Figure 2.29**, the anisotropy factor is plotted against the applied field and from the figure it is evident that anisotropy decreases with applied magnetic field[163]. Häßler *et al.* also found a decrease of anisotropy with increasing carbon content in the tapes[166]. Hence, CHPD method has an influence facilitates the reaction process and leads to enhanced carbon values[163].

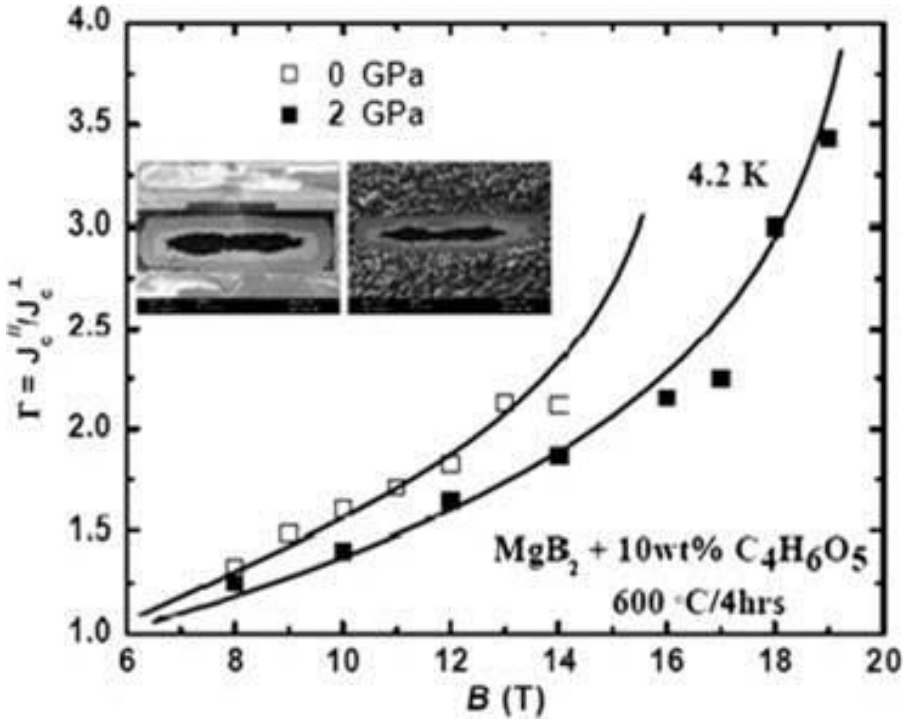

Figure 2.29 Variation of the anisotropy ratio $\boldsymbol{\Gamma = J_c^{\parallel}/J_c^{\perp}}$ vs. B/B_{irr} for $C_4H_6O_5$ added tape with additive at 4.2 K after CHPD at p = 2 GPa. The lines are a guide for the eye. Inset: shape of the tape with and without pressure[163].

2.14.9 Effect of CHPD on AC loss, intra-wire resistance and strain dependence of critical current

Zhou *et al.* reported the effect of CHPD on the intra-wire resistance, AC loss, and strain dependence of the critical current for the first time[167]. Increased critical current and AC loss, and a reduced intrawire resistance, are found after CHPD. From the investigation, it was evident that the densified MgB_2 wires is less strain sensitive and has a higher irreversible strain limit due to the superior connectivity and percolation of MgB_2 filaments[167].

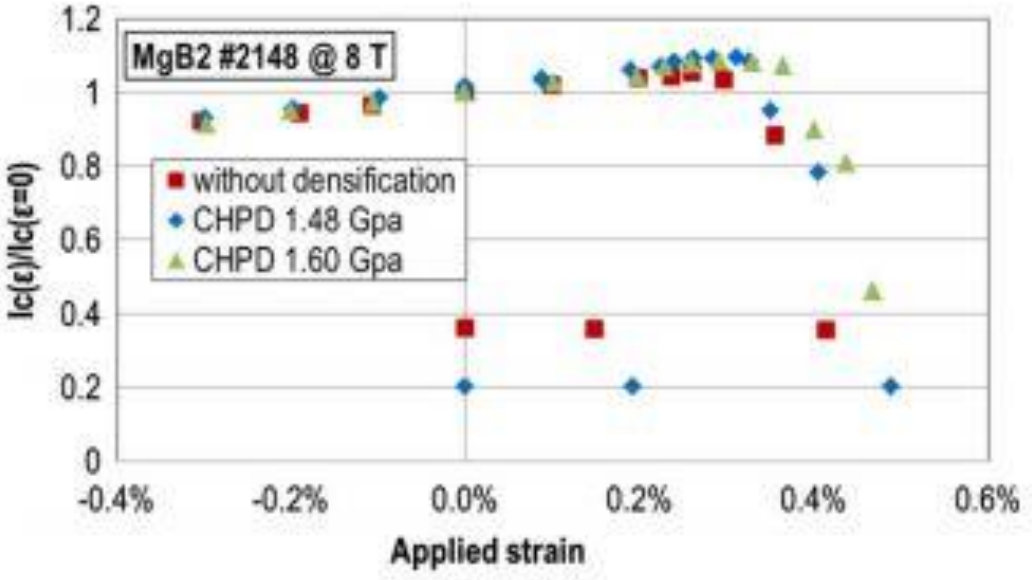

Figure 2.30 The normalized I_c as a function of axial strain at 4.2 K[167].

In **Figure 2.30**, normalized transport I_c is plotted against the axial strain and from the figure it can be seen that irreversible strain is around 0.28%, 0.31%, and 0.33% in the cases without CHPD, CHPD at 1.48 GPa, and 1.60 GPa, respectively[167]. Better performance can be seen with the densified wires in the high tensile strain region (above 0.3%), than those without densification.

2.14.10 Effect of CHPD on T_c distribution (specific heat measurement)

Senatore e*t al*. reported the effect of CHPD on the T_c distribution at zero magnetic field[168]. From the calorimetric investigation is clear that CHPD does not influence the width of the distribution (see **Figure 2.31**), but onset T_c is reduced of about 1 K (see **Figure 2.31(b)**). the reason behind this can be the substitution of more carbon into the boron sites during the CHPD process, which is supported by the reduction of *a*-axis lattice parameter[163,168]. The conventional way of improving the carbon substitution is increasing the heat treatment temperature or longer heat treatment time. In both cases, higher carbon content is accompanied by larger grain sizes, which reduce the grain boundary density. Senatore *et al.* showed that higher carbon content

can be achieved at low temperature using CHPD through reduced reaction path in malic doped wire at 600°C/4h.

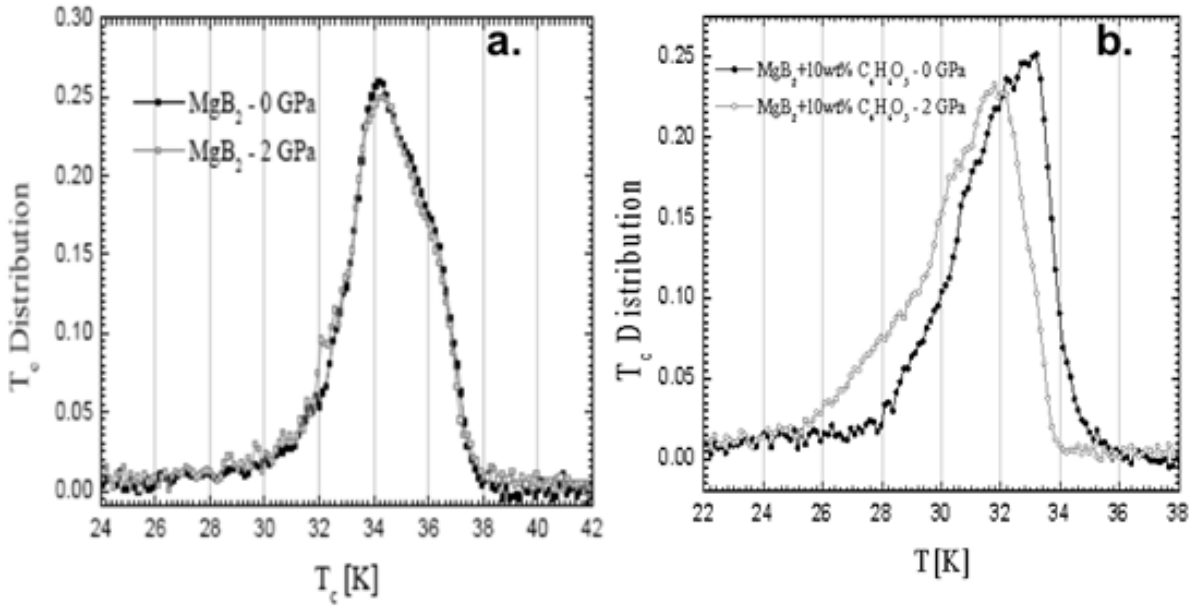

Figure 2.31 a) Distribution of T_c obtained by the deconvolution of the calorimetric data for the non-densified binary MgB_2 sample (solid symbols) and for the binary MgB_2 sample after densification at p = 2 GPa (open symbols). It is seen that the T_c distribution is not influenced by CHPD in the case of binary MgB_2 b) Distribution of T_c for the malic doped samples, non-densified (solid symbols) and densified at p = 2 GPa (open symbols). CHPD determines a higher substitution rate of carbon, resulting in a reduced onset T_c and a broader T_c distribution[168].

2.15 Recent progresses of MgB_2 superconductor and how to improve further?

The progress achieved in the field of MgB_2 conductors in the last 10 years is very impressive, as well from the theoretical as from the experimental point of view. In 2008, a new kind of treatment was introduced at GAP in Geneva, the Cold High Pressure Densification or CHPD technique[110, 155]. The relative mass density inside MgB_2 filaments of *in-situ* mono and multifilament wires was enhanced from 48% to > 60 % for pressures well above 1 GPa, thus leading to strongly enhanced values of J_c. The J_c at 4.2 K and 8 T has been reported to be increased to ~100,000 A·cm^{-2} for a malic acid doped square conductor by CHPD. The best J_c so far reported for the AIMI second generation MgB_2 wire was 100,000 A·cm-2 at 9.5 T[157], well exceeding those commercial Nb-Ti wires and satisfactory to all technical applications.

However, there is a serious limitation for scaling-up the IMD method in terms of filling factor, mechanical strength and reliability. In this thesis, an innovative method has been proposed for the production of high performance and economic MgB_2 wires by the second stage densification technique to get the similar performance but avoiding the possible issues faced by the second generation wires. Multifilament and multi-strand conductors with kA class current capacity and higher *n*-factors are the key requirements for many large-scale applications. Nevertheless, it is expected that the two potential wire processing methods [IMD, *in-situ* CHPD] still have a potential for improvement. The further improvement of MgB_2 conductors involves the following main factors, i) the availability of amorphous, high purity boron powder with sizes in the 100 nm range, ii) the optimization of mass density in MgB_2 filaments, by improved densification methods, iii) the enhancement of the filling factor, which is at present higher for *in-situ* wires than for IMD processed wires, iv) mechanical and electrical stability and reliability and v) further studies on cold and hot deformation are needed in order to obtain wires with smaller filament diameters for reducing the losses in AC applications.

2.16 References

1. J. Kortus, I. I. Mazin, K. D. Belashchenko, V. P. Antropov and L. L. Boyer, Physical Review Letters **86** (20), 4656-4659 (2001).

2. J. Nagamatsu, N. Nakagawa, T. Muranaka, Y. Zenitani and J. Akimitsu, Nature **410** (6824), 63-64 (2001).

3. H. J. Choi, D. Roundy, H. Sun, M. L. Cohen and S. G. Louie, Nature **418** (6899), 758-760 (2002).

4. E. W. Collings, M. D. Sumption, M. Bhatia, M. A. Susner and S. D. Bohnenstiehl, Supercond Sci Tech **21** (10), 103001 (2008).

5. O. V. Shcherbakova, A. V. Pan and S. X. Dou, *Manesium diboride supercoductors: Development and properties*, 1st ed. (VDM Verlag Dr. Muller Aktiengesellschaft & Co. KG and licensors, Germany, 2009).

6. E. Nishibori, M. Takata, M. Sakata, H. Tanaka, T. Muranaka and J. Akimitsu, J Phys Soc Jpn **70** (8), 2252-2254 (2001).

7. X. X. Xi, Rep Prog Phys **71** (11), 116501 (2008).

8. I. I. Mazin and V. P. Antropov, Physica C **385** (1-2), 49-65 (2003).

9. T. Dahm and N. Schopohl, Physical Review Letters **91** (1) (2003).

10. A. A. Golubov, J. Kortus, O. V. Dolgov, O. Jepsen, Y. Kong, O. K. Andersen, B. J. Gibson, K. Ahn and R. K. Kremer, J Phys-Condens Mat **14** (6), 1353-1360 (2002).

11. J. Geerk, R. Schneider, G. Linker, A. G. Zaitsev, R. Heid, K. P. Bohnen and H. von Lohneysen, Physical Review Letters **94** (22), 227005 (2005).

12. A. Y. Liu, I. I. Mazin and J. Kortus, Physical Review Letters **87** (8), 087005 (2001).

13. M. Iavarone, G. Karapetrov, A. E. Koshelev, W. K. Kwok, G. W. Crabtree, D. G. Hinks, W. N. Kang, E. M. Choi, H. J. Kim, H. J. Kim and S. I. Lee, Physical Review Letters **89** (18), 187002 (2002).

14. G. Karapetrov, M. Iavarone, W. K. Kwok, G. W. Crabtree and D. G. Hinks, Physical Review Letters **86** (19), 4374-4377 (2001).

15. H. Schmidt, J. F. Zasadzinski, K. E. Gray and D. G. Hinks, Phys Rev B **63** (22), 220504 (2001).

16. F. Bouquet, R. A. Fisher, N. E. Phillips, D. G. Hinks and J. D. Jorgensen, Physical Review Letters **87** (4), 047001 (2001).

17. Y. X. Wang, T. Plackowski and A. Junod, Physica C **355** (3-4), 179-193 (2001).

18. H. D. Yang, J. Y. Lin, H. H. Li, F. H. Hsu, C. J. Liu, S. C. Li, R. C. Yu and C. Q. Jin, Physical Review Letters **87** (16), 167003 (2001).

19. P. Szabo, P. Samuely, J. Kacmarcik, T. Klein, J. Marcus, D. Fruchart, S. Miraglia, C. Marcenat and A. G. M. Jansen, Physical Review Letters **87** (13), 137005 (2001).

20. R. S. Gonnelli, D. Daghero, G. A. Ummarino, V. A. Stepanov, J. Jun, S. M. Kazakov and J. Karpinski, Physical Review Letters **89** (24), 247004 (2002).

21. W. K. Park and L. H. Greene, Rev Sci Instrum **77** (2), 023905 (2006).

22. H. Schmidt, J. F. Zasadzinski, K. E. Gray and D. G. Hinks, Physical Review Letters **88** (12), 127002 (2002).

23. F. Giubileo, D. Roditchev, W. Sacks, R. Lamy, D. X. Thanh, J. Klein, S. Miraglia, D. Fruchart, J. Marcus and P. Monod, Physical Review Letters **87** (17) (2001).

24. M. R. Eskildsen, M. Kugler, S. Tanaka, J. Jun, S. M. Kazakov, J. Karpinski and O. Fischer, Physical Review Letters **89** (18), 187003 (2002).

25. X. K. Chen, M. J. Konstantinovic, J. C. Irwin, D. D. Lawrie and J. P. Franck, Physical Review Letters **87** (15), 157002 (2001).

26. S. Tsuda, T. Yokoya, T. Kiss, Y. Takano, K. Togano, H. Kito, H. Ihara and S. Shin, Physical Review Letters **87** (17), 177006 (2001).

27. S. Souma, Y. Machida, T. Sato, T. Takahashi, H. Matsui, S. C. Wang, H. Ding, A. Kaminski, J. C. Campuzano, S. Sasaki and K. Kadowaki, Nature **423** (6935), 65-67 (2003).

28. S. Tsuda, T. Yokoya, Y. Takano, H. Kito, A. Matsushita, F. Yin, J. Itoh, H. Harima and S. Shin, Physical Review Letters **91** (12), 127001 (2003).

29. H. Uchiyama, K. M. Shen, S. Lee, A. Damascelli, D. H. Lu, D. L. Feng, Z. X. Shen and S. Tajima, Physical Review Letters **88** (15), 157002 (2002).

30. T. Takenobu, T. Ito, D. H. Chi, K. Prassides and Y. Iwasa, Phys Rev B **64** (13), 134513 (2001).

31. S. Lee, T. Masui, A. Yamamoto, H. Uchiyama and S. Tajima, Physica C **397** (1-2), 7-13 (2003).

32. M. Putti, V. Braccini, C. Ferdeghini, F. Gatti, G. Grasso, P. Manfrinetti, D. Marre, A. Palenzona, I. Pallecchi, C. Tarantini, I. Sheikin, H. U. Aebersold and E. Lehmann, Appl Phys Lett **86** (11), 112503 (2005).

33. C. Tarantini, H. U. Aebersold, V. Braccini, G. Celentano, C. Ferdeghini, V. Ferrando, U. Gambardella, F. Gatti, E. Lehmann, P. Manfrinetti, D. Marre, A. Palenzona, I. Pallecchi, I. Sheikin, I. Sheikin, A. S. Siri and M. Putti, Phys Rev B **73** (13), 134518 (2006).

34. S. Deemyad, T. Tomita, J. J. Hamlin, B. R. Beckett, J. S. Schilling, D. G. Hinks, J. D. Jorgensen, S. Lee and S. Tajima, Physica C **385** (1-2), 105-116 (2003).

35. T. Schneider and D. Di Castro, Phys Rev B **72** (5), 054501 (2005).

36. S. L. Bud'ko, R. H. T. Wilke, M. Angst and P. C. Canfield, Physica C **420** (3-4), 83-87 (2005).

37. A. Serquis, Y. T. Zhu, E. J. Peterson, J. Y. Coulter, D. E. Peterson and F. M. Mueller, Appl Phys Lett **79** (26), 4399-4401 (2001).

38. J. H. Kim, S. X. Dou, J. L. Wang, D. Q. Shi, X. Xu, M. S. A. Hossain, W. K. Yeoh, S. Choi and T. Kiyoshi, Supercond Sci Tech **20** (5), 448-451 (2007).

39. K. Vinod, R. G. A. Kumar and U. Syamaprasad, Supercond Sci Tech **20** (1), R1-R13 (2007).

40. M. Eisterer, Supercond Sci Tech **20** (12), R47-R73 (2007).

41. Z. X. Shi, A. K. Pradhan, M. Tokunaga, K. Yamazaki, T. Tamegai, Y. Takano, K. Togano, H. Kito and H. Ihara, Phys Rev B **68** (10), 104514 (2003).

42. X. H. Zeng, A. V. Pogrebnyakov, M. H. Zhu, J. E. Jones, X. X. Xi, S. Y. Xu, E. Wertz, Q. Li, J. M. Redwing, J. Lettieri, V. Vaithyanathan, D. G. Schlom, Z.-K. Liu, O. Trithaveesak and J. Schubert, Appl Phys Lett **82** (13), 2097-2099 (2003).

43. S. Y. Xu, Q. Li, E. Wertz, Y. F. Hu, A. V. Pogrebnyakov, X. H. Zeng, X. X. Xi and J. M. Redwing, Phys Rev B **68** (22), 224501 (2003).

44. H.-J. Kim, W. N. Kang, E.-M. Choi, M.-S. Kim, K. H. P. Kim and S.-I. Lee, Physical Review Letters **87** (8), 087002 (2001).

45. M. Eisterer, physica status solidi (c) **2** (5), 1606-1614 (2005).

46. R. Zeng, L. Lu, W. X. Li, J. L. Wang, D. Q. Shi, J. Horvat, S. X. Dou, M. Bhatia, M. Sumption, E. W. Collings, J. M. Yoo, M. Tomsic and M. Rindfleisch, J Appl Phys **103** (8), 083911 (2008).

47. R. Zeng, L. Lu, J. L. Wang, J. Horvat, W. X. Li, D. Q. Shi, S. X. Dou, M. Tomsic and M. Rindfleisch, Supercond Sci Tech **20** (8), L43-L47 (2007).

48. H. Fujii, K. Togano and H. Kumakura, Supercond Sci Tech **15** (11), 1571-1576 (2002).

49. H. Yamada, M. Hirakawa, H. Kumakura, A. Matsumoto and H. Kitaguchi, Appl Phys Lett **84** (10), 1728-1730 (2004).

50. D. C. Larbalestier, L. D. Cooley, M. O. Rikel, A. A. Polyanskii, J. Jiang, S. Patnaik, X. Y. Cai, D. M. Feldmann, A. Gurevich, A. A. Squitieri, M. T. Naus, C. B. Eom, E. E. Hellstrom, R. J. Cava, K. A. Regan, N. Rogado, M. A. Hayward, T. He, J. S. Slusky, P. Khalifah, K. Inumaru and M. Haas, Nature **410** (6825), 186-189 (2001).

51. C. Fischer, C. Rodig, W. Hassler, O. Perner, J. Eckert, K. Nenkov, G. Fuchs, H. Wendrock, B. Holzapfel and L. Schultz, Appl Phys Lett **83** (9), 1803-1805 (2003).

52. H. Fang, S. Padmanabhan, Y. X. Zhou and K. Salama, Appl Phys Lett **82** (23), 4113-4115 (2003).

53. A. Kario, R. Nast, W. Hassler, C. Rodig, C. Mickel, W. Goldacker, B. Holzapfel and L. Schultz, Supercond Sci Tech **24** (7), 075011 (2011).

54. C. F. Liu, G. Yan, S. J. Du, W. Xi, Y. Feng, P. X. Zhang, X. Z. Wu and L. Zhou, Physica C **386**, 603-606 (2003).

55. A. Polyanskii, V. Beilin, I. Felner, M. I. Tsindlekht, E. Yashchin, E. Dul'kin, E. Galstyan, M. Roth, B. Senkowicz and E. Hellstrom, Supercond Sci Tech **17** (3), 363-370 (2004).

56. K. Yamamoto, K. Osamura, S. Balamurugan, T. Nakamura, T. Hoshino and I. Muta, Supercond Sci Tech **16** (9), 1052-1058 (2003).

57. A. Serquis, L. Civale, D. L. Hammon, J. Y. Coulter, X. Z. Liao, Y. T. Zhu, D. E. Peterson and F. M. Mueller, Appl Phys Lett **82** (11), 1754-1756 (2003).

58. R. A. Ribeiro, S. L. Bud'ko, C. Petrovic and P. C. Canfield, Physica C **385** (1-2), 16-23 (2003).

59. R. A. Ribeiro, S. L. Bud'ko, C. Petrovic and P. C. Canfield, Physica C **382** (2-3), 194-202 (2002).

60. S. K. Chen, K. A. Yates, M. G. Blamire and J. L. MacManus-Driscoll, Supercond Sci Tech **18** (11), 1473-1477 (2005).

61. Y. Zhang, X. Xu, Y. Zhao, J. H. Kim, C. Lu, S. H. Zhou and S. X. Dou, Supercond Sci Tech **21** (11), 115004 (2008).

62. X. Xu, J. H. Kim, W. K. Yeoh, Y. Zhang and S. X. Dou, Supercond Sci Tech **19** (11), L47-L50 (2006).

63. X. Xu, M. J. Qin, K. Konstantinov, D. I. dos Santos, W. K. Yeoh, J. H. Kim and S. X. Dou, Supercond Sci Tech **19** (6), 466-469 (2006).

64. A. Yamamoto, J. Shimoyama, S. Ueda, Y. Katsura, I. Iwayama, S. Horii and K. Kishio, Physica C **445**, 806-810 (2006).

65. A. Yamamoto, J. Shimoyama, S. Ueda, I. Iwayama, Y. Katsura, S. Horii and K. Kishio, J Phys Conf Ser **43**, 111-114 (2006).

66. M. S. A. Hossain, A. Motaman, X. Xu, K. W. See, O. Cicek, H. Agil, E. Ertekin, A. Gencer, K. Cheong, M. Maeda and S. X. Dou, Mater Lett **91**, 356-358 (2013).

67. A. Yamamoto, J. Shimoyama, S. Ueda, Y. Katsura, I. Iwayama, S. Horii and K. Kishio, Appl Phys Lett **86** (21) (2005).

68. F. Bouquet, Y. Wang, I. Sheikin, P. Toulemonde, M. Eisterer, H. W. Weber, S. Lee, S. Tajima and A. Junod, Physica C **385** (1-2), 192-204 (2003).

69. V. Ferrando, P. Manfrinetti, D. Marre, M. Putti, I. Sheikin, C. Tarantini and C. Ferdeghini, Phys Rev B **68** (9), 094517

(2003).

70. A. Gurevich, S. Patnaik, V. Braccini, K. H. Kim, C. Mielke, X. Song, L. D. Cooley, S. D. Bu, D. M. Kim, J. H. Choi, L. J. Belenky, J. Giencke, M. K. Lee, W. Tian, X. Q. Pan, A. Siri, E. E. Hellstrom, C. B. Eom and D. C. Larbalestier, Supercond Sci Tech **17** (2), 278-286 (2004).

71. Werthame.Nr, E. Helfand and Hohenber.Pc, Phys Rev **147** (1), 295-& (1966).

72. A. Gurevich, Physica C **456** (1-2), 160-169 (2007).

73. Y. Iwasa, D. C. Larbalestier, M. Okada, R. Penco, M. D. Sumption and X. Xiaoxing, Applied Superconductivity, IEEE Transactions on **16** (2), 1457-1464 (2006).

74. V. Braccini, A. Gurevich, J. E. Giencke, M. C. Jewell, C. B. Eom, D. C. Larbalestier, A. Pogrebnyakov, Y. Cui, B. T. Liu, Y. F. Hu, J. M. Redwing, Q. Li, X. X. Xi, R. K. Singh, R. Gandikota, J. Kim, B. Wilkens, N. Newman, J. Rowell, B. Moeckly, V. Ferrando, C. Tarantini, D. Marre, M. Putti, C. Ferdeghini, R. Vaglio and E. Haanappel, Phys Rev B **71** (1), 012504 (2005).

75. J. M. Rowell, Supercond Sci Tech **16** (6), R17-R27 (2003).

76. Y. Eltsev, K. Nakao, S. Lee, T. Masui, N. Chikumoto, S. Tajima, N. Koshizuka and M. Murakami, Phys Rev B **66** (18), 180504 (2002).

77. Y. Eltsev, S. Lee, K. Nakao, N. Chikumoto, S. Tajima, N. Koshizuka and M. Murakami, Physica C **378**, 61-64 (2002).

78. P. C. Canfield, D. K. Finnemore, S. L. Bud'ko, J. E. Ostenson, G. Lapertot, C. E. Cunningham and C. Petrovic, Physical Review Letters **86** (11), 2423-2426 (2001).

79. A. V. Pogrebnyakov, J. M. Redwing, J. E. Jones, X. X. Xi, S. Y. Xu, Q. Li, V. Vaithyanathan and D. G. Schlom, Appl Phys Lett **82** (24), 4319-4321 (2003).

80. N. Rogado, M. A. Hayward, K. A. Regan, Y. Y. Wang, N. P. Ong, H. W. Zandbergen, J. M. Rowell and R. J. Cava, J Appl Phys **91** (1), 274-277 (2002).

81. A. Sidorenko, V. Zdravkov, V. Ryazanov, S. Horn, S. Klimm, R. Tidecks, A. Wixforth, T. Koch and T. Schimmel, Philos Mag **85** (16), 1783-1790 (2005).

82. D. Dew-Hughes, Low Temp Phys+ **27** (9-10), 713-722 (2001).

83. S. Ueda, J. Shimoyama, I. Iwayama, A. Yamamoto, Y. Katsura, S. Horii and K. Kishio, Appl Phys Lett **86** (22), 222502 (2005).

84. X. Y. Song, S. E. Babcock, C. B. Eom, D. C. Larbalestier, K. A. Regan, R. J. Cava, S. L. Bud'Ko, P. C. Canfield and D. K. Finnemore, Supercond Sci Tech **15** (4), 511-518 (2002).

85. D. Dew-Hughes, Philos Mag **30** (2), 293-305 (1974).

86. M. J. Qin, X. L. Wang, H. K. Liu and S. X. Dou, Phys Rev B **65** (13), 132508 (2002).

87. A. Motaman, M. S. A. Hossain, X. Xu, K. W. See, K. C. Chung and S. X. Dou, Supercond Sci Tech **26** (8), 085013 (2013).

88. R. Griessen, H.-h. Wen, A. J. J. van Dalen, B. Dam, J. Rector, H. G. Schnack, S. Libbrecht, E. Osquiguil and Y. Bruynseraede, Physical Review Letters **72** (12), 1910-1913 (1994).

89. G. Blatter, M. V. Feigel'man, V. B. Geshkenbein, A. I. Larkin and V. M. Vinokur, Reviews of Modern Physics **66** (4), 1125-1388 (1994).

90. W. K. Yeoh and S. Dou, Physica C **456** (1-2), 170-179 (2007).

91. M. J. Mehl, D. A. Papaconstantopoulos and D. J. Singh, Physical Review B - Condensed Matter and Materials Physics **64** (14), 1405091-1405094 (2001).

92. H. Schmidt, K. E. Gray, D. G. Hinks, J. F. Zasadzinski, M. Avdeev, J. D. Jorgensen and J. C. Burley, Phys Rev B **68** (6), 060508 (2003).

93. D. R. Smith, S. Schultz, P. Markoš and C. M. Soukoulis, Phys Rev B **65** (19), 195104 (2002).

94. S. J. Balaselvi, N. Gayathri, A. Bharathi, V. S. Sastry and Y. Hariharan, Physica C: Superconductivity and its Applications **407** (1-2), 31-38 (2004).

95. M. Avdeev, J. D. Jorgensen, R. A. Ribeiro, S. L. Bud'ko and P. C. Canfield, Physica C:

Superconductivity and its Applications **387** (3-4), 301-306 (2003).

96. S. M. Kazakov, R. Puzniak, K. Rogacki, A. V. Mironov, N. D. Zhigadlo, J. Jun, C. Soltmann, B. Batlogg and J. Karpinski, Phys Rev B **71** (2), 024533 (2005).

97. S. Soltanian, J. Horvat, X. L. Wang, P. Munroe and S. X. Dou, Physica C: Superconductivity and its Applications **390** (3), 185-190 (2003).

98. Z. X. Shi, M. A. Susner, M. D. Sumption, E. W. Collings, X. Peng, M. Rindfleisch and M. J. Tomsic, Supercond Sci Tech **24** (6), 065015 (2011).

99. Z. Q. Ma, Y. C. Liu, Q. Zhao, Z. Z. Dong and L. M. Yu, Supercond Sci Tech **22** (8), 085015 (2009).

100. W. X. Li, R. Zeng, L. Lu, Y. Li and S. X. Dou, J Appl Phys **106** (9), 093906 (2009).

101. A. Serquis, G. Serrano, S. M. Moreno, L. Civale, B. Maiorov, F. Balakirev and M. Jaime, Supercond Sci Tech **20** (4), L12-L15 (2007).

102. W. K. Yeoh, J. H. Kim, J. Horvat, S. X. Dou and P. Munroe, Supercond Sci Tech **19** (2), L5-L8 (2006).

103. W. K. Yeoh, J. Horvat, S. X. Dou and P. Munroe, Ieee T Appl Supercon **15** (2 PART III), 3284-3287 (2005).

104. P. Lezza, C. Senatore and R. Flukiger, Supercond Sci Tech **19** (10), 1030-1033 (2006).

105. A. Yamamoto, J. Shimoyama, S. Ueda, I. Iwayama, S. Horii and K. Kishio, Supercond Sci Tech **18** (10), 1323-1328 (2005).

106. S. Barua, M. S. A. Hossain, Z. Ma, D. Patel, M. Mustapic, M. Somer, S. Acar, I. Kokal, A. Morawski, T. Cetner, D. Gajda and S. X. Dou, Scripta Mater **104** (0), 37-40 (2015).

107. A. Vajpayee, V. P. S. Awana, G. L. Bhalla, P. A. Bhobe, A. K. Nigam and H. Kishan, Supercond Sci Tech **22** (1), 015016 (2009).

108. J. H. Kim, S. Oh, Y. U. Heo, S. Hata, H. Kumakura, A. Matsumoto, M. Mitsuhara, S. Choi, Y. Shimada, M. Maeda, J. L. MacManus-Driscoll and S. X. Dou, Npg Asia Mater **4**, E3 (2012).

109. J. H. Kim, S. Oh, H. Kumakura, A. Matsumoto, Y. U. Heo, K. S. Song, Y. M. Kang, M. Maeda, M. Rindfleisch, M. Tomsic, S. Choi and S. X. Dou, Adv Mater **23** (42), 4942-4946 (2011).

110. M. S. A. Hossain, C. Senatore, R. Flukiger, M. A. Rindfleisch, M. J. Tomsic, J. H. Kim and S. X. Dou, Supercond Sci Tech **22** (9), 095004 (2009).

111. Z. S. Gao, Y. W. Ma, X. P. Zhang, D. L. Wang, Z. G. Yu, H. Yang, H. H. Wen and E. Mossang, J Appl Phys **102** (1), 013914

(2007).

112. C. Shekhar, R. Giri, R. S. Tiwari, O. N. Srivastava and S. K. Malik, J Appl Phys **102** (9), 093910 (2007).

113. A. Morawski, W. Pachla, D. Kuzmenko, T. Lada, A. Zaleski, O. Eibl, W. Haessler and P. Kovac, Low Temperature Physics, Pts A and B **850**, 605-606 (2006).

114. X. P. Zhang, D. L. Wang, Z. S. Gao, L. Wang, Y. P. Qi, Z. Y. Zhang, Y. W. Ma, S. Awaji, G. Nishijima, K. Watanabe, E. Mossang and X. Chaud, Supercond Sci Tech **23** (2), 025024 (2010).

115. O. V. Shcherbakova, A. V. Pan, J. L. Wang, A. V. Shcherbakov, S. X. Dou, D. Wexler, E. Babic, M. Jercinovic and O. Husnjak, Supercond Sci Tech **21** (1), 015005 (2008).

116. K. S. B. De Silva, X. Xu, W. X. Li, Y. Zhang, M. Rindfleisch and M. Tomsic, Ieee T Appl Supercon **21** (3), 2686-2689 (2011).

117. X. Xu, W. X. Li, Y. Zhang, K. S. B. De Silva, J. H. Kim and S. Choi, J Nanosci Nanotechno **12** (2), 1402-1405 (2012).

118. K. S. B. De Silva, X. Xu, X. L. Wang, D. Wexler, D. Attard, F. Xiang and S. X. Dou, Scripta Mater **67** (10), 802-805 (2012).

119. K. S. B. De Silva, S. Gambhir, X. L. Wang, X. Xu, W. X. Li, D. L. Officer, D. Wexler, G. G. Wallace and S. X. Dou, J Mater Chem **22** (28), 13941-13946 (2012).

120. X. Xu, S. X. Dou, X. L. Wang, J. H. Kim, J. A. Stride, M. Choucair, W. K. Yeoh, R. K. Zheng and S. P. Ringer, Supercond Sci Tech **23** (8), 085003 (2010).

121. H. Fujii, K. Togano, H. Kumakura and K. Ozawa, Supercond Sci Tech **20** (6), 579-583 (2007).

122. S. C. Yan, G. Yan, Y. F. Lu and L. Zhou, Supercond Sci Tech **20** (6), 549-553 (2007).

123. R. Zeng, S. X. Dou, L. Lu, W. X. Li, J. H. Kim, P. Munroe, R. K. Zheng and S. P. Ringer, Appl Phys Lett **94** (4), 042510 (2009).

124. A. Yamamoto, J. Shimoyama, I. Iwayama, Y. Katsura, S. Horii and K. Kishio, Physica C **463**, 807-811 (2007).

125. O. Shcherbakova, S. X. Dou, S. Soltanian, D. Wexler, M. Bhatia, M. Sumption and E. W. Collings, J Appl Phys **99** (8), 08M510 (2006).

126. W. Pachla, A. Morawski, P. Kovac, I. Husek, A. Mazur, T. Lada, R. Diduszko, T. Melisek, V. Strbik and M. Kulczyk, Supercond Sci Tech **19** (1), 1-8 (2006).

127. M. A. Susner, M. D. Sumption, M. Bhatia, X. Peng, M. J. Tomsic, M. A. Rindfleisch and E. W. Collings, Physica C: Superconductivity and its Applications **456** (1-2), 180-187 (2007).

128. S. X. Dou, S. Soltanian, J. Horvat, X. L. Wang, S. H. Zhou, M. Ionescu, H. K. Liu, P. Munroe and M. Tomsic, Appl Phys Lett **81** (18), 3419-3421 (2002).

129. S. X. Dou, A. V. Pan, S. Zhou, M. Ionescu, X. L. Wang, J. Horvat, H. K. Liu and P. R. Munroe, J Appl Phys **94** (3), 1850-1856 (2003).

130. A. Matsumoto, H. Kumakura, H. Kitaguchi, B. J. Senkowicz, M. C. Jewell, E. E. Hellstrom, Y. Zhu, P. M. Voyles and D. C. Larbalestier, Appl Phys Lett **89** (13), 132508 (2006).

131. A. Matsumoto, H. Kumakura, H. Kitaguchi and H. Hatakeyama, Supercond Sci Tech **16** (8), 926-930 (2003).

132. S. I. Schlachter, W. Goldacker, A. Frank, B. Ringsdorf and H. Orschulko, Cryogenics **46** (2-3), 201-207 (2006).

133. M. D. Sumption, M. Bhatia, S. X. Dou, M. Rindfliesch, M. Tomsic, L. Arda, M. Ozdemir, Y. Hascicek and E. W. Collings, Superconductor Science and Technology **17** (10), 1180-1184 (2004).

134. A. Serquis, L. Civale, D. L. Hammon, G. Serrano and V. F. Nesterenko, Ieee T Appl Supercon **15** (2), 3188-3191 (2005).

135. Y. W. Ma, X. P. Zhang, A. X. Xu, X. H. Li, L. Y. Xiao, G. Nishijima, S. Awaji, K. Watanabe, Y. L. Jiao, L. Xiao, X. D. Bai, K. H. Wu and H. H. Wen, Supercond Sci Tech **19** (1), 133-137 (2006).

136. Y. W. Ma, X. P. Zhang, G. Nishijima, K. Watanabe, S. Awaji and X. D. Bai, Appl Phys Lett **88** (7), 072502 (2006).

137. J. H. Kim, S. Zhou, M. S. A. Hossain, A. V. Pan and S. X. Dou, Appl Phys Lett **89** (14), 142505 (2006).

138. H. Yamada, M. Hirakawa, H. Kumakura and H. Kitaguchi, Superconductor Science and Technology **19** (2), 175-177 (2006).

139. D. Patel, M. S. A. Hossain, A. Motaman, S. Barua, M. Shahabuddin and J. H. Kim, Cryogenics **63** (0), 160-165 (2014).

140. S. Ueda, J. Shimoyama, A. Yamamoto, Y. Katsura, I. Iwayama, S. Horii and K. Kishio, Physica C **426**, 1225-1230 (2005).

141. A. Yamamoto, J. I. Shimoyama, S. Ueda, Y. Katsura, S. Horii and K. Kishio, Ieee T Appl Supercon **15** (2 PART III), 3292-3295 (2005).

142. S. R. Sheng, N. L. Rowell and S. P. McAlister, Appl Phys Lett **83** (14), 2790-2792 (2003).

143. A. V. Pan, S. H. Zhou, H. K. Liu and S. X. Don, Supercond Sci Tech **16** (5), 639-644 (2003).

144. A. Serquis, L. Civale, D. L. Hammon, X. Z. Liao, J. Y. Coulter, Y. T. Zhu, M. Jaime, D. E. Peterson, F. M. Mueller, V. F. Nesterenko and Y. Gu, Appl Phys Lett **82** (17), 2847-2849 (2003).

145. T. A. Prikhna, W. Gawalek, Y. M. Savchuk, N. V. Sergienko, V. E. Moshchil, M.

Wendt, T. Habisreuther, S. N. Dub, V. S. Melnikov, A. V. Kozyrev, C. Schmidt, J. Dellith, D. Litzkendorf, P. A. Nagorny, U. Dittrich, V. B. Sverdun, L. K. Kovalev, V. T. Penkin, W. Goldacker, O. A. Rozenberg and J. Noudem, 8th European Conference on Applied Superconductivity (Eucas'07) **97**, 012022 (2008).

146. H. Yamada, M. Igarashi, Y. Nemoto, Y. Yamada, K. Tachikawa, H. Kitaguchi, A. Matsumoto and H. Kumakura, Supercond Sci Tech **23** (4), 045030 (2010).

147. J. H. Kim, A. Matsumoto, M. Maeda, Y. Yamada, K. Wada, K. Tachikawa, M. Rindfleisch, M. Tomsic and H. Kumakura, Physica C **470** (20), 1426-1429 (2010).

148. G. Giunchi, S. Raineri, R. Wesche and P. L. Bruzzone, Physica C **401** (1-4), 310-315 (2004).

149. J. M. Hur, K. Togano, A. Matsumoto, H. Kumakura, H. Wada and K. Kimura, Supercond Sci Tech **21** (3), 032001 (2008).

150. K. Togano, J. M. Hur, A. Matsumoto and H. Kumakura, Supercond Sci Tech **22** (1), 015003 (2009).

151. T. Matsushita, M. Kiuchi, A. Yamamoto, J. I. Shimoyama and K. Kishio, Supercond Sci Tech **21** (1), 015008 (2008).

152. W. Pachla, P. Kovac, R. Diduszko, A. Mazur, I. Husek, A. Morawski and A. Presz, Supercond Sci Tech **16** (1), 7-13 (2003).

153. W. Pachla, P. Kovac, I. Husek, T. Melisek, M. Muler, V. Strbik, A. Mazur and A. Presz, Supercond Sci Tech **18** (4), 552-556 (2005).

154. P. Kovac, I. Husek, W. Pachla and M. Kulczyk, Supercond Sci Tech **20** (7), 607-610 (2007).

155. R. Flukiger, M. S. A. Hossain and C. Senatore, Supercond Sci Tech **22** (8), 085002 (2009).

156. R. Flukiger, M. S. A. Hossain, M. Kulich and C. Senatore, Advances in Cryogenic Engineering, Vol 58 **1435**, 353-362 (2012).

157. G. Z. Li, M. D. Sumption, J. B. Zwayer, M. A. Susner, M. A. Rindfleisch, C. J. Thong, M. J. Tomsic and E. W. Collings, Supercond Sci Tech **26** (9), 095007 (2013).

158. M. S. A. Hossain, C. Senatore, M. Rindfleisch and R. Flukiger, Supercond Sci Tech **24** (7), 075013 (2011).

159. S. J. Ye, A. Matsumoto, K. Togano, T. Ohmura and H. Kumakura, Supercond Sci Tech **26** (10), 105027 (2013).

160. M. S. A. Hossain, A. Motaman, S. Barua, D. Patel, M. Mustapic, J. H. Kim, M. Maeda, M. Rindfleisch, M. Tomsic, O. Cicek, T. Melisek, L. Kopera, A. Kario, B. Ringsdorf, B. Runtsch, A. Jung, S. X. Dou, W. Goldacker and P. Kovac, Supercond Sci Tech **27** (9), 095016 (2014).

161. M. Kulich, R. L. Flukiger, C. Senatore, M. Tropeano and R. Piccardo, Supercond Sci Tech **26** (10), 105019 (2013).

162. P. Kovac, I. Hugek, T. Meligek, J. C. Grivel, W. Pachla, V. Strbik, R. Diduszko, J. Homeyer and N. H. Andersen, Supercond Sci Tech **17** (10), L41-L46 (2004).

163. R. Flükiger, M. S. A. Hossain, C. Senatore and M. Rindfleisch, Physica C: Superconductivity **471** (21–22), 1119-1123 (2011).

164. R. Flukiger, M. S. Al Hossain, C. Senatore, F. Buta and M. Rindfleisch, Applied Superconductivity, IEEE Transactions on **21** (3), 2649-2654 (2011).

165. P. Kovac, T. Melisek and I. Husek, Supercond Sci Tech **18** (7), L45-L48 (2005).

166. W. Hassler, P. Kovac, M. Eisterer, A. B. Abrahamsen, M. Herrmann, C. Rodig, K. Nenkov, B. Holzapfel, T. Melisek, M. Kulich, M. v Zimmermann, J. Bednarcik and J. C. Grivel, Supercond Sci Tech **23** (6), 065011 (2010).

167. C. Zhou, P. Gao, H. J. G. Krooshoop, M. Dhalle, M. D. Sumption, M. Rindfleisch, M. Tomsic, M. Kulich, C. Senatore and A. Nijhuis, Supercond Sci Tech **27** (7), 075002 (2014).

168. C. Senatore, M. S. Al Hossain and R. Flukiger, Applied Superconductivity, IEEE Transactions on **21** (3), 2680-2685 (2011).

CHAPTER 3: EXPERIMENTAL METHODS

3.1 Sample preparation

3.1.1 Fabrication of MgB_2 bulk samples

Fabrication of polycrystalline bulk samples are very important step for studying the properties of the superconducting materials. There are two major processes called *in-situ* and *ex-situ* process generally used in fabrication of MgB_2. In this thesis, MgB_2 bulk was fabricated by using *in-situ* method from the starting materials: Mg powder (99%, 325 mesh), amorphous boron powder (98.8%) with or without carbon encapsulation and dopant (i.e. SiC, Al_2O_3). The homogenously mixed powers were pressed into 13.0 mm diameter pellets of 1.0 mm in thickness by applying uniaxial pressure in 10 ton hydraulic press, and then the pellets were encapsulated into an iron tube. The samples were sintered at 700 °C for 30minutes in quartz tube furnace at the heating rate of $5^oC\ min^{-1}$ under high purity argon (Ar 99.9%) gas atmosphere.

3.1.2 Fabrication of MgB_2 wire

For making MgB_2 wires and tape, different methods have been used by disparate group of researchers. Most popular *in-situ* techniques so far reported are powder in tube (PIT) method, continuous tube forming and filling (CTFF) method developed by Hyper Tech Research Inc. and internal magnesium diffusion (IMD) method, etc. All these methods have some advantages and disadvantages over each other. The most common is PIT method, in which solid structure can be obtained, but the J_c is comparatively lower than the other fabrication process (i.e. IMD and CTFF) due to less connectivity. In the CTFF method multiple sheath materials are used and suitable long length solid structure can be obtained in this fast fabrication process. Similar to PIT method, it has also connectivity problems. On the other hand, IMD process ensures better connectivity and higher J_c. The problem associated with this process is the presence of

hollow structure inside the wire, which makes it brittle. To confront this problem, in this work PIT method was used to fabricate the wire along with further densification process, such as CHPD, cold isostatic pressing (CIP) and hot isostatic pressing (HIP).

3.1.2.1 Powder in tube (PIT)

For investigation of MgB_2 wire performance, wires were fabricated by *in-situ* powder in tube (PIT) method. In the PIT method, the stoichiometric mixture of boron powder (with or without carbon encapsulation) and Mg powder (325 mesh or 30-80 mesh) were homogenously mixed in the mortar by pestle for 30~40 min. Then the powder mixture were filled into the tube (Monel or Cu) and packed gently. After that, two ends of the tube were sealed with aluminum foil. A complementary swaging and drawing process were employed to reduce the diameter of the metal tube to a desired diameter in a 10% step size. Generally, the final diameter after the drawing process is 0.83mm or 1.00 mm. Wire sample also heat treated in a similar way of bulk samples.

3.1.2.2 Cold isostatic pressing (CIP)

To increase the connectivity between the MgB_2 grains different types of pressure was employed. Different research groups studied the effect of pressure before the heat treatment and during the heat treatment. CHPD is applied to the wires before the heat treatment process. Cold isostatic pressing (CIP) is another interesting method of applying pressure during the (Mg + 2B) billet preparation. In this process, pressure is applied from the multiple direction isostatically for getting highly densified billet. To apply CIP, mixture of (Mg + 2B) is filled into a rubber tube, which is immersed in an oil bath. The liquid pressure of oil is transmitted to the rubber tube uniformly, and finally, pressed billet of powder was formed. In this work, CIP was applied to the powder mixture in the Institute of High Pressure Physics (IHPP), Poland. A schematic representation of CIP process is depicted in **Figure 3.1**.

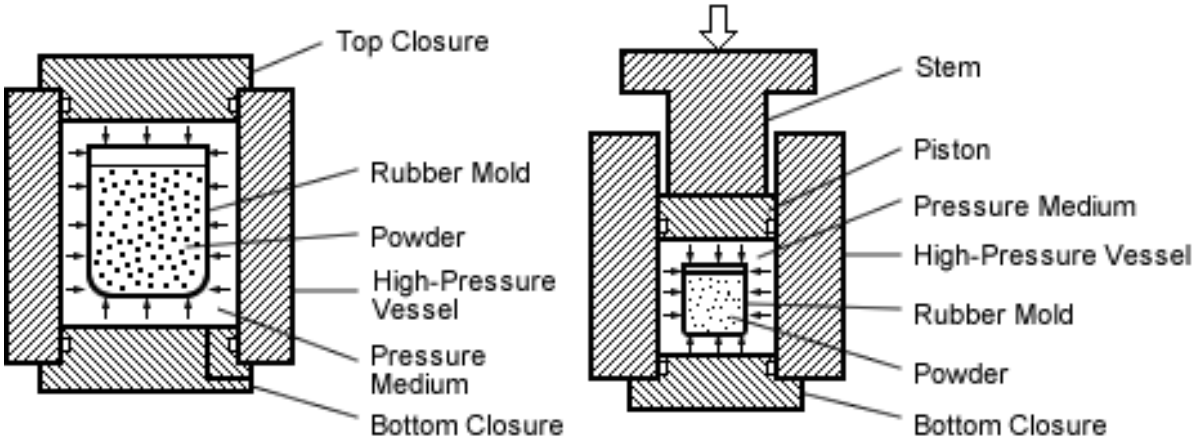

Figure 3.1 A schematic representation of Cold Isostatic Pressing (CIP) process

3.1.2.3 Hot isostatic pressing (HIP)

It was established by most research groups that low filed J_c of MgB_2 superconductor can be enhanced by increasing the grain connectivity. To do this CHPD was introduced and significant enhancement was observed. Another approach for increasing the connectivity is hot isostatic pressing (HIP). In this method, pressure is introduced during the reaction process. Yet, the method was not that much successful to reach the acceptable J_c in the beginning. In this work, HIP was used in IHPP using different medium on different kind of wires and cables, along with CHPD and the result is very encouraging. **Figure 3.2(a, b)** depicts the pictorial view of Hot Isostatic Pressing (HIP) chamber. HIP was done at 700 °C and 740 °C up to 1.6 GPa pressure. There are some problems associated with HIP and is not suitable for the production of industrial length wires due to several reasons, i.e., possibility of Ar gas trap inside the filament, too small sample chamber for reacting km-class wire. The long wires production eliminating all these issues needs a special design for the construction of the chamber. To confront this problem, University of Wollongong and Institute of High Pressure Physics (IHPP), Poland has recently developed such a new lab scale HIP device (see **Figure 3.3**).

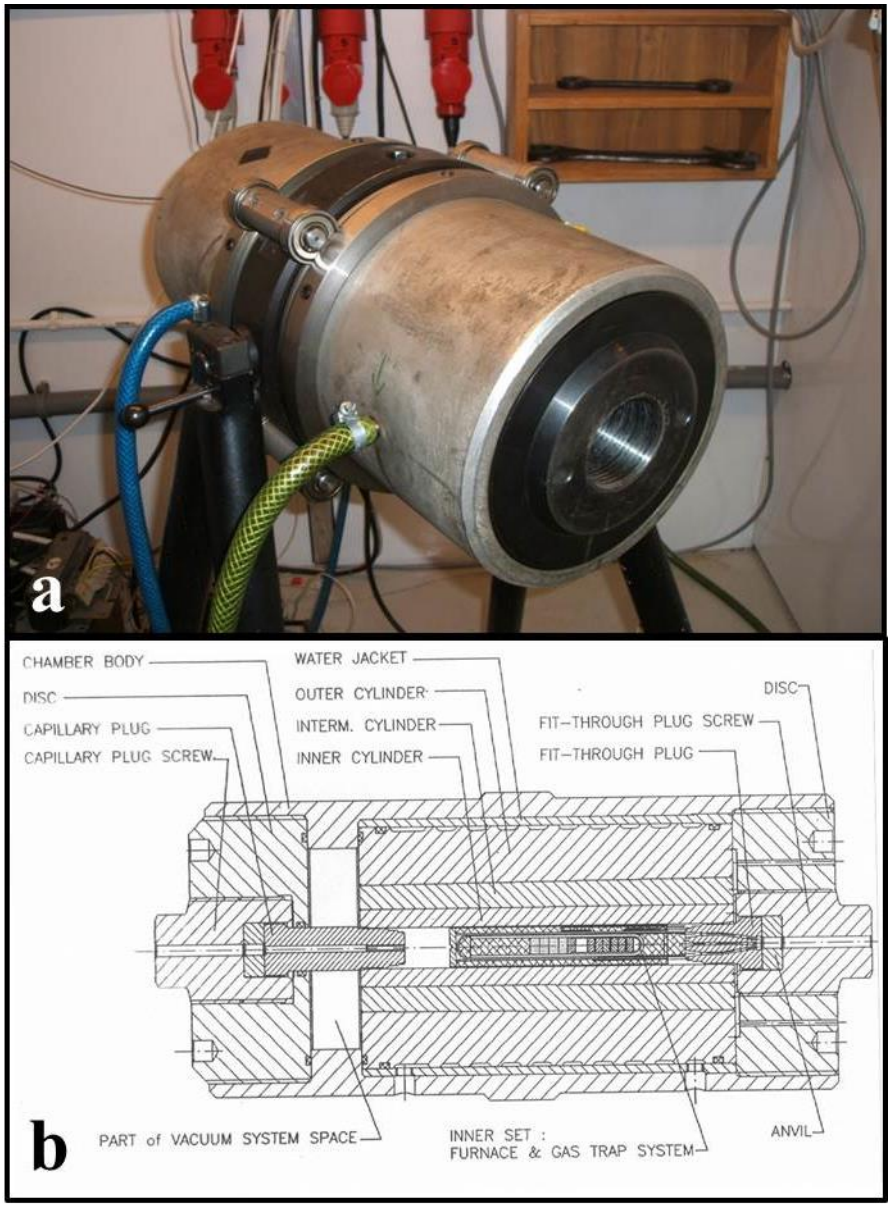

Figure 3.2 a) Pictorial view of Hot Isostatic Pressing (HIP) chamber with gas medium, and b**)** Cross sectional view of the HIP chamber in gas medium.

In this device (see **Figure 3.3**), molten salt (specific eutectic mixture of salts (i.e NaCl and KCl) along with Boron Nitride (BN)) is used as a pressing medium instead of gas which can easily trapped into the filament. BN is used for its significant chemical stability and plasticity. In this process, a long wire sample is kept inside the salt bed in a sealed high pressure chamber. At desired temperature solid salt mixture melts in the high pressure chamber. In this way, external force is applied into the liquid and the force is directly transmitted to the wire

homogeneously. This new toroid type isostatic hot press makes it possible to produce the hundreds or thousands meters of thin MgB_2 wires, ready for use in high performance superconducting systems.

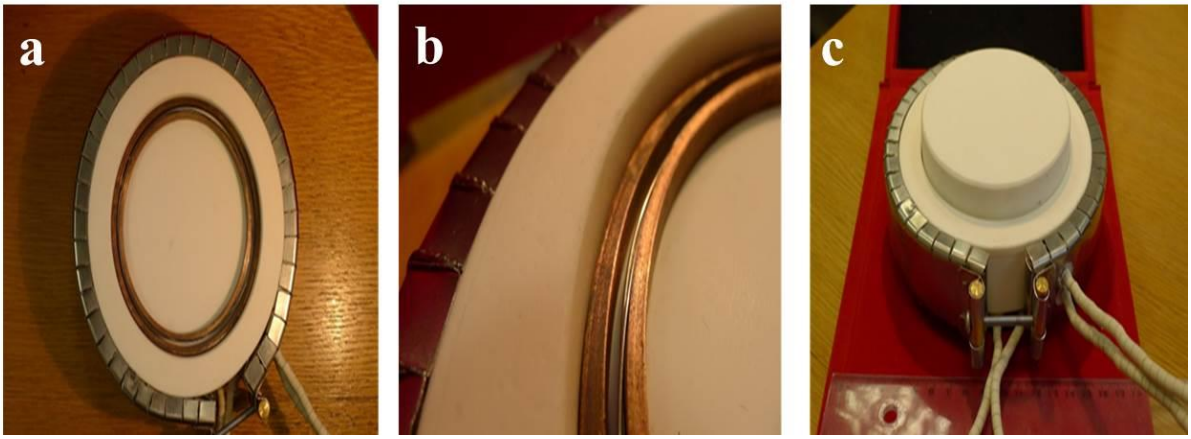

Figure 3.3 The image of lab scale toroidal type salt bed HIP device. In **(a and b)** wire is placed inside the groove, **c)** outside view of the system after sample installment.

The pictorial schematic design of the first prototype of liquid salt based HIP machine has been shown in **Figure 3.3**. The second stage densification after CHPD using toroidal HIP chamber has recently been applied on optimized CHPD treated wires under the collaboration between University of Wollongong, Australia and Institute for High Pressure Physics (Unipress), Poland. The record high J_c has been obtained for the *in-situ* PIT wires and this result is well comparable with the second generation MgB_2 wires produced by Advanced Internal Magnesium Infiltration (AIMI) technique[1] reported by Hyper Tech, Research, USA.

3.1.2.4 Continuous tube forming and filling (CTFF)

The continuous tube forming and filling (CTFF) method is a patented process of Hyper Tech Research Inc. and vary fast wire fabrication technique for MgB_2 conductors[2]. **Figure 3.4** depicts the conceptual schematic view of CTFF process**.** In this technique, a continuous metal strip of niobium (Nb) is used as the inner barrier. As this metal ribbon goes through the tube forming dies, it gradually turns into a 'U' shape. Then, the powder mixture of magnesium (Mg)

and boron (B) is poured into the 'U' shape metal strip. After filling the powder, the tube is closed off through the closing dies. The tube filled with powder is put into another tube (i.e. Monel) for double sheathing. Then, the tube passes through series of dies to reduce the diameter into a final form (i.e. 0.832 mm). CTFF process ensures fast wire fabrication and long length production.

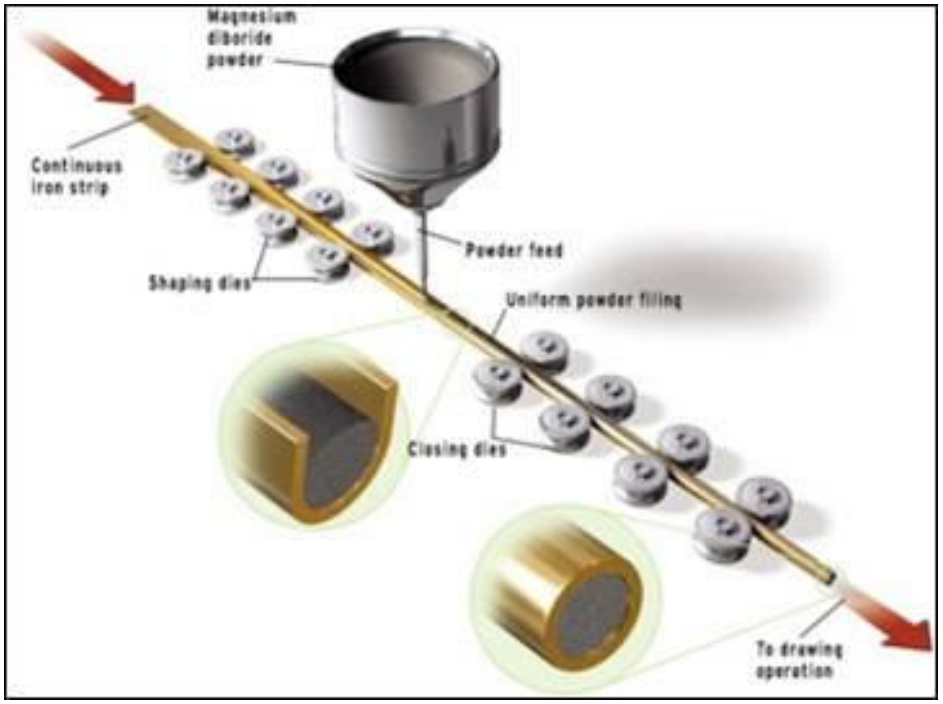

Figure 3.4 Schematic representation of the CTFF wire fabrication process[3]

In this work, CTFF wire was used in collaboration with Hyper Tech Research Inc. to characterize the superconducting performance in the University of Wollongong.

3.2 Equipment

3.2.1 Phase and Structure Characterization

3.2.1.1 Powder x-ray diffraction (XRD)

X-ray diffraction (XRD) was used to investigate the purity of the sample, the phase formation and obtained XRD patterns were evaluated to check the phases, lattice parameters, and grain

sizes. XRD was performed by using GBC MMA diffractometer with a Cu-Kα radiation source (λ = 1.54059Å). The diffraction data was collected using powder from samples and the typical scan range is 20° to 80° (2 theta) with 1°/min step size.

These X-rays are produced by a cathode ray tube, then filtered to get monochromatic radiation, collimated to concentrate them, and directed toward the sample. Using the Bragg's law, XRD pattern can be indexed. **Figure 3.5** depicts the X-ray diffraction in θ-2θ configuration[4]. Bragg's law: $n\lambda = 2d\sin\theta$, where, λ = wave length, n is an integer, θ = diffraction angle and d lattice spacing.

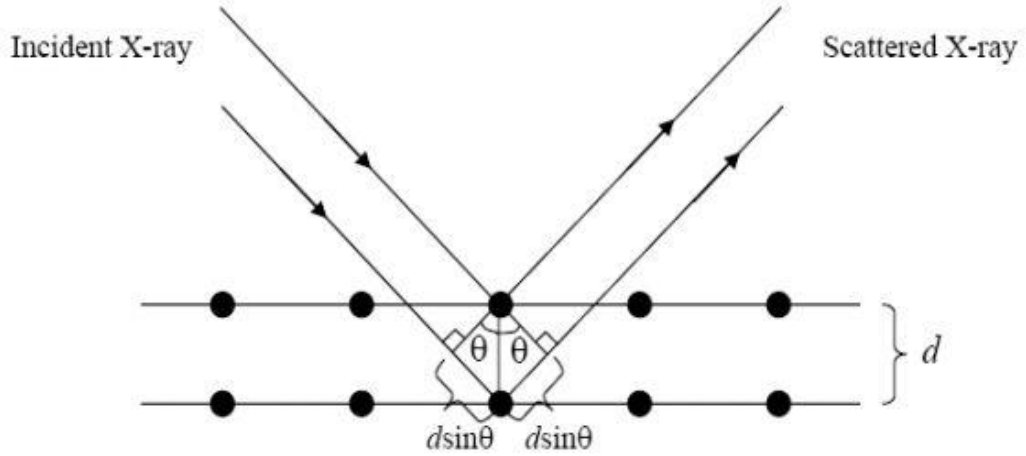

Figure 3.5 The X-ray diffraction in θ-2θ configuration[4]

From the XRD pattern, the lattice parameters were calculated by using the Rietveld refinement method[5]. The grain sizes and the strain were calculated from Williamson-Hall plot. The full-width-at-half-maximum (FWHM) of the characteristic peak of different samples was obtained by using Traces 6.3.0 software. FWHM indicates grain size of the sample. According to Scherrer's formula ($D_p = 0.94\lambda / \beta_{1/2} \cos\theta$, where D_p is crystal size, λ is wavelength, $\beta_{1/2}$ is FWHM, and θ is peak position), the FWHM value is inversely proportional to grain size. For removing the peak broadening problem standard Si powder was used.

3.2.1.2 Scanning electron microscopy (SEM)

To observe the surface morphology, microstructure and chemical composition of the samples, the scanning electron microscope (SEM) was used. A JEOL JSM-7500FA, field emission scanning electron microscope (FESEM), was used for SEM analysis. Electron energy loss spectroscopy (EELS; JEOL ARM-200F) analysis was carried out for detecting carbon. In the SEM, a focused beam of high-energy electrons is used to observe the features down to 50Å. The electrons emitted from the Solid samples are collected to form the final image. The typical magnification of the microscope is up to several hundred thousands of times. The FESEM 7500FA is capable of determining chemical compositions using energy dispersive X-ray (EDX) analysis. To determine the energy spectrum of X-ray to characterize the elemental composition of MgB_2 samples, EDX was used.

3.2.1.3 Transmission electron microscopy (TEM)

Transmission electron microscopy (TEM) was performed on powdered sample to investigate the boron powder characteristics. Transmission electron microscopy (TEM) is a microscopy technique in which a beam of electrons is transmitted through an ultra-thin specimen, interacting with the specimen as it passes through. An image is formed based on the interaction of the electrons transmitted through the specimen. The image is magnified and focused onto an imaging device, such as a fluorescent screen, on a layer of photographic film. TEM is capable of imaging at considerably higher resolution than the normal microscope. The bright field imaging is the most common mode of operation in TEM, where imgae contrast is produced due to electron absorption in the materials. The grain size, crystal defects, and stacking fault can be determined by TEM analysis. In Figure 3.6, a schematic view of the TEM image forming technique is shown[6].

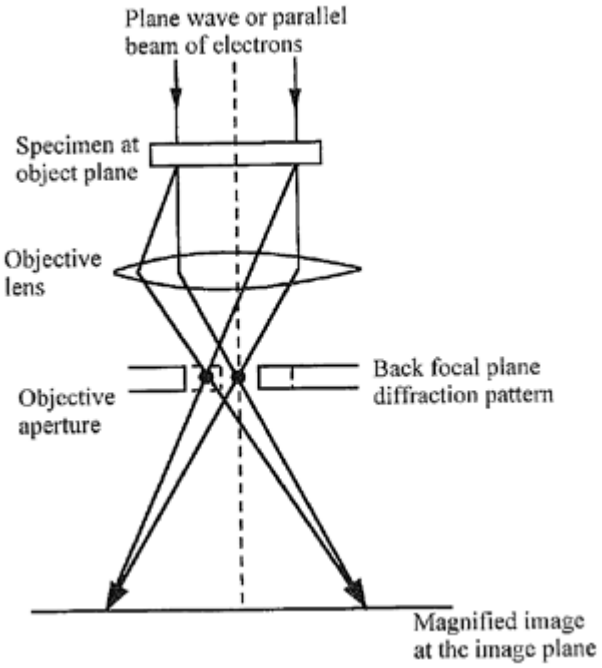

Figure 3.6 Schematic representation of the image forming technique in TEM[6]

3.2.2 Electromagnetic property characterization

The electromagnetic properties of MgB_2, such as, the critical temperature (T_c), the critical fields (B_{c2} and B_{irr}), and the critical current density (J_c) were measured using a Quantum Design physical property measurement system (PPMS). **Figure 3.7** depicts the general principal of magnetic measurement. In the magnetic measurement, the sample is located in a system of primary and secondary coils. The primary coil creates an excitation field set to frequency of 117Hz and amplitude of 0.1 Oe. On the other hand, sample located in the secondary coils, creates a change in the induction voltage through the coil due to the shielding current and it can be detected by the lock-in amplifier (see **Figure 3.7**).

The transport critical current (I_c) of the wire was measured by using standard dour probe method with $1\mu Vcm^{-1}$ criterion. In this technique, the sample is attached to sample probe in a in a particular way that the construction fulfil the four probe circuit. The current leads are connected to the outer contacts in the probe to supply the current to the sample and two inner

contacts act as a voltage tape to measure the voltage across the distance. Typically, samples were measured at 4.2 K and 20 K. Room temperature resistivity of the samples can be measured by the same method.

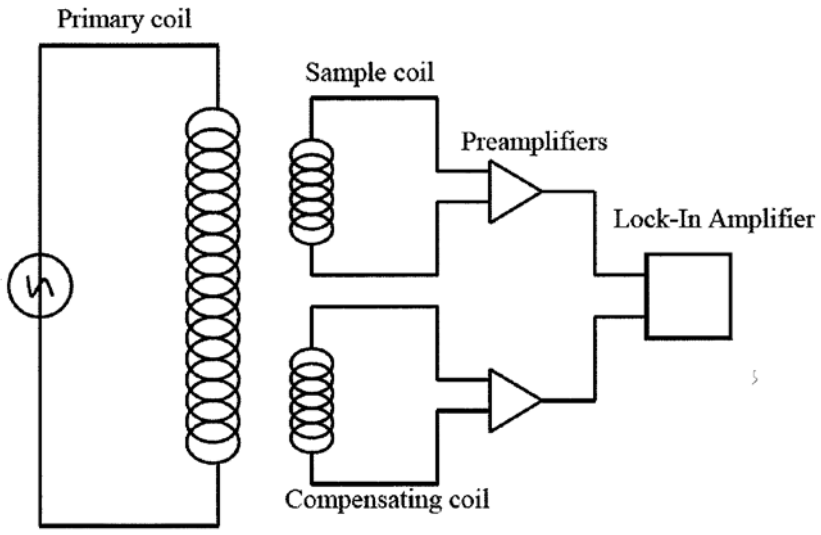

Figure 3.7 Schematic representation of mutual inductance technique for magnetic measurement.

3.2.2.1 Determination of the critical temperature (T_c)

The T_c of the superconducting materials was determined by two separate methods, (a) the alternative current (ac) susceptibility measurement at zero field and (b) the resistance measurement at zero field using a Quantum Design physical property measurement systems (PPMS). In the ac susceptibility measurement, T_c was defined as the onset of the diamagnetism by measuring the real part of the ac susceptibility. In the resistance measurement at zero field, temperature dependence resistive transition suggests the formation of energy gap in the superconductor. In here, T_c is defined as the onset of the resistivity drop to zero point. **Figure 3.8** depicts the T_c definition based on the resistivity measurement method. The residual resistivity (ρ_0) is defined as the resistivity at the transition point and it is an indicator of the impurity scattering effects.

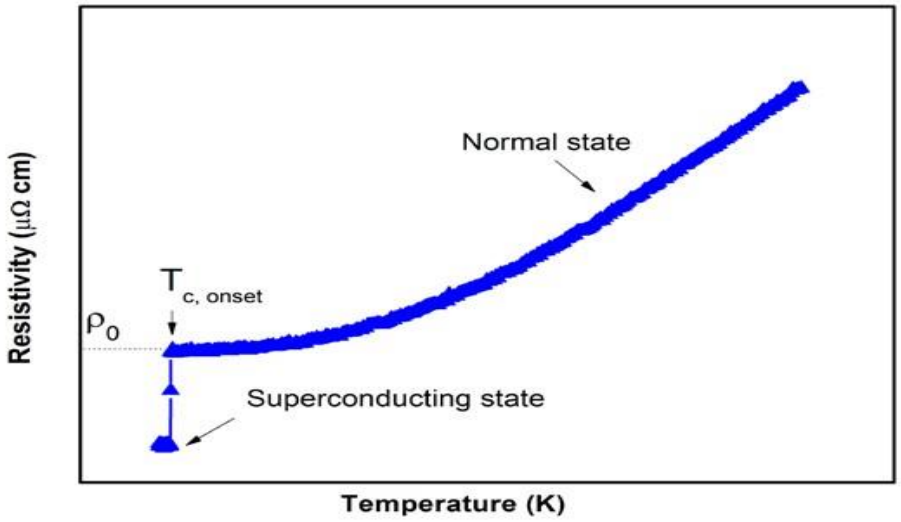

Figure 3.8 The temperature dependence of resistivity

3.2.2.2 Determination of the upper critical field (B_{c2}) and irreversibility field (B_{irr})

In this thesis, the upper critical field (B_{c2}) and the irreversibility field (B_{irr}) were determined by the resistivity measurement in dc filed from 0 to 13 T, using the 14T PPMS. In the resistivity measurement, B_{c2} and B_{irr} are defined as $R(B_{c2}, T) = 0.9\, R_{ns}$ and $R(B_{irr}, T) = 0.1\, R_{ns}$, where R_{ns} is the normal state resistance of MgB_2 at 40K.Again, B_{irr} also assumed from the magnetization measurement based on the criterion, the field at which the J_c = 100 Acm^{-2}, at a particular measuring temperature.

3.2.2.3 Determination of the critical current density (J_c)

The critical current density (J_c) of MgB_2 was measured by either (1) dc magnetization measurement through the variation of moment under different applied magnetic field or (2) dc transport critical current measurement. For bulk sample, J_c was determined from the magnetization hysteresis loop by employing the Bean approximation model[7]. For bar shaped sample, the model is expressed as

$$J_c = \frac{\frac{20\Delta M}{V}}{a\left(1-\frac{a}{3b}\right)}, \text{ [a < b]}$$

Where, ΔM is the width of the relevant M-H loop, V is the volume of the sample, *a* and *b* are the width and length of the bar shaped sample, respectively, in a plane perpendicular to the applied field. The hysteresis loop was measured over a wide range of temperature from 4.2 K 5 to 32 K. **Figure 3.9** shows the schematic representation of hysteresis loop of MgB_2. To eliminate the size effect on J_c, the dimensions of the bulk sample were maintained nearly 1mm × 2mm × 3mm in all cases.

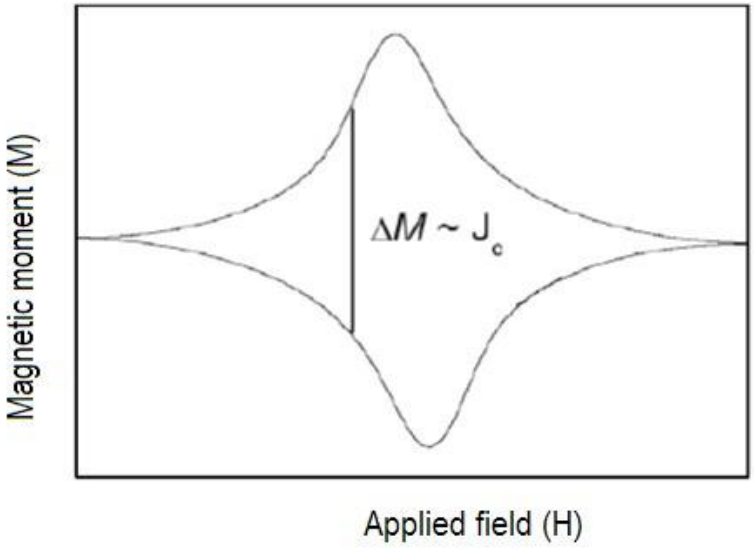

Figure 3.9 Schematic presentation of magnetic hysteresis loop of MgB_2, showing the width of the loop ΔM.

For wires and tape, the J_c was calculated from the transport I_c by dividing by superconducting cross sectional area of MgB_2. The I_c of MgB_2 was measured at 4.2 K and 20K using 15 T superconducting magnet by standard four probe method.

3.2.2.4 Determination of the transport critical current density (J_c)

The transport critical current (I_c) was measured in the 15 T superconducting magnet cryostat system. A partial conceptual diagram of the system is depicted in **Figure 3.10**. The cryostat consists of a variable temperature insert used for applications that require continuous variation

of temperature on the sample. Desired level of temperature inside the space was obtained by withdrawing a controlled amount of liquid helium from the magnet reservoir through a valve capillary tube located at the bottom. The temperature inside the chamber was varied by heating flow. An electrical heater was placed on the bottom adjacent to the capillary tube. The operating temperatures can be achieved from 4.2 K to 300 K. To reduce heat load and consumption of the liquid helium multilayer super insulation and liquid nitrogen shield was employed. The wire samples of around 4.5 cm were mounted onto two oxygen free high conductivity (OFHC) copper blocks, which served as a heat reservoir and low-resistance current leads to the sample. Two ends of the sample were soldered onto two separate copper blocks, with the soldered length of around 1.0 cm. The other ends of the copper blocks were soldered directly to the high-temperature superconductor (HTS) leads that extend 2m down to the chamber, positioning the sample in the middle of a DC superconducting magnet. An additional heater was on the sample holder for better temperature control. The magnetic field was perpendicular to the round wire. For the DC transport measurement a bipolar power source from Cryomagnetics was used as the current source. The maximum peak current was limited to 200A .The current ramping rate was fixed at $0.5As^{-1}$ for currents up to 60A and 1.0 As^{-1} hereafter. Nano voltmeter was used to measure low voltage drop. Depending on the noise and solder points, typical range of the voltage signal during the transport measurement is from 10^{-8} V to 10^{-6} V. The LabVIEW (Laboratory Virtual Instrumentation Engineering Workbench) software was used for data acquisition.

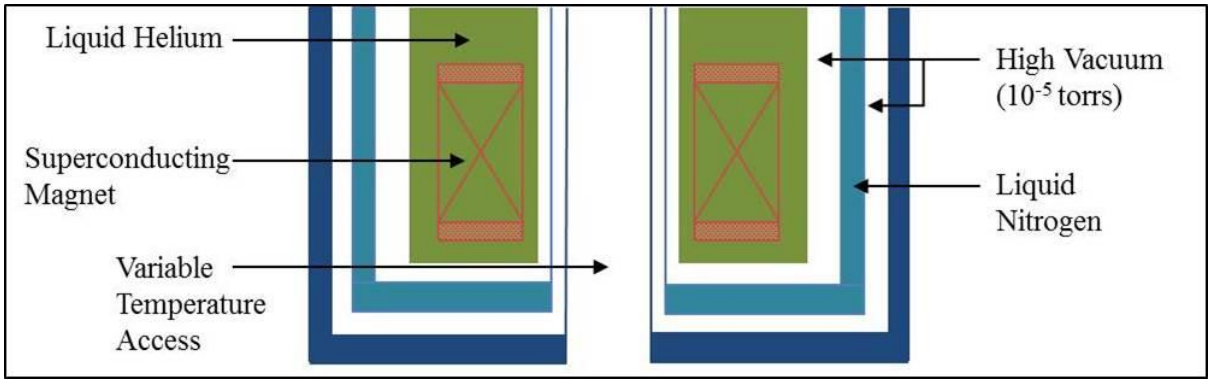

Figure 3.10 Conceptual drawing of the system used for studying superconducting samples in a magnetic field at varying temperatures

The critical current, I_c was obtained as the current giving a voltage of $1\mu Vcm^{-1}$ of sample length from the *I-V* characteristic curve. This I_c was used to calculate the transport critical current density.

3.3 References

1. G. Z. Li, M. D. Sumption, J. B. Zwayer, M. A. Susner, M. A. Rindfleisch, C. J. Thong, M. J. Tomsic and E. W. Collings, Supercond Sci Tech **26** (9) (2013).

2. M. Tomsic, M. Rindfleisch, J. Yue, K. McFadden, J. Phillips, M. D. Sumption, M. Bhatia, S. Bohnenstiehl and E. W. Collings, International Journal of Applied Ceramic Technology **4** (3), 250-259 (2007).

3. D. Patel, M. S. A. Hossain, A. Motaman, S. Barua, M. Shahabuddin and J. H. Kim, Cryogenics **63** (0), 160-165 (2014).

4. B. D. C. a. S. R. Stock, *Elements of X-Ray Diffraction*, 3rd ed. (2001).

5. H. M. Rietveld, J Appl Crystallogr **2**, 65-& (1969).

6. D. S. G. D. a. A. Cardwell, *Handbook of Superconducting Materials*, 1st ed. (Institute of Physics Publishing, London, 2003).

7. D. X. Chen and R. B. Goldfarb, J Appl Phys **66** (6), 2489-2500 (1989).

CHAPTER 4: CORRELATION BETWEEN IN-FIELD J_C ENHANCEMENT AND GRAIN CONNECTIVITY IN CO-DOPED MgB_2 SUPERCONDUCTOR

4.1 Introduction

Due to recent advances in cryocoolers, magnets for many electrical utilities may be the best optimized at temperatures of 10 to 35 K[1], a domain for which MgB_2 could provide the cheapest superconducting wires[2]. For industrial application, its in-field J_c has to be improved, however. To date, much attention has been paid to the enhancement of the high-field J_c properties of MgB_2 wires and carbon substitution on boron sites by chemical doping with nano-SiC [3], carbon nanotubes [4], nanocarbon[5], carbohydrate[6, 7], etc. has been proven to be the easiest and most effective way to enhance the flux pinning. It has been generally accepted, however, that the applications of MgB_2 in fields of 1–2 T at 20–25 K, such as in a cryogen-free magnet for MRI or fault current limiter systems, might be more practical than its high-field utilization[8]. For MgB_2, carbon dopant has proved its potential to enhance the high-field properties, although researchers are still struggling to improve the low-field J_c for such applications. Among the aforementioned dopants, in this work, we have considered nano-size SiC, which is one of the most effective dopants for MgB_2. The cumulative effect by dual reaction model[9] (substitution for B by C and precipitates of Mg_2Si) is the reason for the superior results from SiC doping. Slusky *et al.*[10] have shown that Al can aggressively react with MgB_2, and its substitution into the Mg position leads to a loss of superconductivity. It was found, however, that alumina (Al_2O_3) is more stable in terms of reaction with MgB_2 [11-13], and as a dopant, results in low field J_c enhancement due to improved grain connectivity. A few successful research efforts have been reported on co-doping [14-16] but the effects of simultaneous doping with nano-Al_2O_3 and SiC on the formation and superconductivity properties of the MgB_2 bulk and wires have not been reported, however, to the best of our knowledge. In the present work, to improve the in-field J_c performance, we study the effects of co-doping nano-Al_2O_3 and SiC into MgB_2 bulk

and wire on the microstructure, as well as the superconducting and electronic properties.

4.2 Experimental

Pure and six bulk samples of $Mg_{0.98}Al_{0.02}$ $(B_{1-x}C_x)_2$ were prepared by an *in-situ* process, where the values of *x* are 0, 0.01, 0.02, 0.03, 0.04 and 0.05. The constituent materials Mg, B, Al_2O_3, and SiC were mixed in a stoichiometric ratio. Finally, the mixed powder was pelletized under high pressure. Then three wires (undoped, single doped with 2 wt% SiC, and co-doped with 2 wt% Al_2O_3 + 1 wt% SiC) were fabricated and all samples were sintered at 670 °C for 2.5 h. The wire fabrication process with iron sheath for the different powders has been published elsewhere[7]. Microstructures, lattice parameters, magnetization and normal state resistivity, and transport critical currents were characterized by using a field emission gun-scanning electron microscope (FEG-SEM), X-ray diffractometer (XRD), vibrating sample magnetometer (VSM) attached to a 14 T physical properties measurement system (PPMS) and 14 T transport measurement system, respectively. A magnetic J_c was derived from the height of the magnetization loop ΔM using a Bean model: $J_c = 20\Delta M/[a(1-a/3b)]$. The lattice parameters were obtained by Rietveld refinement. Details of the sample compositions and measured superconducting properties of all the samples are given in **Table 4.1**.

4.3 Results and Discussions

The XRD spectra of pure MgB_2, MgB_2 mono doped with 2 wt% Al_2O_3 and co-doped with 2 wt% Al_2O_3 and SiC in different percentages are shown in **Figure 4.1(a)**, where it is clear that the pure and 2 wt% Al_2O_3 mono-doped samples contain no other impurity phase except for minor trace of MgO. With the addition of SiC, along with 2% Al_2O_3, an impurity phase $MgSiO_4$ appears, the peaks of which are marked by +. It is clear that the full-width-at-half- maximum (FWHM) of the (1 1 0) peak increases with increasing SiC doping level (**Table 4.1**). This indicates that small grains and imperfect crystallinity exist in the co-doped samples [17, 18]. These

observations can be further supported by the microstructures in Fig. 1b–d, where the grain size seems to be smaller, more compacted and homogeneous for the co-doped sample (**Figure 4.1(d)**) compared to un-doped (**Figure 4.1(b**)) and mono-doped samples (**Figure 4.1(c)**).

Table 4.1: Lattice parameters, FWHM values, ρ values at 40 K, and T_c for the bulk samples of $Mg_{0.98}Al_{0.02}(B_{1-x}SiC_x)_2$, with $_x$ varying from 0 to 5%.

Samples	a (Å)	c (Å)	FWHM (1 1 0)	$\rho_{40\,K}$ (μΩ/cm)	T_c (K)	J_c (Acm^{-2})	
						10 K, 2 T	25 K, 2 T
Un-doped MgB_2	3.087	3.532	0.45	28	37.38	0.436×10^5	1.024×10^3
$Mg_{0.98}Al_{0.02}(B_{1-0.00}C_{0.00})_2$	3.085	3.521	0.53	30	37.28	0.906×10^5	2.64×10^3
$Mg_{0.98}Al_{0.02}(B_{1-0.01}C_{0.01})_2$	3.085	3.529	0.55	54	36.48	1.043×10^5	12.98×10^3
$Mg_{0.98}Al_{0.02}(B_{1-0.02}C_{0.02})_2$	3.081	3.513	0.60	75	35.81	0.549×10^5	1.589×10^3
$Mg_{0.98}Al_{0.02}(B_{1-0.03}C_{0.03})_2$	3.077	3.525	0.65	90	35.23	0.605×10^5	1.948×10^3
$Mg_{0.98}Al_{0.02}(B_{1-0.04}C_{0.04})_2$	3.071	3.511	0.72	108	34.54	0.532×10^5	0.956×10^3
$Mg_{0.98}Al_{0.02}(B_{1-0.05}C_{0.05})_2$	3.065	3.539	0.77	122	34.25	0.469×10^5	0.835×10^3

From **Table 4.1**, it is found that the *a*-axis lattice parameter decreases faster than the *c*-axis one with the increasing addition of SiC. This clearly indicates the substitution of C on B sites in the *ab*- plane. However, the *c*-axis only slightly modulated with the addition of Al_2O_3. It is also clear from **Table 4.1** that co-doping with SiC and Al_2O_3 also reduces the transition temperature (T_c) more than in the undoped and alumina only doped MgB_2. This is expected due to the C substitution at the B sites. Since no C substitution takes place in only Al_2O_3 doped sample, the *a*-axis parameter and T_c reduction may be due to the lattice strains caused by the nanometer-sized Al_2O_3 inclusions in the MgB_2[19]. This observation can also be supported by the resistivity, ρ, values for the undoped MgB_2, MgB_2 + 2 wt% Al_2O_3 and MgB_2 + 2 wt% Al_2O_3 + (1–5) wt% SiC samples, which were 28, 30 and 54–122 mΩcm at 40 K, respectively, as shown in **Table 4.1**. The increased ρ and the reduction of *a*-axis and T_c for the MgB_2 + 2 wt% Al_2O_3 + (0.5–5) wt% SiC samples also indicate increased impurity scattering as a result of C substitution onto B sites.

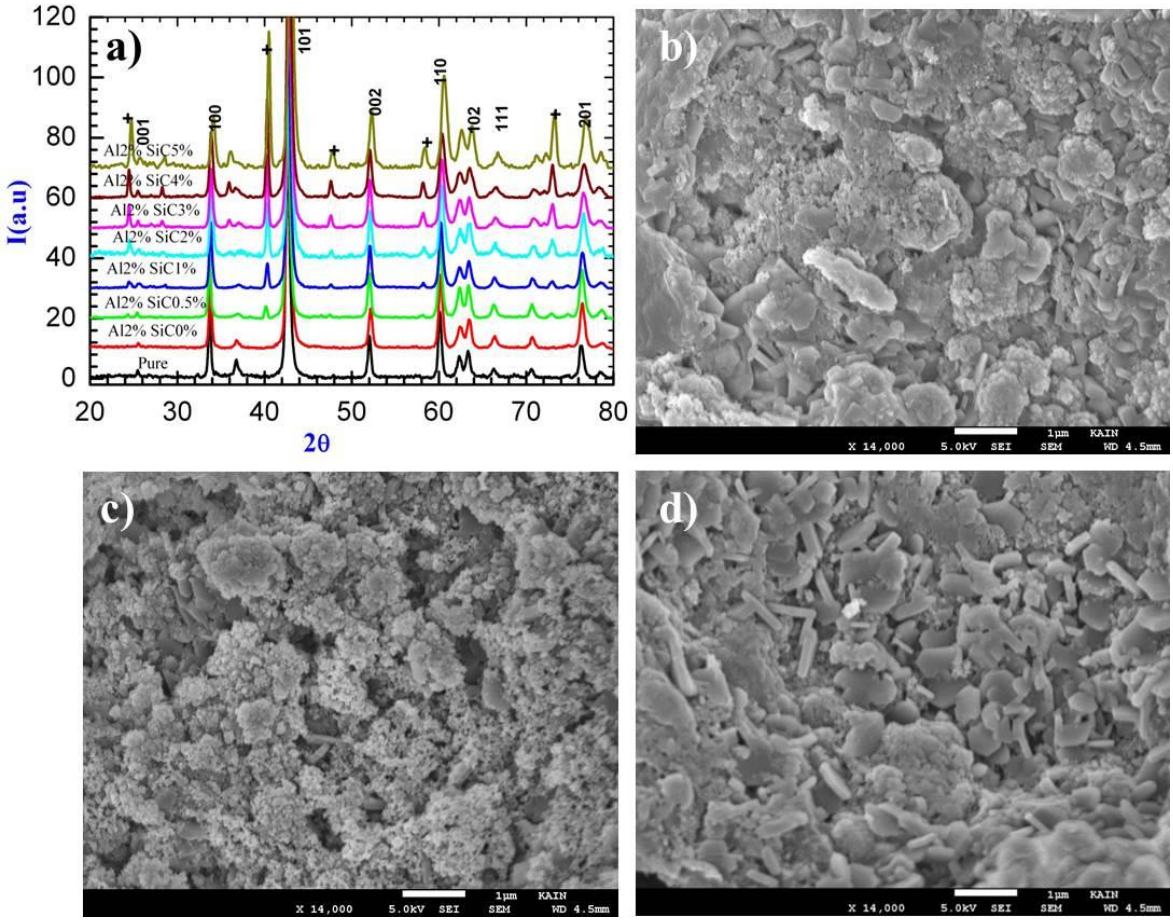

Figure 4.1 (a) XRD of $Mg_{0.98}Al_{0.02}(B_{1-x}SiC_x)_2$, with x varying from 0 to 5%. SEM images for (b) pure MgB_2 and MgB_2 with (c) 2 wt% Al_2O_3 and (d) 2 wt% Al_2O_3+1 wt% SiC.

The variation of magnetic J_c of the bulk samples at 10 K and 25 K with magnetic field (B) is plotted in **Figure 4.2(a and b)**, respectively. The samples with SiC doping show great improvement, especially in the high field region, compared to the un-doped and alumina only doping samples. The co-doped sample with the composition of 2 wt% Al_2O_3 + 1 wt% SiC shows the best in-field J_c (B) performance at both 10 K and 25 K (Table 4.1). **Figure 4.3** shows the transport J_c vs B for the pure, SiC mono-doped and co-doped MgB_2 wires at 4.2 K and 20 K. The design and morphology of the MgB_2/Fe wire filament has been displayed in the inset.

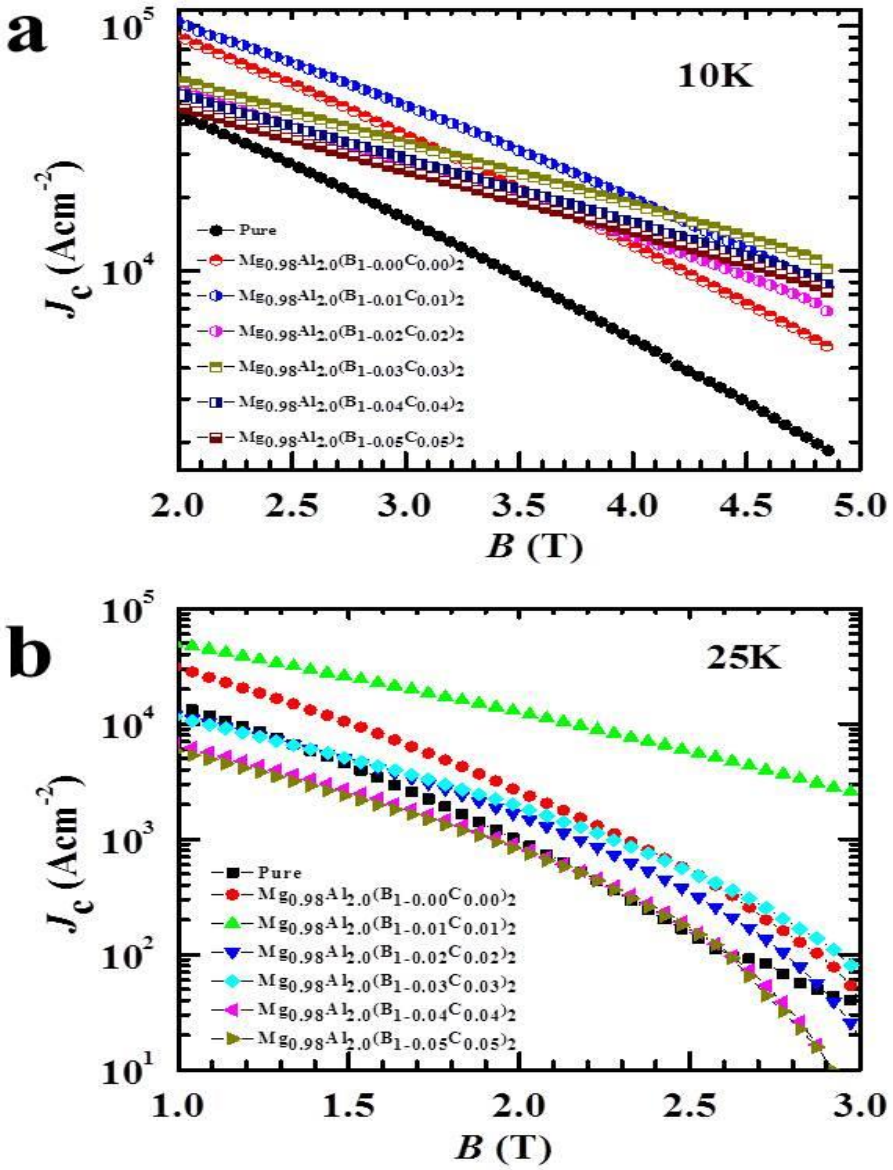

Figure 4.2 Magnetic J_c vs B for Al_2O_3 and SiC co-doped MgB_2 bulk samples at (a) 10 K and (b) 25 K.

It seems that co-doping causes a possible J_c crossover at 7 T with SiC mono-doping at 4.2 K. A steeper slope of J_c-B is observed in co-doped MgB_2 wire compared to the mono-doped wire. The value of $B(10^4)$ [the field at which $J_c = 10^4$ Acm^{-2}] was enhanced from 7.6 to 9.8 T in the co-doped wire compared to the pure wire due to improved grain connectivity, smaller grain size, and C-substitution, as evidenced by the ρ, FWHM, T_c, and a-axis lattice parameter, respectively.

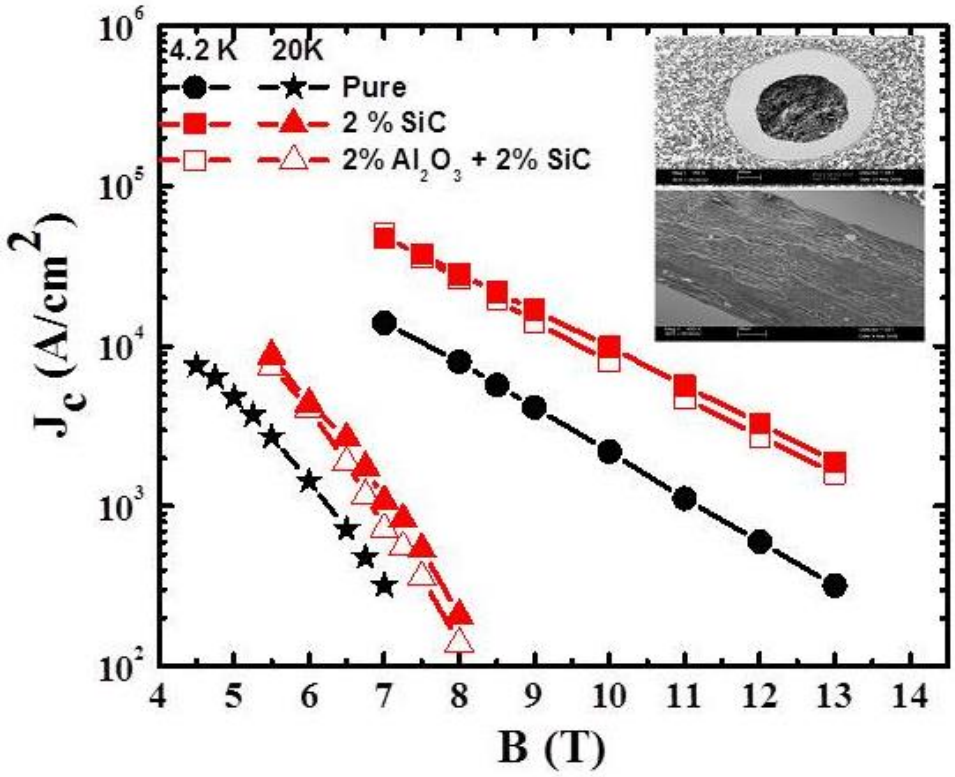

Figure 4. 3 Transport J_c vs B for Al_2O_3 and SiC co-doped MgB_2 wire samples at 4.2 K and 20 K. Transverse- and cross-sectional views of the un-doped wire are shown in the inset.

4.4 Conclusion

We have successfully synthesized pure and nano-Al_2O_3 + SiC co-doped MgB_2 polycrystalline bulks and wires. A systematic decrease in *a*-axis lattice parameter and T_c in co-doped samples with increasing SiC doping level was observed. The co-doped sample with the composition of 2 wt% Al_2O_3 + 1 wt% SiC in both bulk and wire form shows the best in-field J_c (B) performance at operating temperatures ranging from 4.2 K to 25 K due to the carbon substitution and better grain connectivity. This result is very interesting from the view point of low-field magnet applications.

4.5 References

1. J. H. Schultz, Applied Superconductivity, IEEE Transactions on **13** (2), 1604-1607 (2003).

2. P. Grant, Nature **411** (6837), 532-533 (2001).

3. S. X. Dou, S. Soltanian, J. Horvat, X. L. Wang, S. H. Zhou, M. Ionescu, H. K. Liu, P. Munroe and M. Tomsic, Appl Phys Lett **81** (18), 3419-3421 (2002).

4. S. X. Dou, W. K. Yeoh, J. Horvat and M. Ionescu, Appl Phys Lett **83** (24), 4996-4998 (2003).

5. W. K. Yeoh, J. H. Kim, J. Horvat, X. Xu, M. J. Qin, S. X. Dou, C. H. Jiang, T. Nakane, H. Kumakura and P. Munroe, Supercond Sci Tech **19** (6), 596-599 (2006).

6. J. H. Kim, S. Zhou, M. S. A. Hossain, A. V. Pan and S. X. Dou, Appl Phys Lett **89** (14), 142505 (2006).

7. M. S. A. Hossain, C. Senatore, R. Flukiger, M. A. Rindfleisch, M. J. Tomsic, J. H. Kim and S. X. Dou, Supercond Sci Tech **22** (9) (2009).

8. K. Vinod, R. G. A. Kumar and U. Syamaprasad, Supercond Sci Tech **20** (1), R1-R13 (2007).

9. S. X. Dou, O. Shcherbakova, W. K. Yeoh, J. H. Kim, S. Soltanian, X. L. Wang, C. Senatore, R. Flukiger, M. Dhalle, O. Husnjak and E. Babic, Phys Rev Lett **98** (9), 097002 (2007).

10. J. S. Slusky, N. Rogado, K. A. Regan, M. A. Hayward, P. Khalifah, T. He, K. Inumaru, S. M. Loureiro, M. K. Haas, H. W. Zandbergen and R. J. Cava, Nature **410** (6826), 343-345 (2001).

11. T. He, R. J. Cava and J. M. Rowell, Appl Phys Lett **80** (2), 291-293 (2002).

12. A. Delfany, X. L. Wang, S. Soltanian, J. Horvat, H. K. Liu and S. Dou, Ceramics International **30** (7), 1581-1583 (2004).

13. X. F. Rui, J. Chen, X. Chen, W. Guo and H. Zhang, Physica C: Superconductivity **412–414, Part 1** (0), 312-315 (2004).

14. R. Flukiger, P. Lezza, M. Cesaretti, C. Senatore and R. Gladyshevskii, Applied Superconductivity, IEEE Transactions on **17** (2), 2846-2849 (2007).

15. J. D. Moore, G. K. Perkins, W. Branford, K. A. Yates, A. D. Caplin, L. F. Cohen, S. K. Chen, N. A. Rutter and J. L. MacManus-Driscoll, Supercond Sci Tech **20** (9), S278-S281 (2007).

16. N. Novosel, S. Galic, D. Pajic, Z. Skoko, I. Loncarek, M. Mustapic, K. Zadro and E. Babic, Supercond Sci Tech **26** (10) (2013).

17. C. B. Eom, M. K. Lee, J. H. Choi, L. J. Belenky, X. Song, L. D. Cooley, M. T. Naus, S. Patnaik, J. Jiang, M. Rikel, A. Polyanskii, A. Gurevich, X. Y. Cai, S. D. Bu, S. E. Babcock, E. E. Hellstrom, D. C. Larbalestier, N. Rogado, K. A. Regan, M. A. Hayward, T. He, J. S. Slusky, K. Inumaru, M. K. Haas and R. J. Cava, Nature **411** (6837), 558-560 (2001).

18. A. Yamamoto, J. Shimoyama, S. Ueda, Y. Katsura, I. Iwayama, S. Horii and K. Kishio, Appl Phys Lett **86** (21), 212502 (2005).

19. A. Serquis, Y. T. Zhu, E. J. Peterson, J. Y. Coulter, D. E. Peterson and F. M. Mueller, Appl Phys Lett **79** (26), 4399-4401 (2001).

CHAPTER 5: SUPERIOR CRITICAL CURRENT DENSITY OBTAINED IN MgB_2 BULKS THROUGH LOW-COST CARBON ENCAPSULATED BORON POWDER

5.1 Introduction

Compared to other superconductors, MgB_2 has fascinating advantages, such as its simple crystal structure, large coherence length, low material cost, and small anisotropy[1-3]. These properties make MgB_2 competitive with high temperature superconductors (HTS). In addition, the soaring price of helium is a serious threat to other low temperature superconductors (LTS). Recently, MgB_2 superconductor was shown to have significant potential for industrial applications, such as magnetic resonance imaging (MRI), maglev trains, wind turbines, Josephson devices, fault-current limiters, etc. In spite of its numerous advantages, existing MgB_2 materials still have some drawbacks under magnetic field. To overcome this, extensive research has been carried out to increase in-field performance of MgB_2 in the past decade with a view toward practical application. Carbon is well-known to be a promising dopant that can accelerate the enhancement of high field performance. It is thus necessary to optimize an industrial scalable approach of carbon doping for MgB_2 material.

Various approaches have been adopted previously by many research groups to introduce carbon into MgB_2 lattice structure, and among those methods, the most popular techniques are solid state mixing[4] and the chemical solution route[5]. In the case of solid state mixing[4], nano-size precursors, such as SiC and C, are used, but usually nano-size precursor powders tend to be agglomerated during the mixing process. In addition, inhomogeneous mixing between precursors makes MgB_2 undergo complicated reaction or leads to unexpected impurity phases. Alternatively, the chemical solution route has been suggested, and the effect of carbohydrate, i.e., malic acid, introduced in this way on the MgB_2 superconducting material have been evaluated, demonstrating that this is one of the most successful techniques reported so far[5-7].

In this case, homogeneity of the carbon cannot be achieved up to the desired level. This is because there is no definitive control during this process due to the high volatility of the liquid hydrocarbon. Recently, Susner *et al.*[8] investigated and reported a more efficient carbon-doping method, with the product called pre-carbon doped boron, resulting in enhancement of the irreversibility field (B_{irr}) and the upper critical field (B_{c2}) when it was used in MgB_2 superconductor. In their method, they used boron that was amorphous, but with some monocrystalline nature, synthesized by the radio frequency (RF) plasma method[9, 10]. In this process, however, residual BCl_3 adsorbed on the powder particles can react with the humidity in air[11], which is detrimental to the performance of the superconductor.

In order to overcome these problems, we fabricated and studied carbon encapsulated boron powder in collaboration with Pavezyum Kimya, Turkey. We produced amorphous boron powder through pyrolysis of diborane gas (B_2H_6) under inert conditions, and the corresponding schematic illustration of the whole process is presented in **Figure 5.1(a)**. In the B_2H_6 production method, there is always hydrogen gas present in the gas stream, which enables a reducing atmosphere and protection against oxidation. At the same time, it can enhance the thermal conductivity during the pyrolysis. Carbon addition is established by the simultaneous decomposition or pyrolysis of gaseous hydrocarbon (C_xH_y) in the furnace with the B_2H_6. Hydrocarbon as carbon dopant is simply injected into the gas stream of B_2H_6 and hydrogen. Finally, freshly formed spherical-shaped boron particles are obtained, encapsulated with active thin carbon layers (see **Figure 5.1(b)**). What is important thing is that this approach offers further direction for the scalable production of cost-effective and suitable boron powder for industrial use in MgB_2 applications.

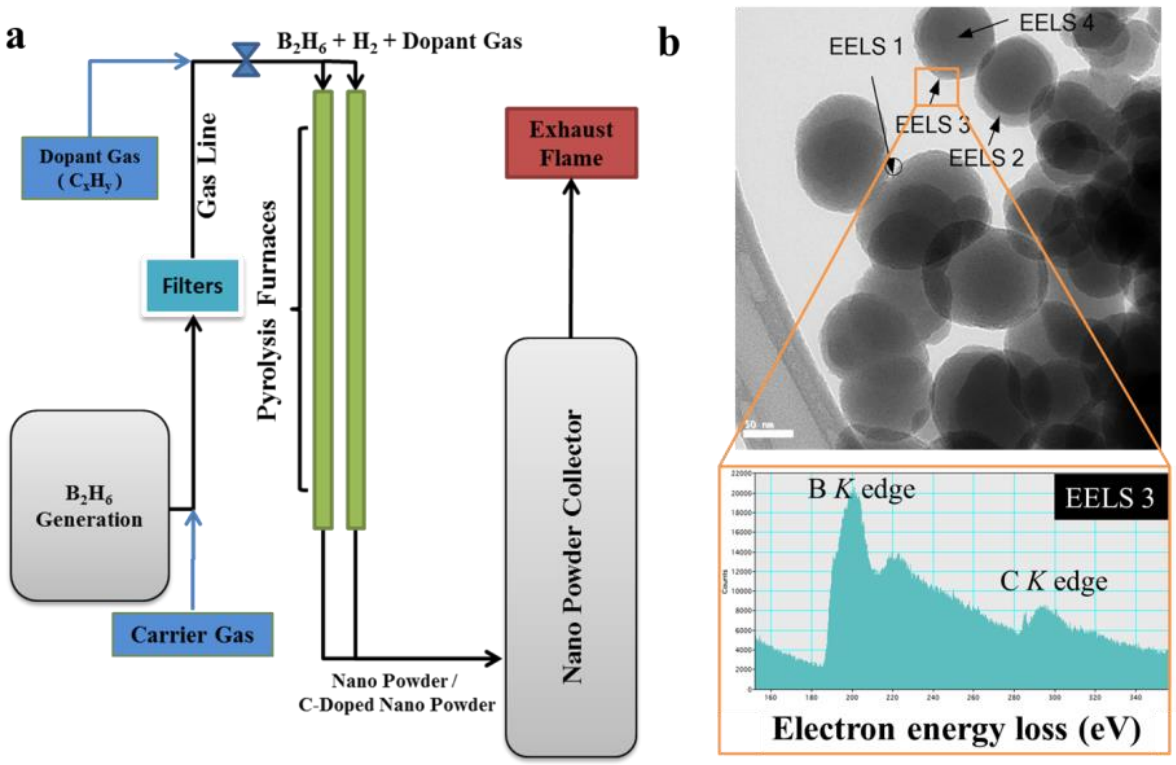

Figure 5.1 (a) Schematic diagram of carbon encapsulation process; **(b)** EELS spot analysis indicates high carbon concentrations at the edges of particles (80 keV).

5.2 Experimental Procedure

MgB_2 bulks were prepared using commercially available magnesium (Mg, 99.9%, 325 mesh) and *in-house* amorphous boron (B, 98.8%) powders with the composition of Mg : B = 1 : 2. To investigate the performance of carbon encapsulated boron power (98.8%), four samples were prepared and denoted as PVZ-NB 23, PVZ-NB 34, and PVZ-NB 41, respectively, with different carbon amount. Undoped MgB_2 bulks were also made for comparative study. Using a carbon analyzer (LECO company) the carbon percentages for PVZ-NB 23, PVZ-NB 34, and PVZ-NB 41 were estimated to be 2.3 wt.%, 3.44 wt.% and 4.14 wt.%, respectively. The powders were pressed into 13.0 mm pellets 1.0 mm in thickness by applying uniaxial pressure using 10 ton hydraulic press. Each pressed pellet was then sealed in an iron tube and sintered at 700 ˚C for 30 min in a tube furnace under high purity argon gas (99.99%) atmosphere. To investigate the microstructure and phase constitution, X-ray diffraction (XRD) analysis was performed on a GBC MMA X-ray diffractometer using Cu-Kα radiation. Electron energy loss

spectroscopy (EELS; JEOL ARM-200F) analysis was carried out for detecting carbon. The morphology of the bulk samples was observed by scanning electron microscopy (SEM) on a JEOL JSM-7500FA. The magnetic hysteresis loops, critical temperature (T_c), and resistivity (ρ) of the samples were measured with a physical properties measurement system (PPMS, Quantum Design). For comparison, all the samples were kept at the same size. The critical current density (J_c) was calculated from the Bean approximation model.

5.3 Results and Discussions

Figure 5.2 shows the XRD patterns of bulks sintered at 700°C for 30 minutes. Diffraction analysis was carried out using Rietveld refinement. We found that MgB_2 is well developed with a minor amount of MgO impurity, regardless of a sintering temperature. **Figure 2(b and c)** shows enlarged views of selected regions of the XRD patterns to reveal the details of the MgB_2 (110) and (002) peaks, respectively. It is clear that the (110) peak of the carbon-doped samples is shifted towards higher angle compared to the undoped MgB_2. On the other hand, the (002) peak position remains unchanged in all the samples. This indicates that carbon partially substitutes for boron in the lattice in the MgB_2 crystal structure. The lattice parameters were further determined by Rietveld refinement using FullProf software. The *a*- and *c*-lattice parameters are presented in Table I. We found that the *a*-axis lattice parameter of the carbon-doped samples is smaller than that of the undoped MgB_2 (from 3.086 Å to 3.072 Å). Avdeev *et al.*[12] proposed a method to estimate the actual level of carbon substitution x in $Mg(B_{1-x}C_x)_2$, and according to this technique, $x = 7.5 \times \Delta(c/a)$, where $\Delta(c/a)$ is the change in c/a compared to an undoped sample. The actual carbon contents for the PVZ-NB 41, PVZ-NB 34, and PVZ-NB 23 samples in terms of x in $Mg\ (B_{1-x}C_x)_2$ are estimated to be 0.0232, 0.0266, and 0.0307, respectively.

Table 5.1 Crystallographic data from Rietveld analysis, the resistivity at 40 K and 300 K and

irreversibility field (B_{irr}) for un-doped and carbon-encapsulated MgB_2 samples.

Samples	*a* (Å)	*c* (Å)	*c* / *a*	Actual C(*x*) In $MgB_{2-x}C_x$	FWHM of peak 101 (°)	FWHM of peak 110 (°)	T_c (K)	$\rho_{300\ K}$ (μΩcm)	$\rho_{40\ K}$ (μΩcm)	B_{irr}* (T)
Undoped MgB_2	3.086	3.522	1.1410	0.0000	0.508	0.586	37.32	56.4	27.30	5.70
PVZ-NB 41	3.079	3.523	1.1442	0.0232	0.588	0.774	35.33	67.52	42.17	6.60
PVZ-NB 34	3.079	3.524	1.1445	0.0266	0.600	0.825	34.85	66.65	43.28	6.25
PVZ-NB 23	3.072	3.518	1.1451	0.0307	0.610	1.320	35.92	90.28	54.29	6.10

B_{irr}* was calculated from the standard criterion of critical current density (100 Acm^{-2})

Figure 5.3 presents SEM images of the top-view surfaces of the undoped and carbon-doped samples. As was previously reported[13], the morphology of carbon-doped samples is changed from that of the corresponding undoped materials and is more compacted with more homogeneous particles due to the carbon encapsulation. The grain size is also smaller in the carbon-doped samples compared to the undoped sample, which increases grain boundary pinning. The grain refinement of the carbon-encapsulated sample is further supported by the full-width-at-half-maximum (FWHM) of (101) and (110) peaks in the XRD patterns as shown in Table.1. The FWHM values of the (101) and (110) peaks for the doped MgB_2 samples become broadened with increasing carbon content. According to Scherrer's formula (D_p = 0.94λ / $\beta_{1/2}$ cosθ, where D_p is crystal size, λ is wavelength, $\beta_{1/2}$ is FWHM, and θ is peak position), the FWHM value is inversely proportional to grain size. Therefore, this broadening of the FWHM value could indicate a refinement of the grain size due to a carbon substitution that minimizes grain growth, which results in an enhancement of the grain boundary pinning effect. This can be also explained by the reduction of T_c. Table I also present the measured resistivity (ρ) values, and it was observed that ρ at 40 K increases from 27.30 μΩcm in the undoped sample to 54.29 μΩcm in the PVZ-NB 23 doped sample. This increased resistivity is due to the impurity scattering in MgB_2 lattice[14].

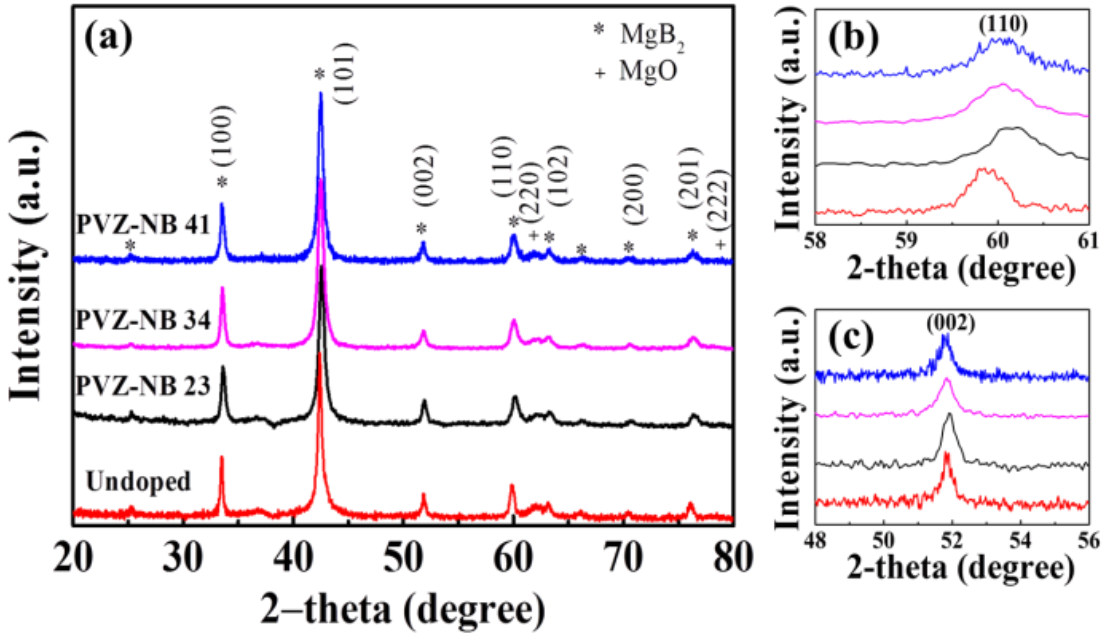

Figure 5.2 X-ray diffraction pattern of (a) undoped and carbon-doped MgB_2 samples, and enlarged view of (b) the (110) peak and (c) the (002) peak. All the samples were sintered at 700 ˚C for 30 minutes.

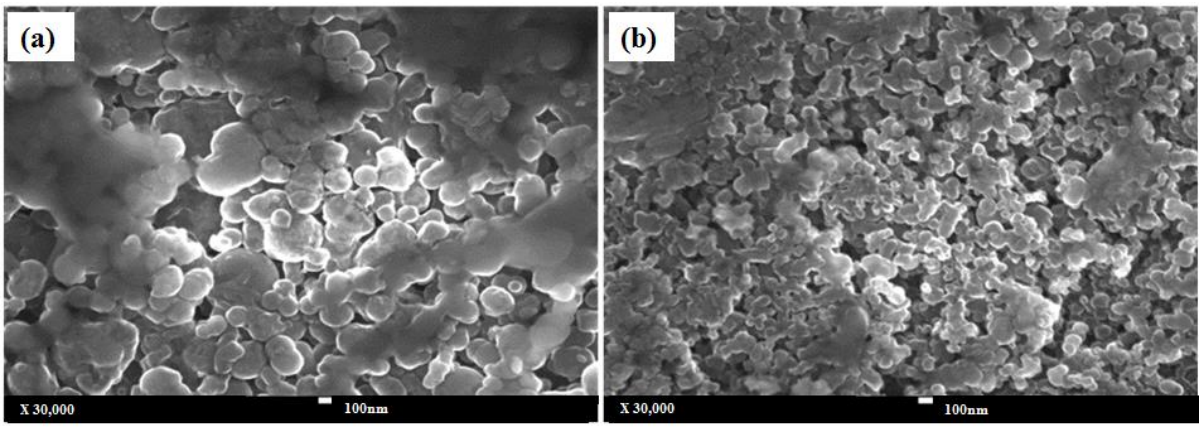

Figure 5.3 SEM images of (a) undoped and (b) C-encapsulated MgB_2 bulk samples sintered at 700 ˚C for 30 minutes.

Figure 5.4(a and b) shows the magnetic field dependence of J_c of the undoped and carbon-doped MgB_2 bulk samples. For comparative study, the results for undoped and carbon doped MgB_2 samples fabricated from different boron sources are plotted in **Figure 5.4(b)**. **Figure 5.4(a)** shows that, at 9 T and 5 K, the J_c values for all carbon-doped samples are over 10^4 Acm^{-2}, more than six times higher than the values for the undoped MgB_2 sample. The best sample

in our experiment (PVZ-NB 34) was chosen for comparison in **Figure 5.4(b)**. It reveals that the magnetic J_c of PVZ-NB 34 exceeds that of the malic doped sample which produced through chemical solution route[15]. This could be attributed to the pre-carbon encapsulation method.

Grain boundary pinning may also play a role, because it is usually important in the high field region, as seen in undoped MgB_2. In addition, the normalized temperature dependence of B_{c2} for all the present samples is shown in the inset of **Figure 5.4(a)**. Significant enhancement of B_{c2} was observed for the carbon-encapsulated MgB_2 samples, indicating that carbon substitution in boron sites results in an enhancement in B_{c2}. The slope of the B_{c2} as functions of normalized temperature for the carbon-doped samples is much steeper than for the undoped sample. This is related to the intra-band and inter-band scattering due to carbon substitution[4, 5]. The irreversibility field (B_{irr}) in Table I was determined using an extrapolation of J_c versus B to 100 A cm^{-2} at 20 K. A common feature observed in carbon doped MgB_2 samples (Table I) is the enhancement of B_{irr}. This observation can be explained by the fact that the enhancement of the electrical resistivity at 40 K as a consequence of the disorder introduced by the carbon substitution on the boron sites.

The small grain size and the grain boundary density (see **Figure 5.3**) in carbon-doped MgB_2 samples may contribute to the flux pinning. To obtain a clear concept of the pinning mechanism in the carbon-encapsulated samples, the normalized pinning force density, $f = F/F_{max}$ is plotted against $h = B/B_{peak}$ in **Figure 5.4(c)**, where B_{peak} is the magnetic field at the maximum pinning force. The scaling of *f-h* is analyzed through the formulation of Higuchi *et al.*[16] in terms of normal point pinning, $f(h) = (9/4)h(1-h/3)^2$, and correlated pinning, $f(h) = (25/16)h^{0.5}(1-h/5)^2$. From the experimental data, it is evident that at normalized magnetic field higher than B_{peak}, flux pinning is dominated by the correlated pinning for the carbon-encapsulated samples, whereas point pinning is dominant for undoped samples. That is why flux pinning is determined

by both point pinning and surface pinning[15]. The experimental results are in good agreement that the grain sizes in the carbon-doped samples are much smaller than in the undoped samples sintered at 700 ˚C for 30 minutes.

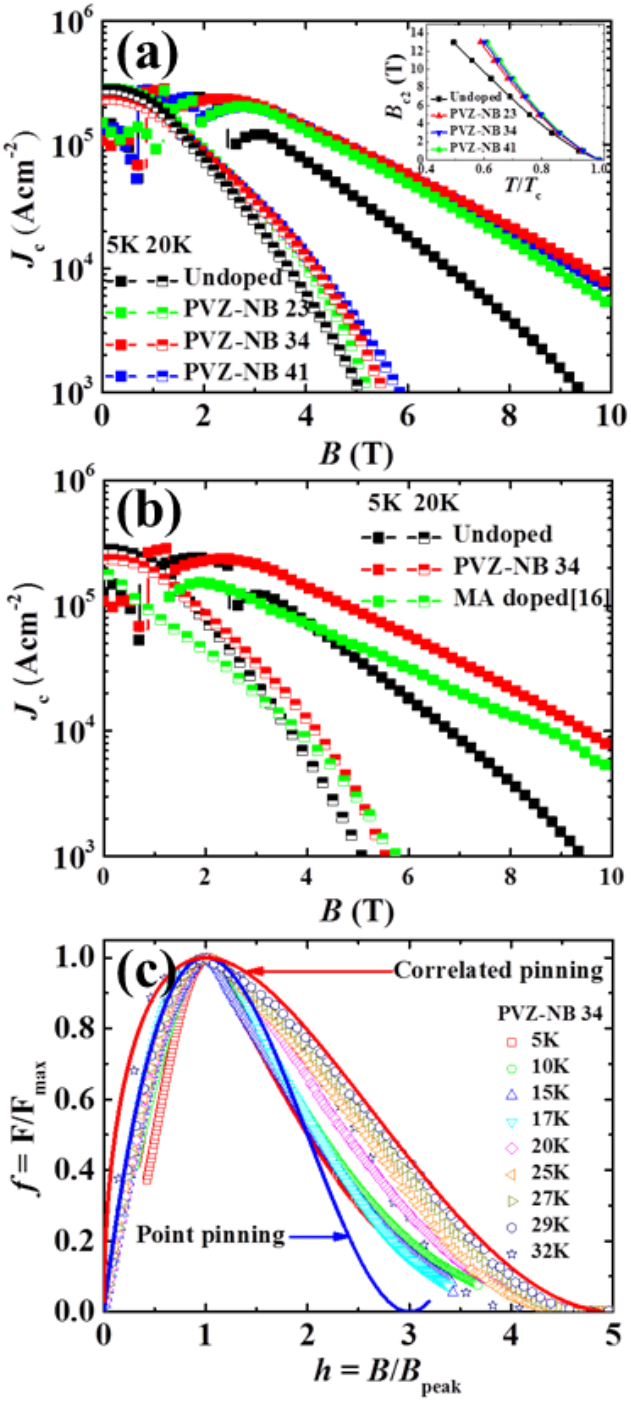

Figure 5.4 Magnetic field dependence of critical current density (J_c) at 5 K and 20 K (a) for the un-doped and the carbon-doped MgB_2 samples, and (b) for different bulk MgB_2 samples from the literature compared with the best carbon-doped MgB_2 sample (PVZ-NB) (c) The

normalized pinning force density, $f = F/F_{max}$ is plotted against $h = B/B_{peak}$ for PVZ-NB 34 sample. The inset of (a) shows B_{c2} against the normalized temperature T/T_c for the present un-doped and carbon-doped MgB_2 samples.

5.4 Conclusion

In summary, boron powders pre-encapsulated with different carbon contents were used to fabricate MgB_2 bulks. These bulks show enhanced magnetic J_c, with the highest value of 10^4 Acm^{-2} at 9.47 T, 5 K. The reason behind the improved high field J_c and pinning force is that the enhanced grain boundary pinning and homogeneous carbon distribution in the carbon-doped samples increase the Mg and B reactivity, and at the same time, restrict the grain growth of the reacted MgB_2. These results indicate that carbon-encapsulated amorphous boron could be a promising alternative for industrial production of practical MgB_2 bulks or wires with excellent J_c, as large-scale production can be commercially viable in terms of cost-effectiveness.

5.5 References

1. C. Buzea and T. Yamashita, Supercond Sci Tech **14** (11), R115-R146 (2001).

2. J. Nagamatsu, N. Nakagawa, T. Muranaka, Y. Zenitani and J. Akimitsu, Nature **410** (6824), 63-64 (2001).

3. Z. Q. Ma and Y. C. Liu, International Materials Reviews **56** (5-6), 267-286 (2011).

4. S. X. Dou, O. Shcherbakova, W. K. Yeoh, J. H. Kim, S. Soltanian, X. L. Wang, C. Senatore, R. Flukiger, M. Dhalle, O. Husnjak and E. Babic, Physical Review Letters **98** (13), 139902 (2007).

5. J. H. Kim, S. Zhou, M. S. A. Hossain, A. V. Pan and S. X. Dou, Appl Phys Lett **89** (14), 142505 (2006).

6. M. S. A. Hossain, C. Senatore, R. Flukiger, M. A. Rindfleisch, M. J. Tomsic, J. H. Kim and S. X. Dou, Supercond Sci Tech **22** (9), 095004 (2009).

7. J. H. Kim, S. X. Dou, S. Oh, M. Jercinovic, E. Babic, T. Nakane and H. Kumakura, J Appl Phys **104** (6), 063911 (2008).

8. M. A. Susner, Y. Yang, M. D. Sumption, E. W. Collings, M. A. Rindfleisch, M. J. Tomsic and J. V. Marzik, Supercond Sci Tech **24** (1), 012001 (2011).

9. J. V. Marzik, R. C. Lewis, M. R. Nickles, D. K. Finnemore, J. Yue, M. Tomsic, M.

Rindfleisch and M. D. Sumption, AIP Conference Proceedings **1219** (1), 295-301 (2010).

10. J. V. Marzik, R. J. Suplinskas, R. H. T. Wilke, P. C. Canfield, D. K. Finnemore, M. Rindfleisch, J. Margolies and S. T. Hannahs, Physica C: Superconductivity and its Applications **423** (3-4), 83-88 (2005).

11. S. J. Ye, M. H. Song, A. Matsumoto, K. Togano, M. Takeguchi, T. Ohmura and H. Kumakura, Supercond Sci Tech **26** (12), 125003 (2013).

12. M. Avdeev, J. D. Jorgensen, R. A. Ribeiro, S. L. Bud'ko and P. C. Canfield, Physica C: Superconductivity and its Applications **387** (3-4), 301-306 (2003).

13. J. H. Kim, S. Oh, Y. U. Heo, S. Hata, H. Kumakura, A. Matsumoto, M. Mitsuhara, S. Choi, Y. Shimada, M. Maeda, J. L. MacManus-Driscoll and S. X. Dou, Npg Asia Mater **4**, E3 (2012).

14. J. Kim and S. Choi, J Anal Sci Technol **6** (1), 1-5 (2015).

15. A. Motaman, M. S. A. Hossain, X. Xu, K. W. See, K. C. Chung and S. X. Dou, Supercond Sci Tech **26** (8), 085013 (2013).

16. T. Higuchi, S. I. Yoo and M. Murakami, Physical Review B - Condensed Matter and Materials Physics **59** (2), 1514-1527 (1999).

CHAPTER 6: SYNERGETIC COMBINATION OF LIMD WITH CHPD FOR THE PRODUCTION OF ECONOMICAL AND HIGH PERFORMANCE MgB_2 WIRES

6.1 Introduction

From the perspective of practical applications, the preparation methods of MgB_2 wires play a very significant role in obtaining good performance. The *in-situ* fabrication method has been used successfully to make MgB_2 wires and tapes. In most cases, to make the MgB_2 conductor, both high purity amorphous or crystalline boron (B) powders along with small size Mg are used[1-4]. The cost of the precursor materials need to be taken into serious consideration for practical application, as the materials cost will be significantly high if the expensive high quality precursors are used. This cost problem could be solved significantly by using inexpensive low grade precursors. The price of high purity (99%) amorphous B powder is about ten times more expensive than low purity (96%) crystalline B powders. Contrarily, low purity materials need to be tested to find out conductor performance if they can be used to supplant existing precursors without much dropping in the superconducting properties. Recently, Kim et al. reported a very cost effective fabrication method by tailoring the starting material for inexpensive high performance MgB_2 wire[5]. It was revealed that using carbon (C)-encapsulated crystalline boron powder and coarse Mg as precursors improved the MgB_2 wire performance by controlling the shape and direction of the voids. Though, grain connectivity is still affected by the presence of elongated voids. So far, in the *in-situ* processing technique, the low density of the filament cores has been a serious hurdle in obtaining high critical current density (J_c) values in MgB_2 wires. In addition, volume contraction during the reaction from Mg and B to form MgB_2 limits the final density to about 50% of the theoretical density (2.36 gcm^{-3}). Due to the presence of high porosity in reacted MgB_2, the grain connectivity is significantly hampered in the finished wires. The typical effective superconductor area in the MgB_2 wire is only about 10%[6, 7]. In recent times, cold high pressure densification (CHPD) has been proposed as an

alternative way to enhance mass density and grain connectivity[8, 9]. Hossain *et al.* reported that the J_c value at 4.2 K and 10 T to be increased to around 40000 Acm^{-2} for a malic acid doped square conductor produced using CHPD[9]. In 2009, the superconductivity group of the University of Geneva first successfully applied CHPD to MgB_2 conductor in a short-length (<1 m)[8]. The density was increased to 73% of the theoretical value for the CHPD treated wire after heat treatment. The J_c increase was particularly remarkable at 20 K, which is more than 300%. Another very effective densification technique is known as the infiltration method, first reported by Giunchi *et al.,* in which the MgB_2 wire was fabricated using a composite billet composed of a steel pipe internally lined with an Nb tube filled with a coaxial internal pure Mg rod and B powder[10]. The J_c performance from the reported work was not outstanding, however, as there was no chemical doping associated with the technique. Following this work, an internal Mg diffusion (IMD) process using a pure Mg rod as a core surrounded by B powder and SiC additive was developed. The composite was cold worked into a wire and heat-treated at temperatures above the melting point of Mg (650 °C). During the heat treatment, liquid Mg infiltrated into the B layer and reacted to form MgB_2 phase. The best J_c for this IMD SiC doped MgB_2 wire was 100000 Acm^{-2} at 8 T, exceeding the performance of commercial Nb-Ti wires and making it satisfactory for all technical applications[11]. However, there is a serious limitation for scaling-up the IMD method. In this process, the Mg infiltration into the B layer forms a hollow wire with only a thin layer of Formula in the interior of the sheath tube. The total superconductor cross-sectional area is small. It is obvious that for this technique to be useful in large-scale production, an innovative process must be developed, and this is the process we propose in this work.

The main goal of this work is to develop a novel fabrication technique by combining the localized IMD process (LIMD) with CHPD and using large size Mg instead of Mg rod and cheap crystalline B powder for the manufacture of economical Formula superconductor wires

with electromagnetic performance suitable for industrial application.

6.2 Experimental Procedure

All wires were fabricated by the *in-situ* powder-in-tube (PIT) process. The starting Mg : B atomic ratio was chosen to be 1:2. Mg powders with different particle sizes of 325 mesh, 100 mesh, and 20–50 mesh were mixed with 97% crystalline boron supplied by Specialty Material Inc (SMI), USA. For comparison, two extra batches of wires were prepared from 325 mesh Mg/99% nanosize amorphous boron supplied by SB Boron USA and 325 mesh Mg/crystalline boron supplied by HC Starck, Germany. The compacted mixtures were inserted into Fe sheaths 9.5 mm in outer diameter and 5.5 mm in inner diameter. The Fe sheaths were cold-rolled into wires 3.5 mm in diameter using a two-axial grooved roller and inserted into Monel sheaths 6.0 mm in outer diameter and 3.5 mm in inner diameter. Afterwards, the composites were cold-rolled and drawn into wires 1.0 mm in diameter. The wires were then subjected to the CHPD process with the applied pressure of 1.5 GPa for core densification. All wires were sintered at 650 °C for 16 hours in a flowing argon gas environment. The transport critical currents of short pieces (6 cm) of straight wires were measured against magnetic field in the low temperature laboratories at the Karlsruhe Institute of Technology (KIT), Germany. Samples were immersed in a liquid helium bath and exposed to an external transverse magnetic field ranging from 2 up to 12 T. Current-voltage (*I-V*) characteristics were recorded by using a standard four-point measurement, where the potential taps were placed in the middle of the wire and spaced 2 cm from each other. The critical currents were estimated from the *I-V* curves using the criterion of 1 μVcm^{-1}. Grain morphology and microstructure were investigated by scanning electron microscopy (SEM).

6.3 Results and Discussions

Figure 6.1 gives a comparison of J_c with and without CHPD in MgB_2 monofilament wires

made from 325 mesh Mg and 99% purity amorphous (SB) or crystalline (SMI and Starck) B powders. The MgB_2 of wires made from amorphous boron typically shows better performance compared to those from crystalline boron powders, which is in good agreement with published results in the literature[4]. The value of J_c was surprisingly enhanced, however, in MgB_2 wire made from crystalline boron by applying CHPD. The J_c of CHPD treated wire made from crystalline boron is 3 times higher than typical values measured for the same wires, but without applying CHPD. This value was similar to the J_c value of wire made from expensive high purity nano-size amorphous boron (SB). This result was the motivation for the selection of crystalline boron in this work.

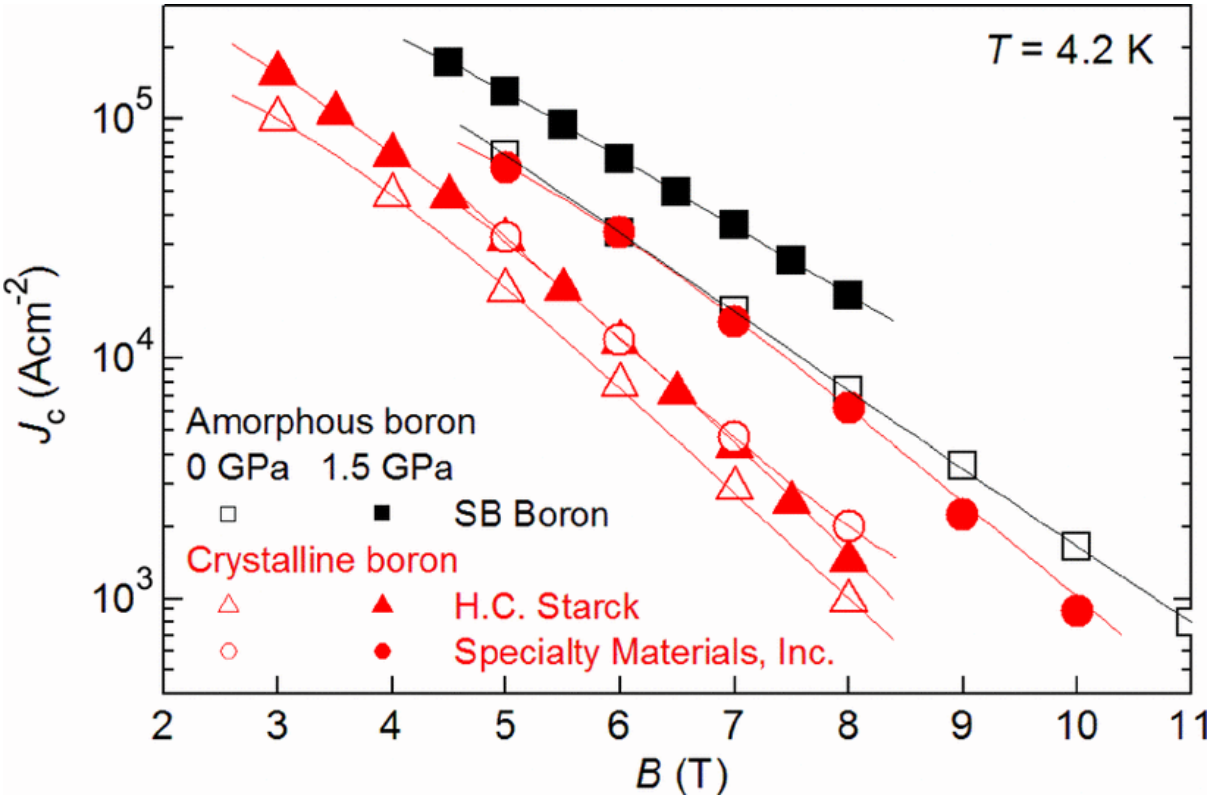

Figure 6.1 Transport critical current densities at 4.2 K as a function of magnetic field for binaryMgB_2/Fe/Monel wires fabricated from Mg powder with particle size of 325 mesh and various boron powders from SB Boron, H.C. Starck, and Specialty Materials, Inc. For comparison, the wires were also subjected to the CHPD process at 1.5 GPa.

In this study, we selected large size Mg following the concept proposed by Kim *et al.*[5], which

was in contrast to the internal magnesium diffusion (IMD) method reported by the National Institute of Materials Science (NIMS) group[11]. We used large size Mg particles (100 mesh, 20–50 mesh) rather than using a single Mg rod in the center of a metal sheath. By this technique, the Mg diffusion process was localized after long hours of heat treatment (600 °C/16 h) to allow a more uniform distribution of elongated voids generated during the cold working along the wire axis rather than a single big hollow, as is found in the typical IMD wires after reaction. Kim *et al.* demonstrated the validity of this concept[5]. Although the localized IMD process only uniformly distributes the voids and changes the voids to an elongated shape, it slightly improves the overall density.

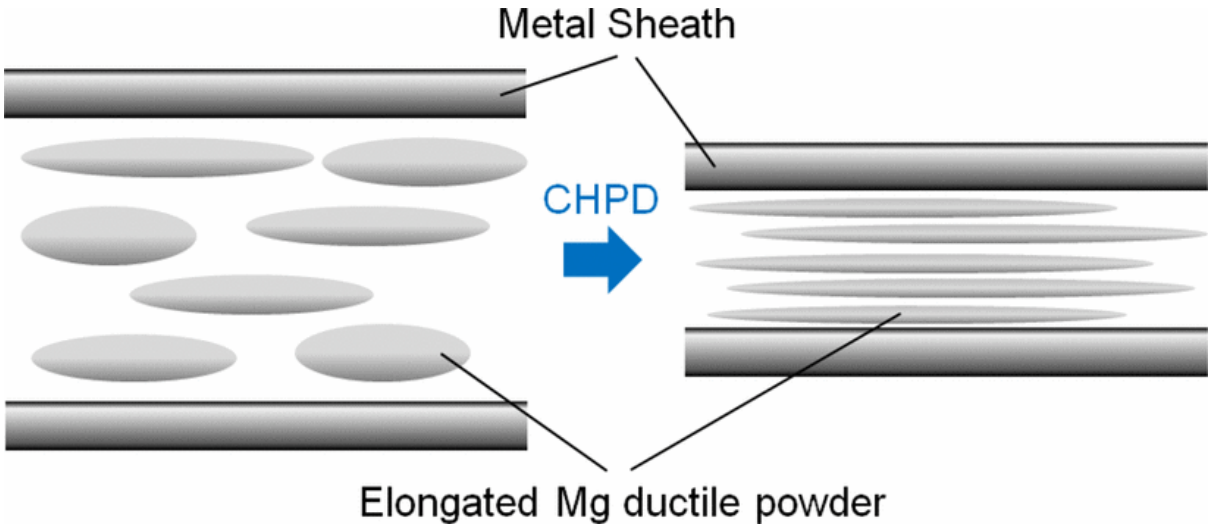

Figure 6.2 Schematic concept of MgB_2 wire fabrication using combined effects of CHPD and localized internal Mg diffusion from large-sized Mg particles.

Mg is ductile, and it can be stretched along the wire direction during the drawing process[12], resulting in a stringy and fibrous structure, to which is attributed the improved superconducting area fraction. If the size, shape and distribution of the voids can be correctly identified, then it will be easier to find a solution to avoid it completely. CHPD is one of the most successful solutions for improving the density of the filament. Although voids can be minimized by CHPD, they are not completely avoided. The shape and direction may be controlled and more

aligned, however, so that the MgB_2 grain linkage and area fraction can be improved. A schematic diagram of this mechanism is presented in **Figure 6.2.**

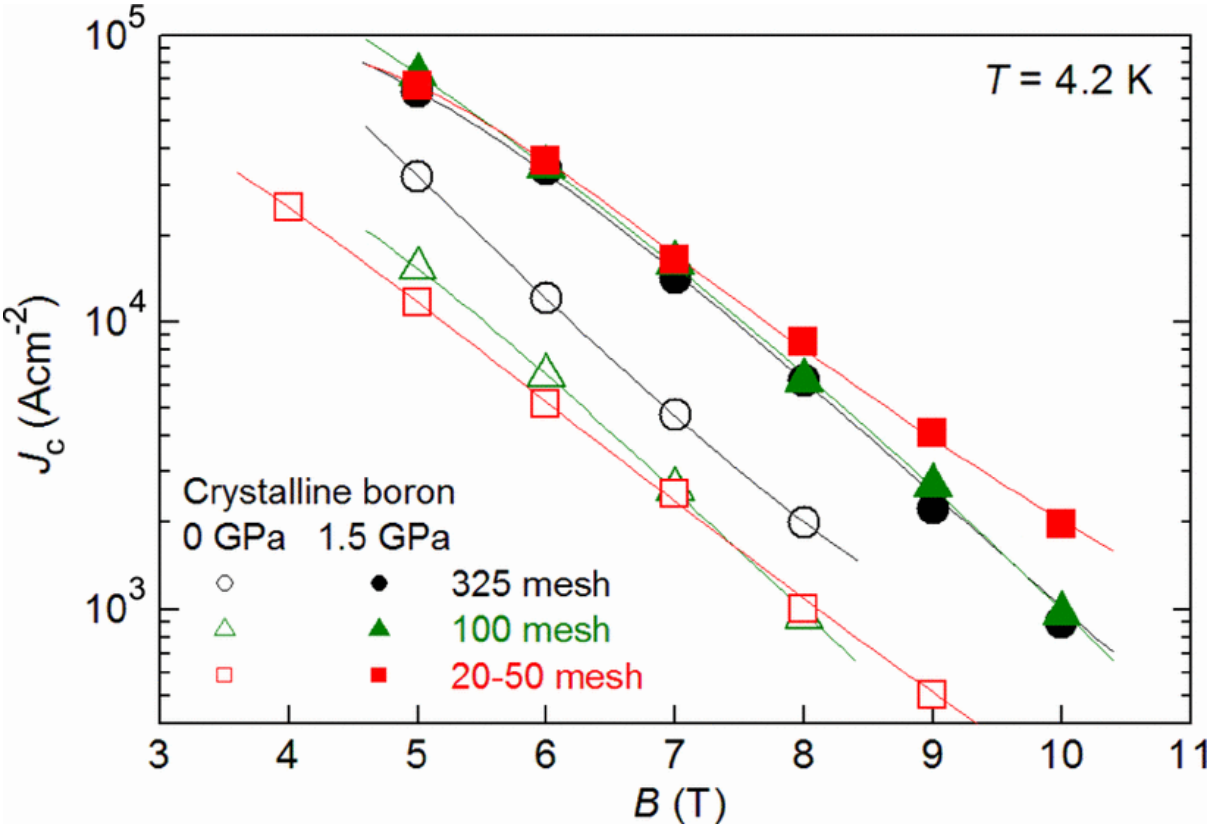

Figure 6.3 Transport critical current densities at 4.2 K as a function of magnetic field for binary MgB_2/Fe/Monel wires fabricated from Mg powders with different particle sizes of 325, 100, and 20–50 mesh, and crystalline boron powder from Specialty Materials, Inc. For comparison, the wires were also subjected to the CHPD process at 1.5 GPa.

Figure 6.3 shows the effect of CHPD on the transport J_c at 4.2 K in magnetic fields up to 12 T for binary wires fabricated from various sizes of Mg powders and crystalline boron, and sintered at 650 °C/16 h. Only data above 3 T are shown, because in the lower field region, J_c was too high to be measured due to the limitations of the current supply source and the lack of proper electrical stabilization. It was found from **Figure 6.3** that the binary wire made from the smaller size (325 mesh) Mg powder usually showed higher values of J_c than the samples made from relatively larger sizes of Mg powder (100 and 20–50 mesh), which was consistent with literature data[13], but surprisingly, this behavior was changed completely when CHPD was

applied.

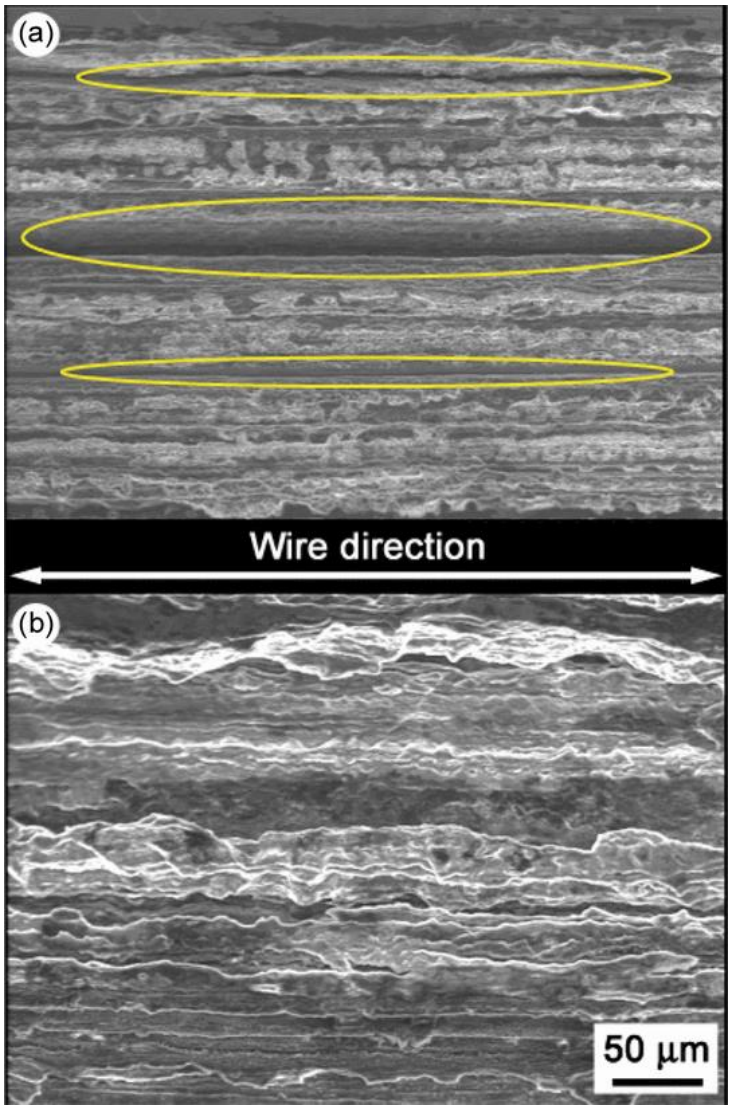

Figure 6.4 SEM images of cores of sintered wires prepared from Mg powder with the large particle size of 20–50 mesh (a) before and (b) after CHPD. The areas marked by the yellow ellipses in Fig. 3(a) indicate elongated voids along the wire direction, and some of these are eliminated by CHPD.

The J_c of wires fabricated from large size Mg (20–50 mesh) was significantly enhanced by applying CHPD due to the flat and elongated voids in the pressed region (see **Figure 6.2**), which might be attributed to the higher densification and hence, better connectivity in the filaments, as evidenced by the SEM images (see **Figure 6.4**). The aligned fibrous structure along the wire direction might also be the possible reason for the enhancement of the effective area fraction. Such grain alignment did not seem to be severely degraded inside the wire by

applying CHPD (1.5 GPa), and the boundaries between filaments may also act as strong pinning centers. This work is still ongoing, and there is plenty of room for further investigations of this interesting feature of void engineering in the MgB_2 filaments after the reaction heat treatment.

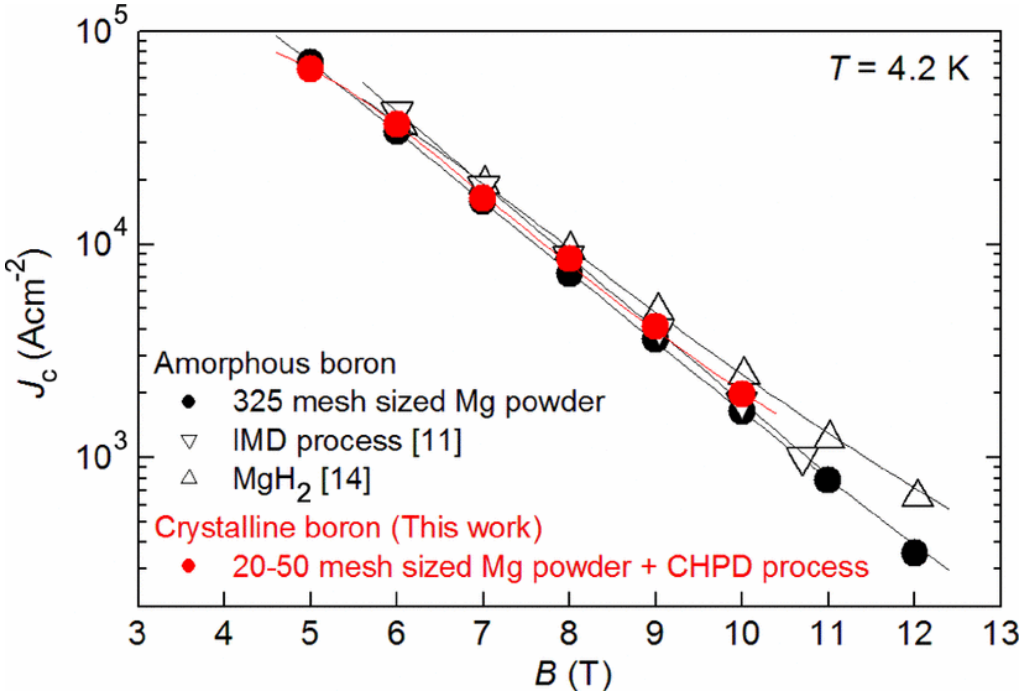

Figure 6.5 J_c versus B properties of binary wire using cheapest starting materials in this work compared with high-performance reported wires using expensive nano-size amorphous powder.

The critical current density as a function of magnetic field was compared in this study with the reported best performance binary PIT *in-situ* and IMD processed wires fabricated from expensive nano-size amorphous boron, small size Mg (325 mesh), MgH_2[14], and Mg rod. It is clear from **Figure 6.5** that the wire fabricated in this work from the cheapest starting materials treated with CHPD was well comparable in terms of performance with reported binary wires fabricated from expensive precursors. The performance of the densified wire made from cheap crystalline boron and large-size Mg shows similar J_c-B properties to wires using expensive nano-size materials. The critical current density of the wire in this work reaches $> 10^5$ at 4.2 K and 4 T, which is within the feasible range for application in low-field magnetic resonance

imaging (MRI) machines.

6.4 Conclusion

We have shown the most economical fabrication route and an alternate solution to the IMD method for the development of high performance, cost-effective MgB_2 wires for industrial application. The J_c of CHPD treated wires made from crystalline boron and large-size Mg shows the best performance among the other wires in this study. The possible reason for increased J_c may be the flat, directional, and elongated voids that arise after heat treatment from large size ductile Mg during the cold working process. The core is densified by the application of CHPD without any severe deterioration of the filament inside the wire. The most noticeable point in this study is that such a good quality binary conductor using cheaper crystalline boron and large-size Mg can be equally useful and cost effective for industry, even without the use of nanoparticle dopants.

6.5 References

1. S. H. Zhou, A. V. Pan, J. Horvat, M. J. Qin and H. K. Liu, Supercond Sci Tech **17** (9), S528-S532 (2004).

2. S. K. Chen, K. A. Yates, M. G. Blamire and J. L. MacManus-Driscoll, Supercond Sci Tech **18** (11), 1473-1477 (2005).

3. Y. Yang, M. A. Susner, M. D. Sumption, M. Rindfleisch, M. Tomsic and E. W. Collings, Ieee T Appl Supercon **22** (2) (2012).

4. J. H. Kim, Y. U. Heo, A. Matsumoto, H. Kumakura, M. Rindfleisch, M. Tomsic and S. X. Dou, Supercond Sci Tech **23** (7) (2010).

5. J. H. Kim, S. Oh, H. Kumakura, A. Matsumoto, Y. U. Heo, K. S. Song, Y. M. Kang, M. Maeda, M. Rindfleisch, M. Tomsic, S. Choi and S. X. Dou, Adv Mater **23** (42), 4942-4946 (2011).

6. J. M. Rowell, Supercond Sci Tech **16** (6), R17-R27 (2003).

7. J. M. Rowell, S. Y. Xu, H. Zeng, A. V. Pogrebnyakov, Q. Li, X. X. Xi, J. M. Redwing, W. Tian and X. Q. Pan, Appl Phys Lett **83** (1), 102-104 (2003).

8. M. S. A. Hossain, C. Senatore, R. Flukiger, M. A. Rindfleisch, M. J. Tomsic, J. H. Kim and S. X. Dou, Supercond Sci Tech **22** (9) (2009).

9. R. Flukiger, M. S. A. Hossain and C. Senatore, Supercond Sci Tech **22** (8) (2009).

10. G. Giunchi, S. Ceresara, G. Ripamonti, A. Di Zenobio, S. Rossi, S. Chiarelli, M. Spadoni, R. Wesche and P. L. Bruzzone, Supercond Sci Tech **16** (2), 285-291 (2003).

11. J. M. Hur, K. Togano, A. Matsumoto, H. Kumakura, H. Wada and K. Kimura, Supercond Sci Tech **21** (3) (2008).

12. M. A. Susner, T. W. Daniels, M. D. Sumption, M. A. Rindfleisch, C. J. Thong and E. W. Collings, Supercond Sci Tech **25** (6) (2012).

13. D. L. Wang, Y. W. Ma, Z. G. Yu, Z. S. Gao, X. P. Zhang, K. Watanabe and E. Mossang, Supercond Sci Tech **20** (6), 574-578 (2007).

14. H. Fujii, K. Togano and H. Kumakura, Supercond Sci Tech **15** (11), 1571-1576 (2002).

CHAPTER 7: COMBINED EFFECT OF COLD AND HOT ISOSTATIC PRESSURE ON ENHANCING THE TRANSPORT CRITICAL CURRENT DENSITY OF *in-situ* MgB_2 WIRES

7.1 Introduction

The superconductivity at 39K discovered in MgB_2 among simple binary chemical composition attracted much interest in its fabrication techniques and practical applications due to low density, good compositional tolerance and easy fabrication methods[1]. The electrical application is largely determined by the current carrying capability, i.e. the critical current density (J_c) of the superconductor at the service temperature. Therefore, many researchers have been trying to improve the J_c of MgB_2 since its discovery in 2001. Although considerable progress has been made in the fabrication and performance improvement of MgB_2 during this period[2], the critical current density in MgB_2 is still smaller compared to expectations for an optimized material.

As we all know, flux pinning and electrical connectivity are the critical factors determining the performance of J_c in the Type-II superconductors. Flux pinning strength in MgB_2 is closely associated with elementary pinning force and grain size. It was reported[3, 4] that the elementary pinning force depends on condensation energy, BCS, coherence length, and impurity parameter. On the other hand, electrical connectivity is generally suppressed by voids, an insulating oxide phase, and imperfect connection between grains. Yamamoto *et al.*[5] treated this issue as a percolation system, and showed that the electrical connectivity was described as a function of the packing factor. Accordingly, a significant improvement might be achieved in J_c, if one can enhance flux pinning strength at the same time with increase the grain connectivity. However, it is actually difficult to balance the electrical connectivity and flux pinning strength of MgB_2 during preparation process. A variety of processing techniques have been investigated to improve J_c in the MgB_2 superconductors before, including irradiation[6, 7],

chemical doping[8-14] and ball milling[15-18]. Among them, carbon doping is proved to be the most effective way of improving J_c till now, especially at high fields[9, 11]. But all these techniques have focused on enhancing flux pinning by engineering grain boundaries or introducing nano-impurities and lattice defects, but have tended to neglect and even worsen the associated issues of connectivity.

In particular, the corresponding issues of connectivity play a more vital role in determining J_c performance in MgB_2 wires for the reason that the low density within the filament cores has been a serious obstacle in reaching high J_c values for *in-situ* MgB_2 wires. In addition, the reaction of magnesium and boron to form MgB_2 involves a volume contraction that produces a final density limited to about 50% of theoretical density (2.36 g/cm^3)[19]. Consequently, the typical effective cross-sectional superconductor area in MgB_2 wire is only about 10%[20]. The porosity of the wires strongly affects the electrical connectivity of the grains in the finished wires, thus resulting in decreased wire performance.

Based on these backgrounds, it is of great importance to develop an effective way of improving the mass density of MgB_2 wires with the specific aim of increasing grain connectivity. On this basis, then additional technique that can effectively enhance flux pinning strength need to be employed to further improve J_c. In this way, excellent J_c can be expected to achieve in MgB_2 wires, promoting its practical application. In present work, both cold high pressure densification (CHPD) technique and hot isostatic pressure (HIP) techniques were developed and applied to *in-situ* PIT MgB_2 wires to increase mass density, and further grain connectivity. Together with usage of carbon capsuled boron as precursor to increase flux pinning strength, significantly improved J_c were obtained in our prepared MgB_2 wires compared to all the PIT MgB_2 wires reported before.

7.2 Experimental procedure

All wires were fabricated by the *in-situ* powder-in-tube (PIT) process. The starting Mg:B atomic ratio was chosen to be 1:2. Mg powders with different particle sizes of 325 mesh, and 30–80 mesh (99.9%, 150 μm) were mixed with *in-house* carbon encapsulated amorphous boron (B, 98%) powder (the C percentage is about 2.30 wt. %). The powders mixture was inserted into a Monel with niobium (Nb) barrier, 8.5 mm in outer diameter and 5.5 mm in inner diameter. Then the composites were drawn to an outer diameter of 1.0 mm. CHPD was applied to all wires individually with the applied pressure of 1.5 GPa for core densification. To complete this, a cold high pressure densification device for fabrication of dense MgB_2 wire has been designed and equipped, and the corresponding schematic diagram is present in **Figure 7.1(a)**. One can see that high pressure on the wire is applied from four-sides via hard metal anvils at room temperature using our home built device. After CHPD treatment, it was found that cylinder wires have been deformed into cuboid wires with significant decrease of size. Consequently, a sizable enhancement of the mass density in MgB_2 wires can be obtained by this cold high pressure densification, as reported in our previous studies[21]. After CHPD treatment, HIP (about 1.4 GP in pressure) was applied to MgB_2 wires using our home built device. The pictures of this device are given in **Figure 7.1(b)**. In this device, molten salt is used as a pressing medium instead of gas. Particularly, liquid property of exerting pressure in all direction equally is the key factor for choosing incompressible liquid. In this device long wire can be easily sintered at desired temperature under specific eutectic mixture of salts (i.e. NaCl and KCl) along with Boron Nitride (BN) additives. BN is used for its significant chemical stability and plasticity. In this process, a long wire sample is kept inside the salt bed in a sealed high pressure chamber (see **Figure. 7.2 (b)**). At desired temperature solid salt mixture melts in the high pressure chamber. In this way, external force is applied into the liquid and the force is directly transmitted to the wire homogeneously. The HIP was performed in at the Institute of

High Pressure Physics (IHPP), Warsaw, Poland[14, 24]. The transport critical currents (I_c) of short pieces (6 cm) of straight wires were measured against increasing magnetic field at the International Laboratory of High Magnetic Fields and Low Temperature (ILHMFLM) in Wroclaw, Poland. The I_c was measured with a four-probe resistive method in Bitter magnet at the temperature of a liquid helium bath. The maximal available magnitude of magnetic field was 14 T and maximal current was 150A. The I_c was determined on the basis of the 1 μVcm^{-1} criterion. The morphology and microstructure were investigated by scanning electron microscopy (SEM) on a JEOL JSM-7500FA or Zeiss Ultra Plus microscope as well as transmission electron microscopy (TEM). Electron energy loss spectroscopy (EELS; JEOL ARM-200F) analysis was carried out for detecting carbon.

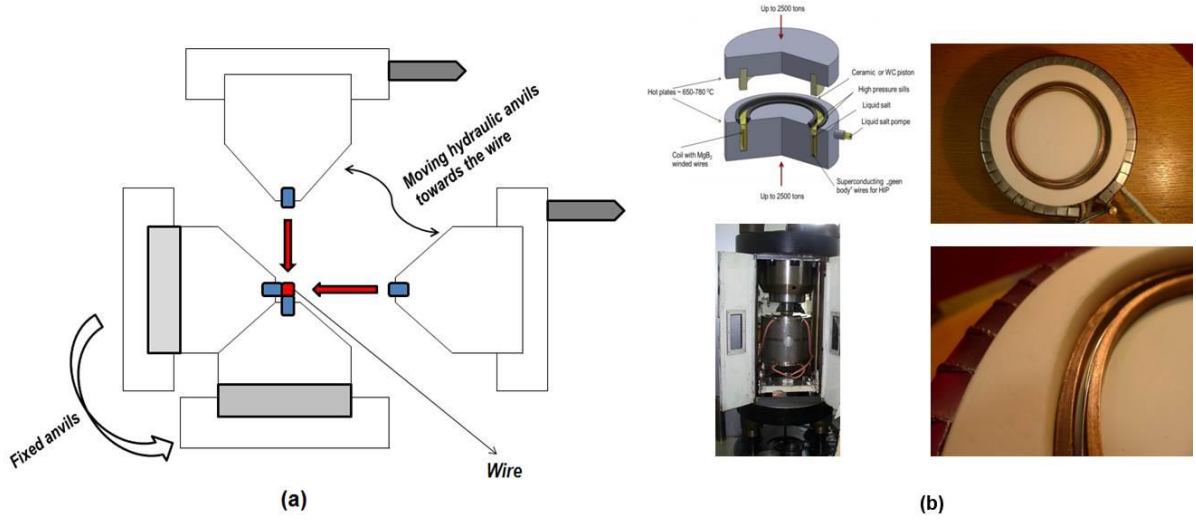

Figure 7.1 The schematic structures and pictures of our home-built CHPD and HIP devices with (a) CHPD device and (b) HIP device.

7.3 Results and Discussions

Figure 7.2 presents the schematic diagram of MgB_2 wires fabrication process and the corresponding microstructure of boron or magnesium within the wires at different stages. As shown in the TEM images of C encapsulated boron precursor in **Figure 7.2(a)**, the boron particles are very small (about 150~200 nm in size) and in amorphous state. Observing more

carefully, it can be found that these boron particles are homogenously coated by some kind of thin layer. Combined with EELS results, the coated layer is carbon-rich, which indicates that carbon indeed mainly concentrates at the surface of B particles and capsulate them uniformly during the pyrolysis process, as we expected. Compared to other techniques introducing carbon doping, such as solid state mixing and the chemical solution route, the significant advantages of using this C-encapsulated B as a precursor are that the high level of carbon doping can be achieved more homogenously in final sintered MgB_2 wires at low cost and the whole process is precisely controlled in industry. Actually, we have investigated carbon doping introduced by such C-encapsulated B precursor in our recent work[22] and found that the actual level of carbon substitution x in Mg $(B_{1-x}C_x)_2$ is as high as 0.0307.

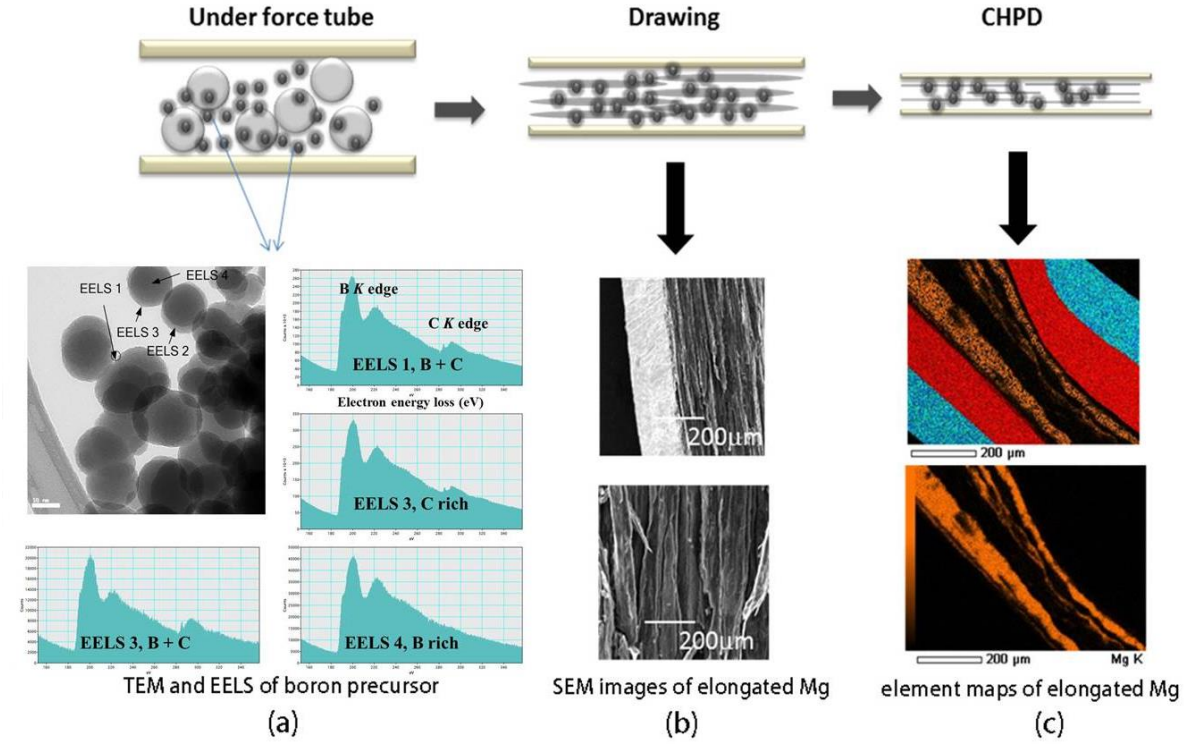

Figure 7.2 The schematic diagram of preparing process of MgB_2 wires and the corresponding microstructure of boron or magnesium within the wires at different stages.

The SEM images of elongated Mg in PIT MgB_2 wires after drawing and CHPD treatment are given in **Figure 7.2(b and c)**. Obviously, the coarse Mg original particles in PIT wires are gradually deformed into Mg fibers as the size of wires are decreased to final diameter by

drawing. It is explained that magnesium is more ductile than boron, and during cold-working the magnesium powder can be easily elongated along the wire direction, resulting in such fibrous structure within the wire core. After CHPD process, this deformation of Mg is further enhanced and the Mg fibers are elongated (see the element map of Mg within wires after CHPD in **Figure 7.2(c)**. Finally, the diameter of these Mg fibers can be reduced into approximate 40 μm. In that case, although voids can still form in the original position of elongated Mg fibers after heating treatment due to the volume reduction as a result of chemical reaction between Mg and B, their shape and direction are controlled and aligned along the wire direction, as discussed in our previous work[23]. Consequently, the electrical current could percolate easily with less hinder in such kind of microstructure and thus the electrical connectivity can be improved obviously.

Figure 7.3 shows the microstructure of superconducting core within MgB_2 wire after HIP treatment. As a reference, the microstructure of superconducting core within the MgB_2 wire prepared using traditional sintering is also shown here. It is clear that the amount and size of voids are both reduced and the sintering density is increased in the HIP MgB_2 wire compared to traditional sintered MgB_2 wire (See **Figure 7.3(a and b)**). It can be understood that isostatic pressure is employed synchronously with the reaction between Mg and B during HIP process, which can compact superconducting core and compensate the whole volume shrinkage. Besides, comparing **Figure 7.3(c)** with **Figure 7.3(d)**, clear and regular lattices are observed in the whole MgB_2 grains in traditional heated wire while some locally modulated nanostructure exist within MgB_2 grains in the HIP wire. The presence of this modulated nanostructure could be attributed to the micro strain resulting from HIP treatment. The size of this kind of nanostructure (about 10 nm) is comparable to the coherence length of MgB_2, and thus can serve as flux pinning centers.

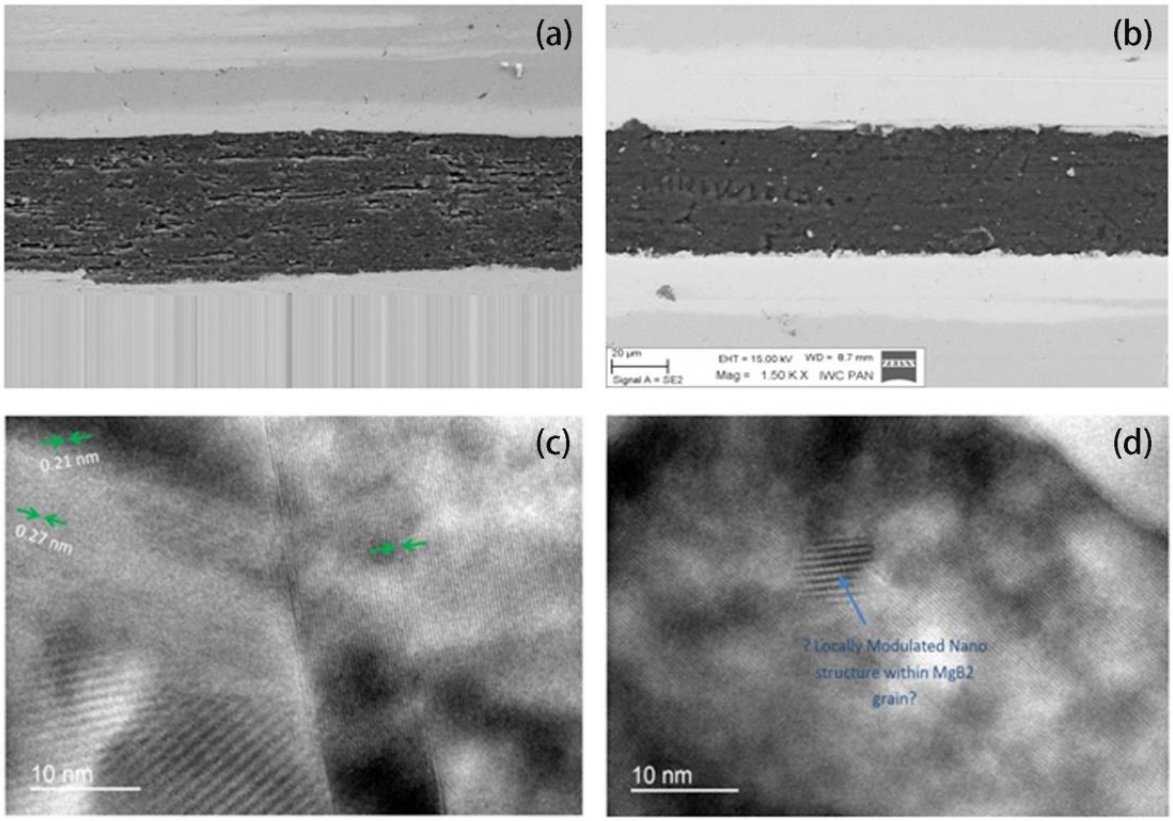

Figure 7.3 The microstructure of superconducting core within MgB_2 wire after HIP treatment. As a reference, the microstructure of superconducting core within the MgB_2 wire prepared using traditional sintering is also shown here.

Based on above results, usage of coarse Mg particle as precursor, together with CHPD and HIP treatment, are capable of dramatically increasing the mass density, decreasing the amount and size of voids as well as design their shape and alignment. All these factors are beneficial to the electrical connectivity. Moreover, carbon encapsulated amorphous boron precursor can introduce sufficient and homogenous carbon doping as well as HIP treatment can introduce some nano sized lattice distortions, which both contribute to the flux pinning strength. Therefore, the J_c should be enhanced in the prepared MgB_2 wires compared to traditional PIT MgB_2 wires. To confirm this, the transport critical current density (J_c) was measured and the corresponding magnetic field dependence of transport critical current density (J_c) at 4.2 K for the CHPD and HIP co-treated MgB_2 wires with carbon encapsulated amorphous boron precursor are illustrated in **Figure 7.4**.

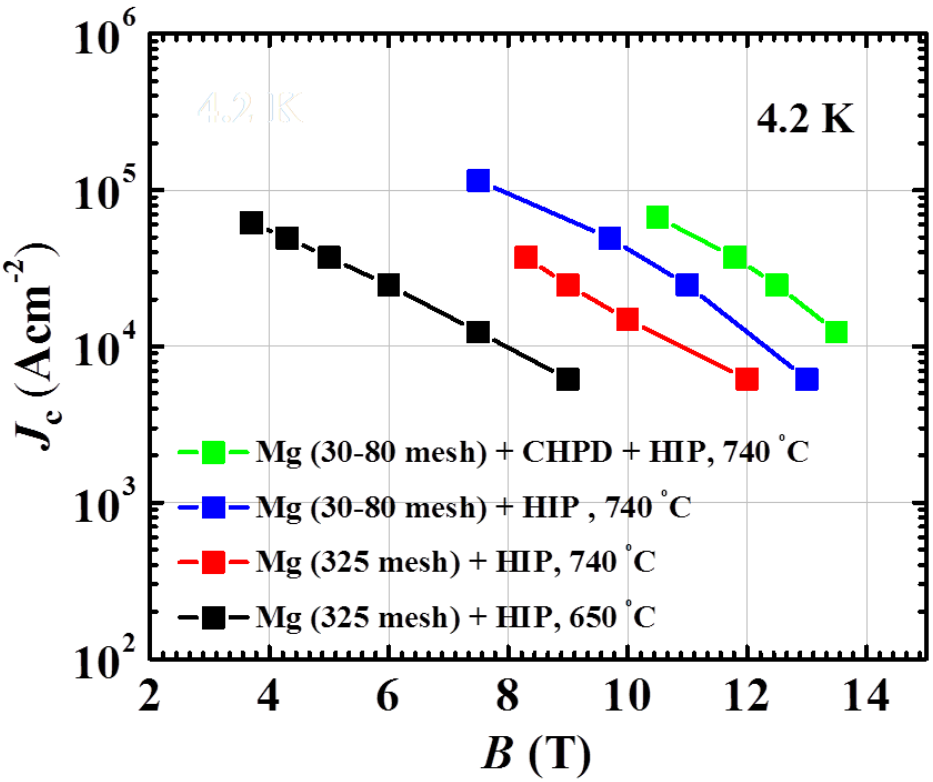

Figure 7.4 Magnetic field dependence of transport critical current density (J_c) at 4.2 K for the CHPD and HIP co-treated MgB_2 wires fabricated with small size Mg (325 mesh) and big size Mg (30-80 mesh) with carbon encapsulated amorphous B powder.

As references, the magnetic field dependence of transport critical current density (J_c) for the traditional PIT MgB_2 wire, internal Mg diffused (IMD) MgB_2 wire, only CHPD treated PIT MgB_2 wire and only HIP treated PIT MgB_2 wire is also present in **Figure 7.5**. Obviously, the values of J_c in CHPD and HIP treated MgB_2 wires are much higher than traditional PIT MgB_2 wire without any treatment, increasing approximately four times. The J_c performance of only CHPD treated wire and only HIP treated wire are also both better than traditional MgB_2 wire, whereas inferior compared to CHPD and HIP Co-treated wire. This result suggests that both of CHPD and HIP treatment indeed increase the mass density, enhance electrical connectivity and thus improve J_c. However, only CHPD or HIP treatment is not sufficient to increase mass density, collaborative effort of CHPD and HIP treatment can enhance the mass density more effectively. Generally, CHPD treatment only compact the original particles in the PIT MgB_2

wire, deform these particles and reduce the space between them, leading to the increase of original packing density and filling factor. But it has little effect on the voids forming as a result of the reaction between Mg and B during heating treatment. On the other hand, HIP treatment can just make up this limitation of CHPD treatment and reduce such voids.

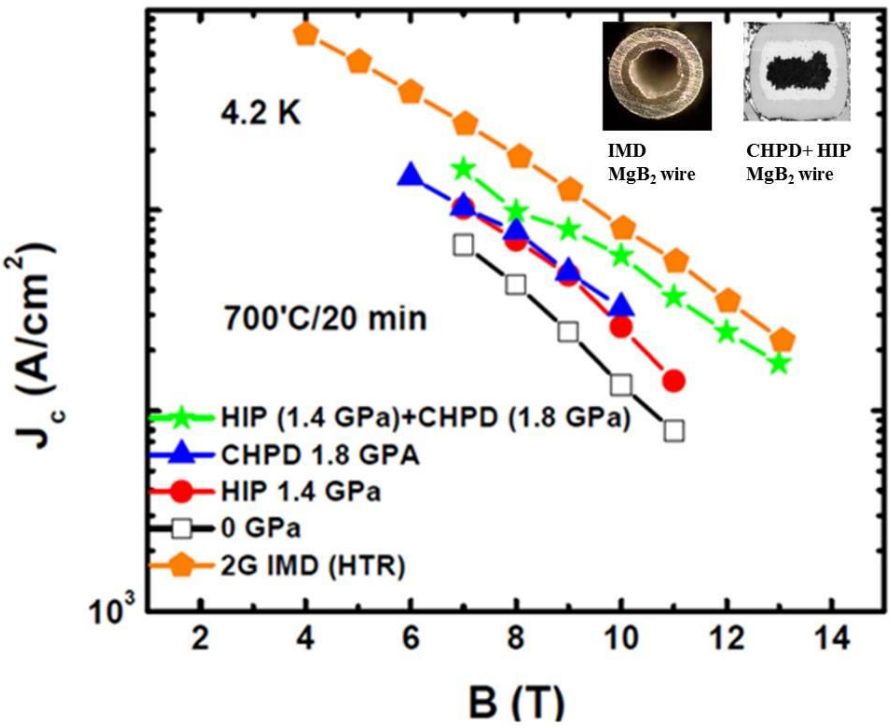

Figure 7.5 The magnetic field dependence of transport critical current density (J_c) at 4.2 K for the CHPD and HIP co-treated MgB_2 wires with carbon encapsulated amorphous boron precursor. As references, the magnetic field dependence of transport critical current density (J_c) for the traditional PIT MgB_2 wire, internal Mg diffused (IMD) MgB_2 wire, only CHPD treated PIT MgB_2 wire and only HIP treated PIT MgB_2 wire is also present here. The insets are the cross section of IMD MgB_2 wire and MgB_2 wire prepared in this work.

It is worth noting that the J_c performance of CHPD and HIP Co-treated PIT MgB_2 wires in our work is close to that of IMD MgB_2 wires reported in previous studies[24]. Although the IMD MgB_2 wires exhibit the highest J_c values among all the MgB_2 wires till now[24], there are still serious shortcoming for scaling-up this IMD 2G MgB_2 wires in view of application. During IMD process, the Mg diffuses into the B layer forming a hollow wire and only a thin layer of MgB_2 in the interior of the sheath tube (see its cross section in the inset of **Figure 7.5**). As a result, their filling factor is very low (generally approximate 18%) and thus the corresponding

engineering critical current density (J_e) performance is not as noticeable as their J_c performance. Moreover, their mechanical performance is inferior due to such hollow structure, especially when twisting into coils that are essential to fabricate various practical superconducting devices. On the contrary, the core of CHPD and HIP co-treated PIT MgB_2 wires in our work is full of superconducting MgB_2 solid and thus the filling factor is very high (see its cross section in the inset of **Figure 7.5**). One can imagine that this structure in our prepared wires possesses higher J_e as well as better mechanical properties than IMD MgB_2 wires.

7.4 Conclusion

Various technique including CHPD, HIP, usage of coarse Mg particles and carbon encapsulated amorphous boron precursors were collaboratively employed to improve J_c performance of PIT MgB_2 wires in present work. Consequently, the best J_c performance was obtained among all the PIT MgB_2 wires reported before, due to the improved grain connectivity and enhanced flux pinning strength. For one thing, usage of coarse Mg particle as precursor, together with CHPD and HIP treatment, can effectively increase the mass density, decrease the amount of voids as well as design their shape and alignment, which are responsible for the improvement of the electrical connectivity. For another thing, carbon encapsulated amorphous boron precursor is able to introduce sufficient and homogenous carbon doping, which contributes to the flux pinning strength. Moreover, the CHPD and HIP devices were both home built and conveniently operated at low cost, and large scale production of coarse Mg particles and carbon encapsulated amorphous boron can be commercially viable at comparatively low cost. This suggests that combination of these techniques could be a promising alternative for industrial production of practical MgB_2 wires with excellent J_c as the cost/performance of MgB_2 wires is superior.

7.5 References

1. J. Nagamatsu, N. Nakagawa, T. Muranaka, Y. Zenitani and J. Akimitsu, Nature **410** (6824), 63-64 (2001).

2. Z. Q. Ma and Y. C. Liu, International Materials Reviews **56** (5-6), 267-286 (2011).

3. G. Zerweck, J Low Temp Phys **42** (1-2), 1-9 (1981).

4. W. E. Yetter, D. A. Thomas and E. J. Kramer, Philos Mag B **46** (5), 523-537 (1982).

5. A. Yamamoto, J. I. Shimoyama, K. Kishio and T. Matsushita, Supercond Sci Tech **20** (7), 658-666 (2007).

6. Y. Bugoslavsky, L. F. Cohen, G. K. Perkins, M. Polichetti, T. J. Tate, R. Gwilliam and A. D. Caplin, Nature **411** (6837), 561-563 (2001).

7. M. Eisterer, M. Zehetmayer, S. Tonies, H. W. Weber, M. Kambara, N. H. Babu, D. A. Cardwell and L. R. Greenwood, Supercond Sci Tech **15** (2), L9-L12 (2002).

8. J. S. Slusky, N. Rogado, K. A. Regan, M. A. Hayward, P. Khalifah, T. He, K. Inumaru, S. M. Loureiro, M. K. Haas, H. W. Zandbergen and R. J. Cava, Nature **410** (6826), 343-345 (2001).

9. S. X. Dou, S. Soltanian, J. Horvat, X. L. Wang, S. H. Zhou, M. Ionescu, H. K. Liu, P. Munroe and M. Tomsic, Appl Phys Lett **81** (18), 3419-3421 (2002).

10. S. H. Zhou, A. V. Pan, D. Wexler and S. X. Dou, Adv Mater **19** (10), 1373-1376 (2007).

11. A. Vajpayee, V. P. S. Awana, G. L. Bhalla and H. Kishan, Nanotechnology **19** (12) (2008).

12. Z. Q. Ma, Y. C. Liu, Q. Z. Shi, Q. Zhao and Z. M. Gao, Physica C **468** (22), 2250-2253 (2008).

13. W. K. Yeoh, J. H. Kim, J. Horvat, S. X. Dou and P. Munroe, Supercond Sci Tech **19** (2), L5-L8 (2006).

14. C. Shekhar, R. Giri, R. S. Tiwari, O. N. Srivastava and S. K. Malik, J Appl Phys **101** (4), 043906 (2007).

15. A. Gumbel, J. Eckert, G. Fuchs, K. Nenkov, K. H. Muller and L. Schultz, Appl Phys Lett **80** (15), 2725-2727 (2002).

16. M. Herrmann, W. Haessler, C. Rodig, W. Gruner, B. Holzapfel and L. Schultz, Appl Phys Lett **91** (8) (2007).

17. Z. Q. Ma, Y. C. Liu, J. Huo and Z. M. Gao, J Appl Phys **106** (11), 113911 (2009).

18. X. Xu, J. H. Kim, M. S. A. Hossain, J. S. Park, Y. Zhao, S. X. Dou, W. K. Yeoh, M. Rindfleisch and M. Tomsic, J Appl Phys **103** (2), 023912 (2008).

19. E. W. Collings, M. D. Sumption, M. Bhatia, M. A. Susner and S. D. Bohnenstiehl, Supercond Sci Tech **21** (10), 103001 (2008).

20. J. M. Rowell, Supercond Sci Tech **16** (6), R17-R27 (2003).

21. M. S. A. Hossain, C. Senatore, R. Flukiger, M. A. Rindfleisch, M. J. Tomsic, J. H. Kim and S. X. Dou, Supercond Sci Tech **22** (9), 095004 (2009).

22. S. Barua, M. S. A. Hossain, Z. Ma, D. Patel, M. Mustapic, M. Somer, S. Acar, I. Kokal, A. Morawski, T. Cetner, D. Gajda and S. X. Dou, Scripta Mater **104** (0), 37-40 (2015).

23. J. H. Kim, S. Oh, H. Kumakura, A. Matsumoto, Y. U. Heo, K. S. Song, Y. M. Kang, M. Maeda, M. Rindfleisch, M. Tomsic, S. Choi and S. X. Dou, Adv Mater **23** (42), 4942-4946 (2011).

24. G. Z. Li, M. D. Sumption, M. A. Susner, Y. Yang, K. M. Reddy, M. A. Rindfleisch, M. J. Tomsic, C. J. Thong and E. W. Collings, Superconductor Science and Technology **25** (11), 115023 (2012).

CHAPTER 8: CONCLUSION

In summary, we have systematically investigated the effect of co-doing with SiC and Al_2O_3, carbon encapsulation technique, effect of CHPD with low cost crystalline boron, a synergetic effect of CHPD and HIP on the critical current density of MgB_2. The primary target of this thesis is to delineate a comprehensive method of improving critical properties of MgB_2 by intrinsic and extrinsic approach.

We have successfully synthesized pure and nano-Al_2O_3 + SiC co-doped MgB_2 polycrystalline bulks and wires. A systematic decrease in *a*-axis lattice parameter and T_c in co-doped samples with increasing SiC doping level was observed. The co-doped sample with the composition of 2 wt% Al_2O_3 + 1 wt% SiC in both bulk and wire samples show the best in-field J_c (B) performance at operating temperatures ranging from 4.2 K to 25 K due to the carbon substitution and better grain connectivity. The value of $B(10^4)$ [the field at which $J_c = 10^4$ Acm^{-2}] was enhanced from 7.6 T to 9.8 T in the co-doped wire. This result is very interesting from the view point of low-field magnet applications.

In case of bulk, fabricated with *in-house* carbon-encapsulated boron powders with different carbon contents enhanced magnetic J_c, with the highest value of 10^4 Acm^{-2} at 9.47 T, 5 K. The reason behind the improved high field J_c and pinning force is that the enhanced grain boundary pinning and homogeneous carbon distribution in the carbon-doped samples increase the Mg and B reactivity, and at the same time, restrict the grain growth of the reacted MgB_2. These results indicate that carbon-encapsulated amorphous boron could be a promising alternative for industrial production of practical MgB_2 bulks or wires with excellent J_c, as large-scale production can be commercially viable in terms of cost-effectiveness. The performance of MgB_2 bulk was enhanced intrinsically through a suitable and effective doping method. The J_c performance at high fields is mainly governed by B_{c2} and the flux pinning, and therefore, it

improves with increasing doping level up to certain level.

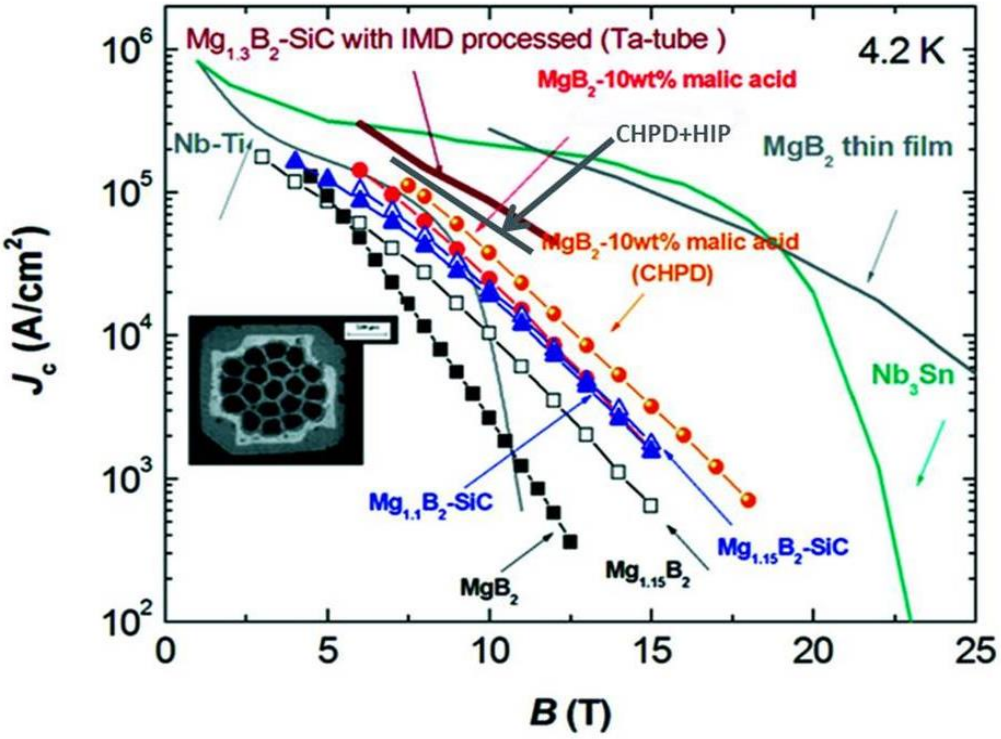

Figure 8.1 Comparison of J_c versus B characteristics at 4.2 K of LIMD wire with two steps densification (HIP + CHPD) and those of other existing MgB_2 and commercial superconductors.

Extrinsic approaches have also been studied to enhance in-field performance. From the point of economic feasibility and effectiveness in large scale applications, the most economical fabrication route and an alternate solution to the IMD method for the development of high performance, cost-effective *in-situ* PIT wires for industrial application have been investigated. The transport J_c of CHPD treated MgB_2 wires made from crystalline boron and large-size Mg shows the best performance among the other wires in this study. The possible reason for increased J_c may be the flat, directional, and elongated voids that arise after heat treatment from large size ductile Mg during the cold working process. The core is densified by the application of CHPD without any severe deterioration of the filament inside the wire. The most noticeable point in this study is that such a good quality binary conductor using cheaper crystalline boron and large-size Mg can be equally useful and cost effective for industry, even without the use

of nanoparticle dopants.

Effects of two steps densification on wire performance have been investigated in combination with carbon doping. Superior transport J_c was obtained in this method. Combined effect of CHPD and HIP facilitates void reduction and grain connectivity in MgB_2 wires made with large size Mg particle. In the first step of densification of the unreacted wire by CHPD, mass density of (Mg + 2B) was increased and in the second stage densification process during the reaction further enhancement density was resulted (see **Figure 8.1**). The fibrous structure of large Mg assists in the effective densification. In this new investigation, at 4.2 K, the J_c value was 10,000 Acm^{-2} at close to 14 T which is comparable to 2G IMD wire. The advantages of this CHPD and HIP treated LIMD wire over IMD wire is that there is no hollow structure inside the wire. A highly dense wire with enhanced mechanical durability can be fabricated by this method, which is desirable for large scale application.

In conclusion, it can be said that the in-field performance of MgB_2 conductor can be increased in a two disparate ways. High filed performance can be enhanced through effective carbon doping and low field performance can be increased by introducing pressure. In a combined method of carbon doping and high pressure technique overall field performance can be increased.

PUBLICATIONS

[1] **S. Barua**, M. S. A. Hossain, Z. Ma, D. Patel, M. Mustapic, M. Somer, *et al.*, "Superior critical current density obtained in MgB_2 bulks through low-cost carbon-encapsulated boron powder," *Scripta Materialia,* vol. 104, pp. 37-40, 2015.

[2] **S. Barua**, D. Patel, N. Alzayed, M. Shahabuddin, J. M. Parakkandy, M. S. Shah, *et al.*, "Correlation between in-field J_c enhancement and grain connectivity in co-doped MgB_2 superconductor," *Materials Letters,* vol. 139, pp. 333-335, 2015.

[3] Y. C. Liu, F. Lan, Z. Q. Ma, N. Chen, H. J. Li, **S. Barua**, *et al.*, "Significantly enhanced critical current density in nano-MgB_2 grains rapidly formed at low temperature with homogeneous carbon doping," *Superconductor Science & Technology,* vol. 28, p. 055005, 2015.

[4] M. S. A. Hossain, A. A. Gazder, **S. Barua**, A. Motaman, D. Patel, J. H. Kim, *et al.*, "Development of High Current Capacity Mono- and 18-Filament in situ MgB_2 Cables by Varying the Twist Pitch," *Ieee Transactions on Applied Superconductivity,* vol. 24, p. 6200304, 2014.

[5] M. S. A. Hossain, A. Motaman, **S. Barua**, D. Patel, M. Mustapic, J. H. Kim, *et al.*, "The roles of CHPD: superior critical current density and n-value obtained in binary in situ MgB_2 cables," *Superconductor Science & Technology,* vol. 27, p. 095016, 2014.

[6] F. Lan, Z. Q. Ma, Y. C. Liu, N. Chen, Q. Cai, H. J. Li,**S. Barua** *et al.*, "The formation of nano-layered grains and their enhanced superconducting transition temperature in Mg-doped $FeSe_{0.9}$ bulks," *Scientific Reports,* vol. 4, p. 6481, 2014.

[7] D. Patel, M. S. Al Hossain, A. Motaman, **S. Barua**, M. Shahabuddin, and J. H. Kim, "Rational design of MgB_2 conductors toward practical applications," *Cryogenics,* vol. 63, pp. 160-165, 2014.

[8] A. Motaman, **S. Barua**, D. Patel, M. Maeda, K. Cheong, J. H. Kim, *et al.*, "Power-Law

Relationship Between Critical Current Density, Microstructure, and the n-Value in MgB_2 Superconductor Wires," *Journal of Superconductivity and Novel Magnetism*, vol. 27, pp. 1643-1645, 2014.

[9] P. Dipak, H. Md Shahriar Al, S. Khay Wai, X. Xun, **B. Shaon**, M. Zongqing, *et al.*, "MgB_2 superconducting joints for persistent current operation," *Superconductor Science and Technology*, vol. 28, p. 065017, 2015.

[10] M. Mustapić, K. S. B. De Silva, S. H. Aboutalebi, **S. Barua**, X. Xu, J. Wang, *et al.*, "Improvements in the Dispersion of Nanosilver in a MgB_2 Matrix through a Graphene Oxide Net," *The Journal of Physical Chemistry C*, vol. 119, pp. 10631-10640, 2015.